Hiroshima University
Graduate School of Science

Doctoral Thesis

Investigation and manipulation of spin polarized Dirac surface state in the chalcogenide topological insulators

---

Kenta Kuroda

March 2014

Abstract

A classification of material phases is a fundamental concept in condensed matter physics to clarify particular states of matter and usually it is specified with the spontaneous breaking symmetry. For examples, the ferromagnetic materials in which the magnetic moments form ordered state can be classified into the different material phase from non-magnetic one with the broken time-reversal symmetry. Superconducting states also can feature an unique material phase regarding the broken gauge symmetry. In 1980s, the new concept to classify materials without the broken symmetry but "*topology*" of the wave function in Hilbert space was discovered and intensively developed. Eventually, the concept leaded to the great discovery of "*topological insulator*" in 2000s.

The easiest way to clarify the new material phase is a particular insulator in which an existence of a metallic state is promised at the boundary (surface). Furthermore, one of the greatest feature of the topological insulator is that the metallic surface state behaves a spin-helical and massless Dirac fermion whose motion is governed by massless Dirac equation. In contrast to Graphene, the Dirac fermion in the topological insulator is described with the real spin instead of the pseudo-spin. As a consequence, the Dirac fermion in topological insulator can directly couple to the magnetic field, which can provide us with a fertile playground to study the intriguing relativistic physical phenomena as well as the realization of the high performance spintronic devices.

This dissertation guides one to bring the novelties of topological insulators into the reality through the investigation and manipulate of the spin polarized Dirac surface state with spin-and angle-resolved photoemission spectroscopy (spin-ARPES) with synchrotron radiation and the material growths.

In Chapter 4 of this thesis we study the precise electronic and magnetic structures at the surface of the prototypical topological insulator Bi_2Se_3 with non-magnetic and magnetic impurity doping investigated by high-resolution ARPES measurement.

To further search an ideal topological insulator, the electronic structures of two candidates for the topological insulator, $TlBiSe_2$ and $PbBi_2Te_4$, are studied and it is demonstrated that the both of the candidates are topological insulator in Chapter 5 of this thesis. Especially, it is revealed that $TlBiSe_2$ possesses an ideal Dirac surface state which features in-gap Dirac point which has never been achieved in the other topological insulators. We

further discuss the spin textures of the Dirac surface state and the surface structure of $TlBiSe_2$ in Chapter 6 and Chapter 7 of this thesis. Noteworthy, the reversal spin current regime can be realized with the methodology introduced in Chapter 6. These our finding can open path way to study intriguing physical phenomena and design the future devices on the surface.

In Chapter 8 of this thesis, we come back to the surface state in the prototypical topological insulator Bi_2Se_3 and highlight the circular polarization dependence in ARPES and SARPES measurements, and develop a methodology for the spin manipulation in the spin polarized Dirac system that may facilitate further application of opt-spintronic devices.

Contents

CONTENTS

List of Figures

8

9

10

List of Tables

Chapter 1

Background

1.1 Spin-split bands under the broken symmetry

with TRS+SIS   without TRS + with SIS

(a)   (b)   Zeeman-type
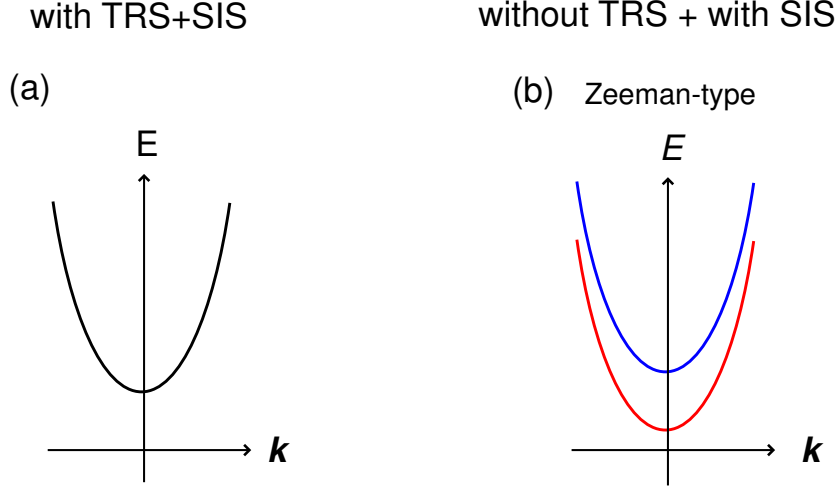
Figure 1.1: Schematics of free electron band structures (a) under a space inversion symmetry (SIS) and a time-reversal symmetry (TRS) and (b) without TRS.

Symmetry is one of the most basic and important consideration in electronic structures of a given physical system because the eigenstates and the degeneracy of eigenvalues are governed by the symmetry ingredients [1]. If the given physical system holds time-reversal symmetry (TRS), the eigenvalues should satisfy the relation:

$$E(\boldsymbol{k}, \uparrow) = E(-\boldsymbol{k}, \downarrow) \tag{1.1}$$

where $\boldsymbol{k}$ is the electron wavenumber, $\uparrow$ and $\downarrow$ denote the spin-up and -down states. Space inversion symmetry (SIS) promises the relation of eigenvalues as follows:

$$E(\boldsymbol{k}, \uparrow) = E(-\boldsymbol{k}, \uparrow) \tag{1.2}$$

With consideration of these basic symmetries, one can finally obtain a brief solution of the eigenvalues as follows:

$$E(\boldsymbol{k}, \uparrow) = E(-\boldsymbol{k}, \downarrow) \tag{1.3}$$

and thus the states are spin degenerate in a whole E-k space (see Fig. 1.1 (a)) owing to both of these symmetries, which is well known as the Kramers degeneracy and is hardly protected by the symmetry restriction. However, when the both or either of the symmetries the degeneracy of the energy band is broken up, the spin dependent energy states are allowed to come into existence. Here discuss how the state degeneracy can be lifted by the symmetry breaking. Generally, under an external magnetic field, electrons take a spin dependent potential. Briefly, this potential can be described by Zeeman type potential:

$$U \propto \boldsymbol{s} \cdot \boldsymbol{H} \tag{1.4}$$

where the $\boldsymbol{s}$ is spin of electrons and $\boldsymbol{H}$ is an external magnetic field. As a consequence of the spin dependent potential, the spin-degeneracy of the free electron parabola in Fig. 1.1(a) is lifted along energy axis as shown in Fig. 1.1(b). As is clearly understood with the Eq. (1.4), the size of the spin splitting is determined by the strength and direction of the magnetic field.

The k-dependent spin splitting is allowed in the case of the broken space inversion symmetry (SIS) and importantly the size of the splitting is governed by the spin-orbit coupling (SOC) expressed as :

$$H_{SOC} = \propto (\boldsymbol{\nabla} V \times \boldsymbol{k}) \cdot \boldsymbol{s} \tag{1.5}$$

where V is the crystal potential, k is the momentum, respectively. Assuming the lack of inversion symmetry along z axis, the potential in the system can generate a net electric field $\boldsymbol{E}$ in the z direction. Finally Eq. (1.5) can be converted into:

$$H_{SOC} = \propto (\boldsymbol{E} \times \boldsymbol{k}) \cdot \boldsymbol{s} \tag{1.6}$$

If the term $(\boldsymbol{E} \times \boldsymbol{k})$ is considered as an effective magnetic field $(\boldsymbol{B}_{eff})$, the SOC term is represented as:

$$H_{SOC} \propto \boldsymbol{B}_{eff} \cdot \boldsymbol{s} \tag{1.7}$$

The expression in Eq. (1.7) absolutely tells us that the SOC in a lack of SIS can be a cause of the effective magnetic field acting on the electron spin. The effective magnetic field via the SOC strongly depends on the electron momentum, which finally results in the k-dependent spin splitting in contrast to the case without the TRS. Figures 1.2(a) and (b) represent two typical cases for the spin-split bands and their constant energy contours (CECs) under the

with TRS + without SIS

(a)   Rashba-type

(b)   Dirac cone
        (Topological insulator)
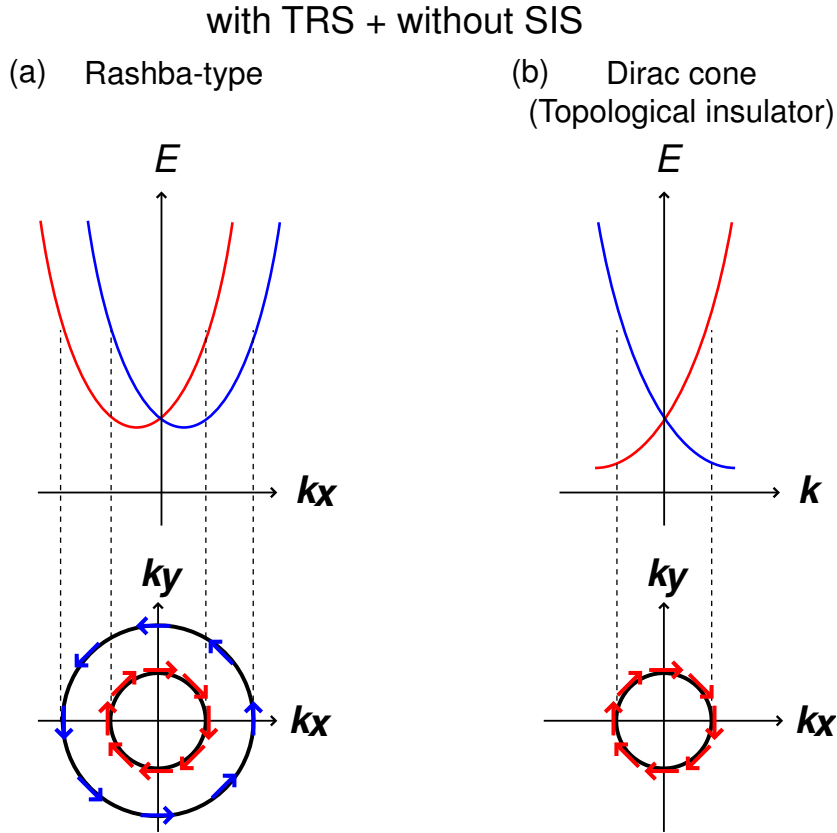
Figure 1.2: Schematic images of spin-split band structures in a lack of space inversion symmetry (SIS) for (a) Rashba-type and (b) Dirac cone like energy dispersion which can be realized in topological insulator.

broken SIS. In both cases, the energy bands are degenerate at the TRS momenta in k-space and furthermore the spin splitting is antisymmetric along k axis with respect to the TRS momenta. The both features are hallmarks of the TRS as is described in Eq. (1.1).

Note that the SIS is always broken at solid surfaces in perpendicular direction to the surface and thus the spin-splitting is general effect. However, in order to induce a experimentally observable spin-splitting, the large SOC is required as this type of spin splitting surface bands can be generally observed at the surface of heavy elements such as Au, Bi and so on [2, 3]. Note that the electronic state should have only $\boldsymbol{k}_{\parallel} = (k_x, k_x)$ dependence since the surface

states are well localized near the surface the surface. As a consequence of the two-dimensionality, the electron spins are strongly locked in-plane and the perpendicular to $k_\parallel$ through the strong SOC as described in Eq. 1.6 and finally form the spin-helical texture along the constant energy contour as shown in Fig. 1.2.

The k dependent spin splitting induced by the strong SOC is currently expected to be a promising effect for realizing the spintronic devices as well as studying relativistic physics. The spin bands in Fig. 1.2(a) shows two parabolic energy dispersions accompanying two CECs. In contrast, X-shaped dispersion, so called "*Dirac cone*" is formed, which results in a single CEC. In the former case, this type of spin splitting are well known as a Rashba spin splitting [4]. It should be noted that the difference in both surface states is not a product of chance but a result of "*topology*". The spin-helical "*Dirac cone*" type of the surface state is recently discovered on the surface of the particular materials, the so-called "*topological insulator*". The "*topological insulator*" can be classified into a topologically non-trivial state of matter from the Rashba system with a band "*topology*" in the bulk. The different "*topology*" of the bulk electronic states create the different surface states through a bulk-edge correspondence. The concept of "*topological insulator*" and the band "*topology*" will be further introduced in Sec. 1.2.

1.2 Introductions to Topological insulator

The theoretical prediction and experimental discovery of a new class of materials known as "*topological insulator*" (TI) is a major recent subject in the condensed matter physics. This material can be distinguished from a conventional band insulator with a non-trivial topology and a spin-helical surface state that behaves massless Dirac fermion owing to a strong spin-orbit coupling. Therefore TI is a promising quantum state for future technologies such as spintronic devices and studying the peculiar relativistic phenomena. Historically, the concept of band "*topology*" in TI is strongly connected to the quantum Hall (QH) state. In fact, "*topological insulator*" is called quantum spin Hall (QSH) state soon after the discovery and QSH state can be considered well as a superposition of two QH states with opposite magnetization directions. The introduction section will start with an explanation of topology in relation with QH effect (Sec. 1.2.1). An statements on the parity anomaly (Haldane model) will follow in Sec. 1.2.2, which connects the QH state to the QSH state. In Sec. 1.2.3, the QH effect will be expanded to the two-dimensional version of TI and Z_2 topological invariant will be introduced in Sec. 1.2.4. Finally, the three-dimensional TI will be introduced in Sec. 1.2.5.

1.2.1 Quantum Hall state
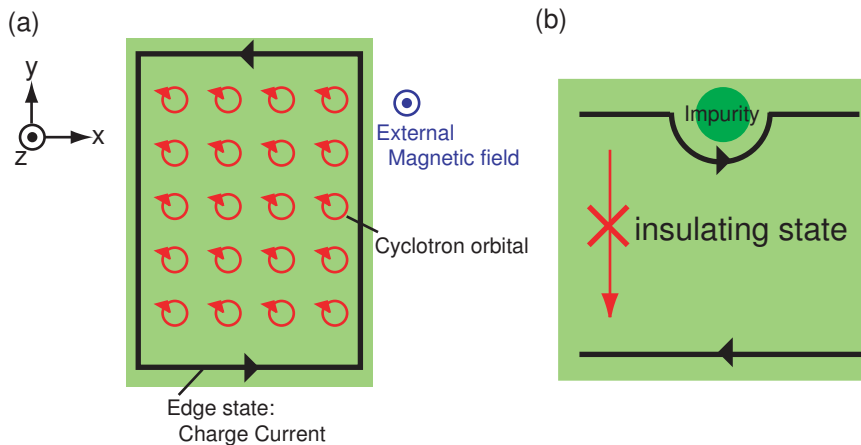
Figure 1.3: (a) Quantum Hall state (b) Robust chiral edge channel.

QH effect is a quantum version of Hall effect in which Hall conductance is quantized and given by:

$$\sigma_{xy} = \frac{e^2}{h}\nu \qquad (1.8)$$

where e is the elementary charge, h is Plank's constant and ν is known as the integer (or fractional) filling factor of Landau level. The effect has been originally predicted by *Ando* in 1975 [5] and experimentally demonstrated that Hall conductance (transverse conductance σ_{xy}) is exactly quantized in two-dimensional electron gas at heterojunction with a strong magnetic field in perpendicular to the sample by *von Klitzing* in 1980 [6]. *von Klitzing* won Nobel prize for the experimental work in 1985. Figure 1.4 represents a schematic image of QH effect. Under the magnetic field $\boldsymbol{B}$ in perpendicular to the surface, the electrons feel Lorentz force which gives σ_{xy} in breaking the time-reversal symmetry (TRS). With symmetric gauge, the vector potential $\boldsymbol{A}$ can be written as $\boldsymbol{A} = \frac{B}{2}(y, -x, 0)$ which then produces the following Hamiltonian;

$$H_{\text{Lorentz}} \propto (xp_y - yp_x)|B| \qquad (1.9)$$

where $\boldsymbol{p}$ is momentum in two-dimensional (x-y) plane. If magnetic strength is strong enough, the electrons will be forced to take localized cyclotron orbits as shown by red-colored circles in Fig.1.4(a), which results in a bulk insulation. However, the electrons cannot complete their cyclotron motions at the edge, which creates metallic electronic states at the edge as depicted with black bold line in Fig.1.4(a). These peculiar charge currents are known as the chiral edge mode in the QH state. Specifically, the chiral edge state is very robust against impurities or defects. When the electron encounters them as schematically shown in Fig. 1.4(b), one can expect that there are two possible ways for electron motion: (1) Scattered to the other side of edge channel. (2) Going through the obstacle and keeping forward-moving. Now, because the bulk is insulating, case(1) can not happen if the both edge states are isolated well in real space. Therefore, the electron should keep going forward, which allows the perfect transmission.

Interestingly, the QH state has been considered with an idea of topology, which was firstly proposed by *Laughlin* with a gauge invariant using an annulus geometry in 1981 [7]. Soon after his thought experiment, *Thouless, Kohmoto, Nightingale,* and *den Nijs* (TKNN) developed the expression for the Hall conductance (σ_{xy}) in a periodic system based on Kubo formula, which is well known as TKNN formula, and finally discovered a topological

invariant in the QH state, so called Chern number (C) [8]. The C can be understood by Berry phase (Φ) that is a production of geometry in Hilbert space with $|\boldsymbol{k}>$ [9]. According to TKNN formula, if the Fermi level is located between lth energy gap, σ_{xy} is written by with C:

$$\sigma_{xy} = \frac{e^2}{\hbar} \sum_{\alpha=1}^{l} C_\alpha \tag{1.10}$$

where α is a index of the Landau level. C_α forms:

$$C_\alpha = \int_{BZ} \frac{d^2\boldsymbol{k}_\alpha}{(2\pi)^2} \frac{\partial}{\partial \boldsymbol{k}_\alpha} \times \boldsymbol{A}_\alpha(\boldsymbol{k}_\alpha) \tag{1.11}$$

where

$$\boldsymbol{A}_\alpha(\boldsymbol{k}_\alpha) = i < \boldsymbol{k}_\alpha | \frac{\partial}{\partial \boldsymbol{k}_\alpha} | \boldsymbol{k}_\alpha > \tag{1.12}$$

In Eq. 1.12, $\boldsymbol{A}_\alpha$ is a Berry connection or Berry vector potential. With similar treatment of vector potential in electromagnetism, the term of $\frac{\partial}{\partial \boldsymbol{k}_\alpha} \times \boldsymbol{A}_\alpha(\boldsymbol{k}_\alpha)$ can be rewritten with magnetic flux density (B_α) and therefore the C_α can be transformed into:

$$C_\alpha = \int_{BZ} \frac{d^2\boldsymbol{k}_\alpha}{(2\pi)^2} \boldsymbol{B}_\alpha = \Phi_\alpha \tag{1.13}$$

The term of $\boldsymbol{B}$ and Φ are called Berry curvature and Berry phase. With Eq. (1.13), one can find C as a magnetic flux in the parameter (k) space. In the case of integer quantum Hall state, the Landau states actually have identical $C=2\pi$ and therefore the ν in Eq. (1.8) is equal to the filling number of Landau levels. The consequence of Eqs. (1.10)-(1.13) is very surprising because the phase of the wavefunctions induced by the geometry in Hilbert space determines the macroscopic current in the QH state. Thus, the QH state can be distinguished from a conventional band insulator with the topological invariant. Starting with the QH state, the topology in condensed matter physics has been intensively developed.

1.2.2 Haldane model

After the discovery of the QH state, it was believed that the Landau level is required for the realization of topologically non-trivial QH sate. However, in 1988, *Haldane* theoretically proposed an integer quantum Hall effect without
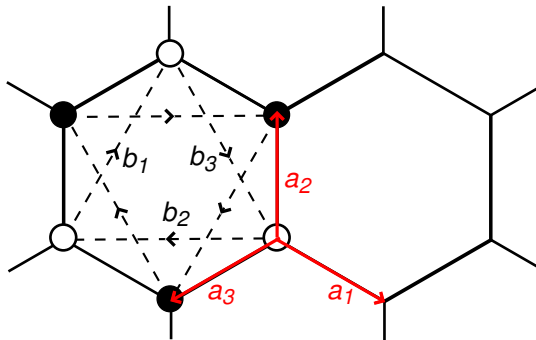
Figure 1.4: Honeycomb lattice in Haldane model. Open and closed circles represent the A and B sublattice sites, respectively. Dashed and Red color arrows represent next-nearest-neighbor and nearest-neighbor vectors denoted with denoted by b_i and a_i (i=1, 2, 3), respectively.

Landau levels and demolished the conventional wisdom [10]. Haldane used a honeycomb lattice, where there are sublattice sites A and B in Fig. 1.4, and assumed that a hopping matrix element between nearest neighbor sites is real t_1 and one between the next nearest neighbor sites is a complex number $t_2 e^{i\phi}$ or $t_2 e^{-i\phi}$. The total hopping matrix element along the triangle path ABA or BAB becomes $t_1^2 t_2 e^{i\phi}$ and coincides with a flux penetrating the triangular plane. On the other hand, for the hopping along the perimeter of honeycomb lattice, the matrix element is t_i^6 and thus the flux in honeycomb lattice is zero. With this assumption, one can make an electronic system without Landau level even if external magnetic field is applied because the magnetic flux locally remains but is canceled out in the unit cell. *Haldane* developed the Hamiltonian around K and K' point within the first order:

$$H_{K,K'}(\boldsymbol{k}) = \hbar c(\pm k_x \sigma_x + k_y \sigma_y) + M_\pm \sigma_z$$
$$c = \frac{\sqrt{3}t_1}{2\hbar} \tag{1.14}$$
$$M_\pm = M \pm 3\sqrt{3}t_2 sin\phi$$

where $\sigma_{x,y,z}$ is the Pauli matrix. Eq. (1.14) represents that low energy excitation state in Haldane model can be described as massive (gapped) Dirac fermion with $M_\pm$. Haldane started with the Dirac equation and finally discovered that the Hall conductance is quantized in this model, which can be

described as:

$$\sigma_{xy}(\boldsymbol{k}) = \frac{e^2}{\hbar}[sgn(M_-) - sgn(M_+)] \tag{1.15}$$

This result is very surprising because the quantized Hall conductivity is governed by the mass (gap) term of Dirac fermion owing to the non-zero Chern number without Landau level. The fact is known as parity anomaly in (2+1) dimensional Dirac fermion. Importantly, it should be noted that the gap needs to close at once to change Chern number, which is an evidence of the existence of the topological invariant in the system. These band insulators which possesses non-zero Chern number without Landau levels are called Chern insulator.

1.2.3 Quantum Spin Hall state

In 2005, *Kane-Mele* extended the Haldane model to apply for the system with TRS by introducing a spin-orbit coupling (SOC) as a perturbation to discuss the topologically non-trivial aspect and to see its edge state of graphene. [11]. Importantly, it should be noted that the edge state is however not a chiral but a spin-helical edge mode as a consequence of TRS as shown in Fig. 1.5(a) which is in sharp contrast to QH state and *Haldane* model. Therefore, this topologically non-trivial state is called quantum spin Hall (QSH) state.

The SOC term can be described with $(\boldsymbol{p} \times \boldsymbol{E}) \cdot \boldsymbol{\sigma}$, where $\boldsymbol{\sigma}$ is the Pauli spin matrix and $\boldsymbol{E}$ is the electric field. Since $\boldsymbol{p}=(p_x, p_y)$ and $\boldsymbol{E}=(E_x, E_y)$ are all defined in a two dimensional (x-y) plane, this Hamiltonian consists of only z component as given by:

$$H_{\text{SOC}} \propto (E_x p_y - E_y p_x)\sigma_z = B_{eff}\sigma_z \tag{1.16}$$

This equation indicates that each electron with opposite spin directions feels effective magnetic field in perpendicular to the surface. Therefore, the spin-up electrons would behave a chiral edge state with a conductance quantized in fractional multiples of $\frac{e^2}{h}$ in Fig. 1.5(b), while the spin-down electrons would be anti-chiral with a conductance in fractional multiples of $-\frac{e^2}{h}$ in Fig. 1.5(c). These two channels are superimposed together that leads to TRS, that is, the spin-up electron is moving in the left direction while the spin-down electron is moving in the reversed direction (Fig. 1.5(a)). Although there are both left-moving and right-moving channels in the each edge in
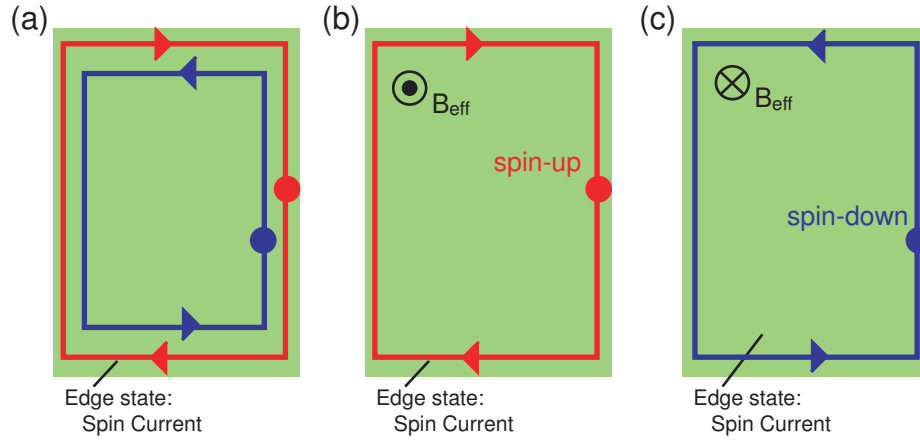
Figure 1.5: Schematics of (a) quantum spin Hall state and its (b) spin-up and (c) spin-down edge channels.
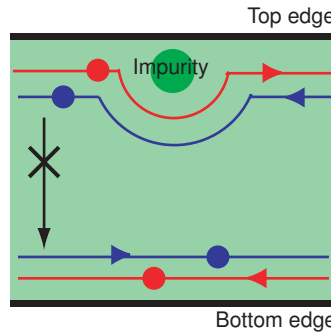
Figure 1.6: Perfect transmission in spin-helical edge state.

contrast to a single channels in QH edge sate, the back-scattering is still forbidden by the TRS. When an edge electron of the QSH state can be reflected by non-magnetic impurities as described in Fig. 1.6, one can expect that there are three possible cases for the electron motion. (1) Scattering into the other edge. (2) Back-scattering to the anti-chiral edge. (3) Keeping its way without scattering. The case (1) can not happen because the bulk is insulating. The case (2) can not happen because the spin-flip scattering is prohibited at the non-magnetic impurity. Therefore, the electron has to keep going forward, which allows a perfect transmission.

However, this process works only when there is an odd number pair of forward and backward channels as characterized by Z_2 topological invari-

ant [12]. This is a hallmark of the QSH with Z_2 topological invariant as will
be further introduced in Sec. 1.2.4. We should also note that time-reversal
symmetry is broken if the impurity is magnetic and then perfect transmission
is no longer possible and robustness would not be guaranteed. Here, we com-
pare the QH state with the QSH state in Table 1.1. The helical edge state
for the QSH system can not carry the charge current but the spin current
while the chiral edge state in the QH state produces charge current.
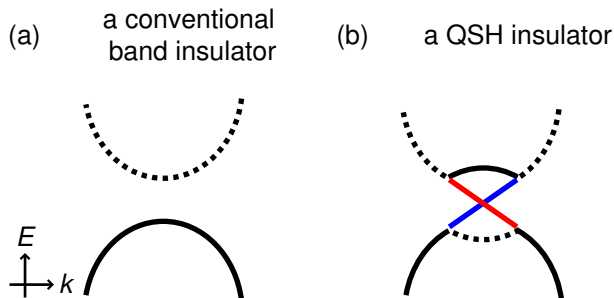
Figure 1.7: Schematic diagram of the band structures in (a) conventional band
insulator before the band inversion and (b) quantum Hall state with spin-helical
edge state after the band inversion.

Kane-Mele found that the effective Hamiltonian in the model can be
expressed as:

$$H_{KM} = \hbar c(k_x \sigma_x \tau_z + k_y \sigma_y) + \Delta_{SO} \sigma_z \tau_z s_z \tag{1.17}$$

where $\tau_z=+1, -1$ is a index for K and K' points, s_z indicates a z spin compo-
nent and Δ_{SO} is a strength of SOC. Importantly, the effective Hamiltonian in
the *Kane-Mele* model also leads to the parity anomaly in (2+1) dimensional
Dirac fermion introduced in *Haldane* model in Sec 1.2.2. This result implies
that the topological invariant can be defined with the sign of the mass term
also in this model. However, the mass term in the *Kane-Mele* model is gov-

	magnetic field	T	edge state
QH state	necessary	LT	Chiral charge state
QSH state	unnecessary	possible at RT	Spin-helical state

Table 1.1: Comparing quantum Hall (QH) state and quantum spin Hall (QSH)
states. (RT (LT) is room (low) temperature)

erned by a sign of SOC, and therefore the topological invariant is determined by the SOC. In analogy to *Haldane* model, the sign of mass (Δ_{SO}) has to be reversed to turn into the different topological phase. This indicates that the energy level at typical k point needs to be reversed between a conventional insulator and a QSH insulator as shown in Fig. 1.7. The consideration based on the parity anomaly of massive Dirac fermions in the *Kane-Mele* model crucially gives us an important consequence that the band inversion plays a role in the realization of topological non-trivial QSH state. *Kane* and *Mele* proposed the QSH sate in Graphene with the band inversion owing to the SOC but the realistic strength of SOC in Graphene is too small to generate the QSH state. Therefore, it was required to find proper materials with the strong SOC as well as the band inversion.

In 2006, *S.-C. Zhang* theoretically predicted that the QSH insulator can be realized in two-dimensional electron system of the quantum well structure of HgTe/CdTe heterostructure owing to the strong SOC [13] and, soon after that, *Molenkamp* with *S.-C. Zhang* experimentally discovered the quantized edge current in the system [14]. It is expected that this discovery would solve some problems in spintronics such as (i) low spin current density and (ii) insufficient spin life-time because the QSH state generate a dissipationless spin current naturally. Moreover, it is surprising that the spin-current can be realized at room-temperature without external magnetic field, thus these special properties could be useful not only for fundamental physics but also for creating new functional devices.

1.2.4 Z_2 topological invariant

As described so far, both QH and QSH states are topologically non-trivial, where the edge shows robust metallic feature although bulk is insulating. The band structures of the two bulk insulating states are compared with that of the conventional band insulator (CBI) in Fig. 1.8. The QH and the QSH states can be distinguished from the CBI because the topological non-trivial state possess the surface state that connects the bulk valence band to the bulk conduction band as shown in Fig. 1.8(b) and (c) while the surface state of the CBI show two parabolas inside the bulk energy gap (see Fig. 1.8(a)). Interestingly, the differences in the energy dispersion of the surface state contains some "topological invariants", which is useful to classify the condensed matter states into several classes. As mentioned in Sec. 1.2.1, "Chern number" is a topological invariant in QH state under the
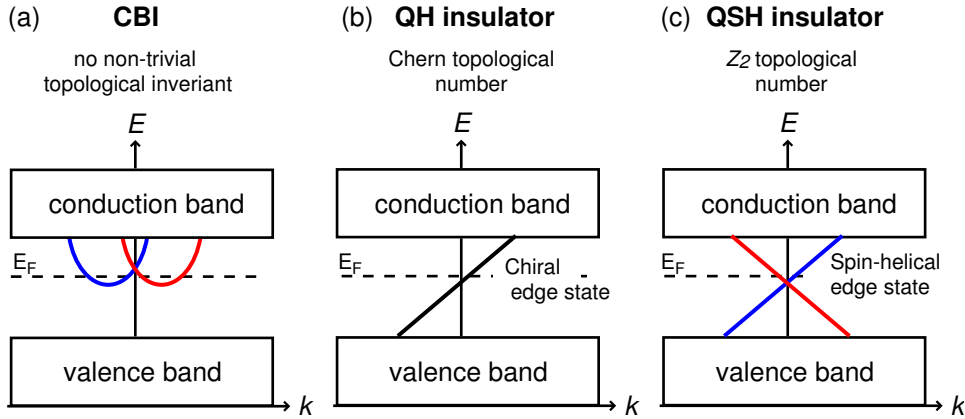
Figure 1.8: Comparison of the band structure with the typical surface state within the bulk energy gap in (a) conventional band insulator (CBI) and (b) quantum Hall (QH) insulator with chiral edge state and (c) quantum spin Hall (QSH) insulator with spin-helical edge state.

breaking of TRS and gives a index of the Hall conductance, which is driven by the curvature of wave function in Hilbert space. In QSH state, new class of characteristic "Z_2 topological number" was mathematically discovered by *Kane* and *Mele* [12], which enables us to classify the QSH state from the other insulators under the presence of TRS. Below, we further introduce the Z_2 topological number and finally connect the topological invariant to the energy dispersion of the edge states.
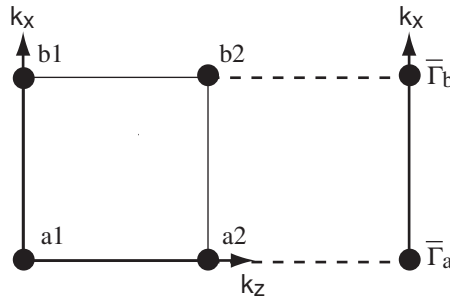
Figure 1.9: Two-dimensional Brillouin zone and its projection to one-dimensional edge.

In contrast to the Chern invariant, the Z_2 topological invariant is a mod 2 number, which can be classified into only two classes, even (0, 2, 4, ...)

and odd (1, 3, 5, ...) or just 0 (even) and 1 (odd). For $Z_2 = 0$ (even), the state can be classified into the same class as that for the CBI, that is, topologically"trivial". On the other hand, for $Z_2 = 1$ (odd), the state is topologically "non-trivial" state and can be classified into the QSH class. To understand the Z_2 number, at first, we consider the square two-dimensional Brillouin zone, and projected onto the edge, that is, one-dimensional system as shown in Fig. 1.9. Here, it is enough to consider only a quarter of two-dimensional Brillouin zone because of the TRS. There are four time-reversal invariant momenta (TRIMs) as denoted with $a1$, $a2$, $b1$, $b2$ in Fig. 1.9. In a freestanding two-dimensional system with space-inversion symmetry, Z_2 number ν_0 is given by:

$$(-1)^{\nu_0} = \prod_{i=1}^{4} \delta_{ij} \quad (i = a \text{ or } b, \, j = 1 \text{ or } 2) \tag{1.18}$$

$$\delta_{ij} = \prod_{m=1}^{N} \xi_{2m}(\boldsymbol{k}_{ij}) \quad (i = a \text{ or } b, \, j = 1 \text{ or } 2) \tag{1.19}$$

where $\xi_{2m}(\boldsymbol{k}_i) = \pm 1$ exhibits the parity ($+1$ or -1) eigenvalue of the Kramers
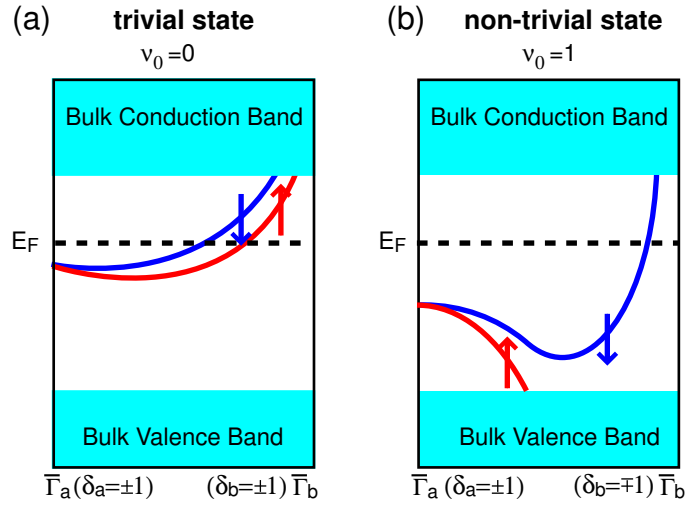
Figure 1.10: Schematic image of the relation between the topological number and the surface energy dispersions in (a) trivial state and (b) topologically non-trivial states.

pairs at TRIMs and N is the number of Kramers pairs below Fermi energy.

27

Now, we return to the edge state, and try to interpret the Z_2 topological number ν_0. Fig.1.10 shows two possible edge states along a path connecting the TRIMs $\overline{\Gamma}_a$ and $\overline{\Gamma}_b$. Here, we define the quantities δ_a and the momenta δ_b at $\overline{\Gamma}_a$ and $\overline{\Gamma}_b$, respectively as shown in Fig1.9. δ_i is described by:

$$\delta_i = \delta_{i1}\delta_{i2} \quad (i = a \text{ or } b) \tag{1.20}$$

It should be noted that δ_i can also be determined by the parity production in two-dimensional Brillouin zone. Figure 1.10(a) and (b) represent the schematic image of the surface and bulk band structures for the topological trivial and non-trivial states, respectively. Specifically, this "even-odd" Z_2 number contains the number of times for the edge state crossing at the Fermi energy. If δ_a=1 and δ_b=1 or δ_a=−1 and δ_b=−1, with Eq. (1.18), the edge state crosses the Fermi level even times and thus can be defined as topologically trivial sate as shown in Fig. 1.10(a). On the other hand, for $\delta_a = 1$ and $\delta_b = -1$, Z_2 number will be $\nu_0 = 1$ and thus we can define topologically non-trivial phase in which the edge state crosses the Fermi energy odd times as shown in Fig. 1.10(b). Here, it is noteworthy that the relation of the even-odd time crossing E_F is immutable wherever E_F is located within the bulk energy gap as long as the bulk energy gap opens, which indicates that there is a topological invariant, that is, Z_2 topological number, to classify the two insulators.

1.2.5 Three dimensional Topological insulator
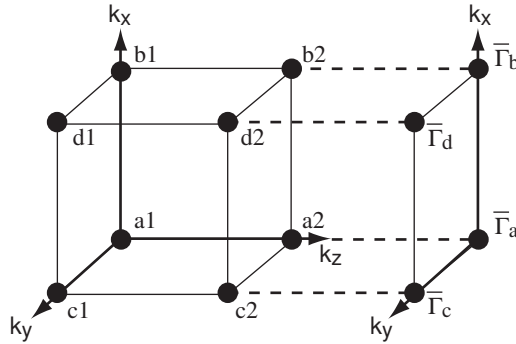
Figure 1.11: 1/8 three-dimensional Brillouin zone and its projection to two-dimensional plane

In 2007, some theorists found that it is possible to expand the two-dimensional QSH state into the three-dimensional case [15, 16, 17]. In the three-dimensional case, the edge state is no longer the one-dimensional state but the two-dimensional surface state. Soon after its discovery, the three-dimensional Z_2 topological insulator has started to be called as "topological insulator" (TI). In order to analyze the Z_2 topological invariant in three-dimensional system, $\frac{1}{8}$ three-dimensional Brillouin zone and its projection two-dimensional plane should be considered as shown in Fig 1.11. In the figure, the dots indicate the TRIMs. In contrast to the two-dimensional system with four TRIMs, eight TRIMs should be considered in three-dimensional system. Therefore, Eq.1.18 can be replaced with the following equation,

$$(-1)^{\nu_0} = \prod_{i=1}^{8} \delta_{ij} \quad \text{(i=a, b, c, d j=1 or 2)} \tag{1.21}$$

where δ_i is given by

$$\delta_{ij} = \prod_{m=1}^{N} \xi_{2m}(\boldsymbol{k}_{ij}) \quad \text{(i=a, b, c, d, j=1 or 2)} \tag{1.22}$$

In the Eq. (1.22), we assumed that the system has the space inversion symmetry (SIS) to simplify the analysis. In fact, the analysis of Z_2 topological invariant in the system without the SIS is complicated [16] and therefore is limited to the case with space inversion symmetry (SIS). In the presence of the SIS symmetry, the parity can be defined at TRIMs and δ_{ij} is a product of the parities for the all occupied eigenfunctions at the TRIM. In analogy to the two-dimensional QSH state, let us see whether it is topologically "non-trivial" state or not. Here, we assume four δ_i's at the four TRIMs in the two-dimensional Brillouin zone which are projected from the three-dimensional system.

$$(\delta_a, \delta_b, \delta_c, \delta_d) = (-, +, +, +) \tag{1.23}$$

Now, we should find Z_2 topological number $\nu_0 = 1$ in this case, which is topologically "non-trivial". Here, we consider the model "non-trivial" surface state with assumed δ_i in Eq. (1.23). Fig. 1.12 (a) shows a quarter of the surface Brillouin zone, which can cover all the Brillouin zone due to TRS. There are five high symmetry lines, for example, $\overline{\Gamma}_a$ - $\overline{\Gamma}_b$, $\overline{\Gamma}_a$ - $\overline{\Gamma}_c$ *etc*. For all of the high symmetry lines, two classes $\delta_i = -1$ or 1 are listed in Table. 1.2.
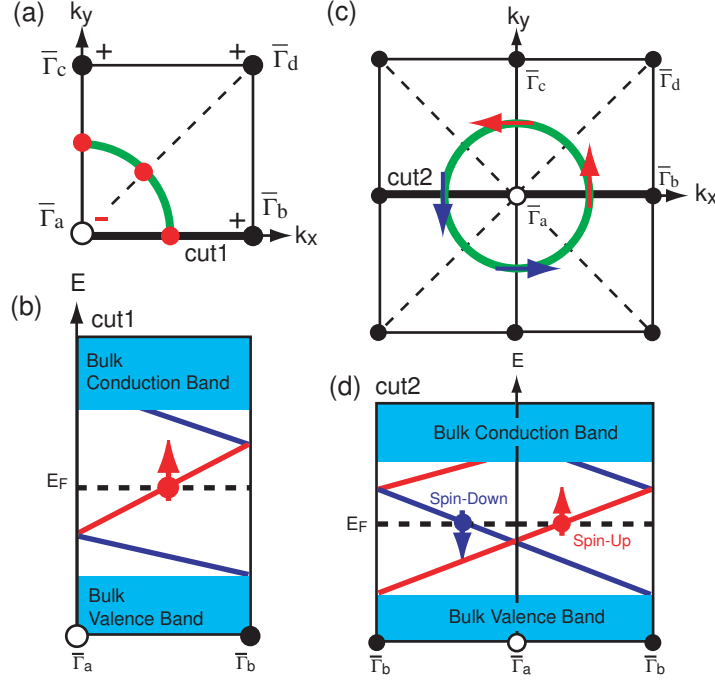
Figure 1.12: (a) Fermi square of 1/4 surface Brillouin zone. (b) The energy band structure along the cut 1(Bold line) in (a). (c) Fermi surface in the whole surface Brillouin zone (d) The energy band structure along the cut 2 (Bold line) in (c).

For example, along $\overline{\Gamma}_a$-$\overline{\Gamma}_b$ line, the edge state can form the "non-trivial" band structure as shown in Fig. 1.12(b) because there is $\delta_i = -1$ along this line. Red (Blue) color lines indicate spin-up (down) states and both of them should be degenerate at the TRIM in the presence of the TRS. Here, we consider the simplest case where the number of crossing point is one. The same thing is allowed for the other two high summery lines, $\overline{\Gamma}_a$-$\overline{\Gamma}_c$ and $\overline{\Gamma}_a$-$\overline{\Gamma}_d$ lines. On the other hand, for $\overline{\Gamma}_b$-$\overline{\Gamma}_d$ and $\overline{\Gamma}_c$-$\overline{\Gamma}_d$ lines, the edge state shows even-time crossing. When it is assumed that no crossing occurs at the Fermi level along these lines, the edge state can form the Fermi surface as shown by the red line in Fig. 1.12 (a). Now, as we know Fermi surface in the quarter of surface Brillouin zone, the whole Fermi surface can be clearly understood with TRS shown by bold green line in Fig. 1.12(c). Here, we should note that the odd number of Fermi surface and the spins are oriented along tangential direction of the Fermi surface.

In fact, to know the number of Fermi surfaces it is meaningful to deter-

Odd-time crossing ($\delta_i = -1$)	Even-time crossing ($\delta_i = 1$)
$\delta_a\delta_b$=-1 ($\overline{\Gamma}_a$ to $\overline{\Gamma}_b$)	$\delta_b\delta_d = 1$ ($\overline{\Gamma}_b$ to $\overline{\Gamma}_d$)
$\delta_a\delta_c$=-1 ($\overline{\Gamma}_a$ to $\overline{\Gamma}_c$)	$\delta_c\delta_d = 1$ ($\overline{\Gamma}_c$ to $\overline{\Gamma}_d$)
$\delta_a\delta_d$=-1 ($\overline{\Gamma}_a$ to $\overline{\Gamma}_d$)	

Table 1.2: Odd- or Even-times Fermi energy crossing along the high symmetry line.

mine the Z_2 topology in the three-dimensional case. For the odd (even) number of Fermi surface, Z_2 should also be odd (even) and the system can thus be classified into the topological "non-trivial" ("trivial") in three-dimensional system. Fig. 1.12 (d) shows the band structure along the cut 2 line in Fig1.12(c) and it is found that the spin-up and spin-down bands cross to each other at TRIMs, and there will be linear dispersions around the TRIM. Thus, its linear dispersion forms a Dirac cone like energy dispersion. In contrast to the Dirac cone of Graphene, it should be noted that the Dirac fermion in the topological insulator is described with the real spin instead of the pseudo-spin in Graphene. As a consequence, the Dirac fermion in topological insulator can couple to the magnetic field, which is expected to provide us with a fertile playground to study the intriguing quantum electromagnetic dynamics as well as the realization of the high performance spintronic devices.

1.3 Prototypical topological insulators

L. Fu and *C.-L. Kane* performed parity analysis of Z_2 topological invariants on several materials and finally found that $Bi_{1-x}Sb_x$ alloy is a candidate for topological insulator in which the odd number of surface states are predicted on the surface [18]. It was experimentally verified for the first time in 2008 by *Hasan*'s group [19]. However, since the surface states in the compound crosses the Fermi energy five times, the Fermi surface of the state is very complicated, which would results in the multichannel electron scattering even under the time-reversal symmetry. In fact, *Yazdani*'s group observed the electron scatterings in $Bi_{1-x}Sb_x$ with STM and STS measurements although the scattering from k to $-k$ is restricted [20]. Therefore, the materials that possesses a single surface state was strongly anticipated. In 2009, *S.-*

C. Zhang's group theoretically predicted that Bi_2Se_3, Bi_2Te_3, Sb_2Te_3 are candidates for the topological insulator and possess a single Dirac cone like surface state [21]. At the same year, it has been independently confirmed that Bi_2Se_3 and Bi_2Te_3 possess a single topological surface state by *Hasan*'s group [22] and *Z.-X. Shen*'s [23] group. Owing to the existence of a single Dirac cone, Bi_2Se_3 and Bi_2Te_3 are considered as prototypical topological insulators, and thus many theoretical and experimental efforts are exerted on the surface of the material. Especially, Bi_2Se_3 has a large bulk band gap ∼300-350 meV, which is a great advantage as a TI if one considers realistic applications [22]. With this reason, Bi_2Se_3 has been regarded as the most promising TI.

1.3.1 Crystal structure
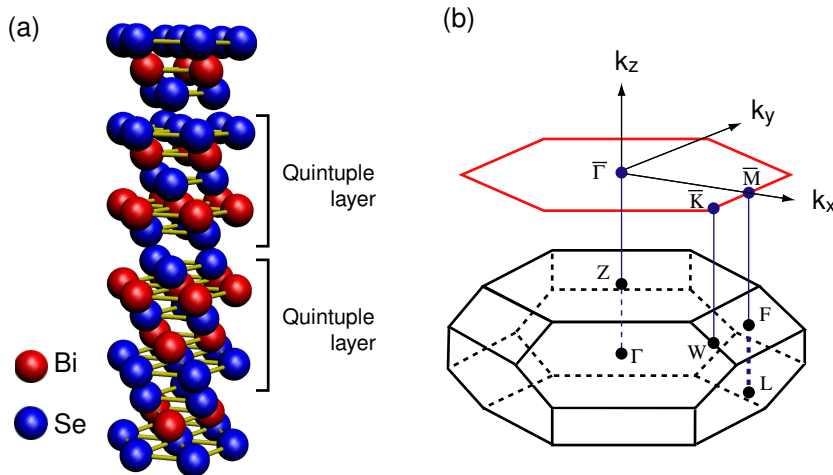
Figure 1.13: (a) Crystal structure of Bi_2Se_3 and (b) its Brillouin zone.

A_2B_3 (A:Sb, Bi, B: Se, Te) family of materials possesses the tetradymite crystal structure as shown in Fig. 1.13(a). This type crystal structure can be categorized into the rhombohedral structure with the space group D_{3d}^5 ($R\bar{3}m$). Characteristically, the crystal has a layered structure, where the five-atomic-layer blocks (Se1-Bi-Se2-Bi-Se1), so-called "quintuple layer (QL)" are stacked along z direction. It should be noted that the chemical bonding between the QLs is a van-der-Waals type while the strong bonding within

the QLs. Therefore, the clean surface of these compounds can be easily obtained by cleaving of the crystal and the cleaved surface always consist of outer Se atoms in the QL. The Brillouin zone (BZ) of this lattice is shown in Fig. 1.13.

1.3.2 Model Hamiltonian
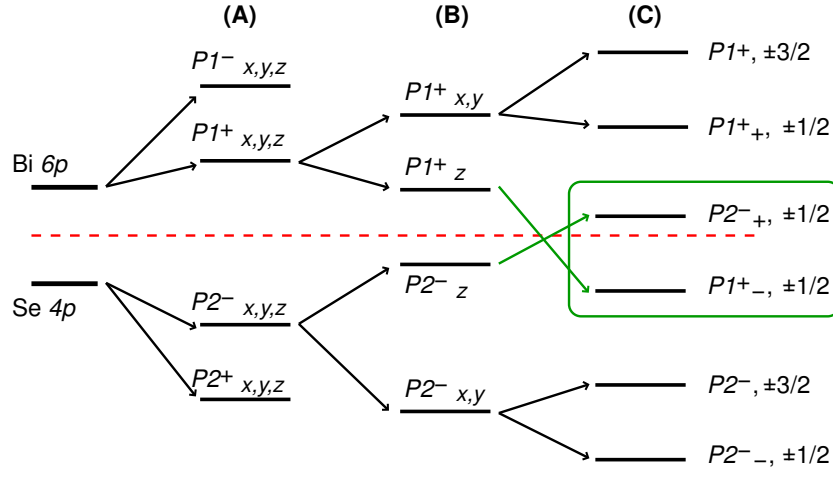
Figure 1.14: Schematic energy diagram from the atomic $p_{x,y,z}$ orbitals of Bi and Se of Bi_2Se_3 at the Γ point. There is three different step (A), (B) and (C) that represent the effect of chemical bonding, crystal-field and SOC. The dashed line represents the Fermi energy. This figure of the energy diagram is from Ref [21].

Here, we introduce the model Hamiltonian of the bulk state in Bi_2Se_3, which has been developed by *S.-C. Zhang et al.* with a parity consideration [21, 24]. At first, we show the energy diagram at the Γ point of Bi_2Se_3 in Fig. 1.14. The electron configuration of Bi is $6s^2 6p^3$ and that of Se is $4s^2 4p^3$. Since the outer shell is p state in both atoms, s state can be neglected. For the atomic state, the Bi $6p$ state is located at higher energy than that for the Se $4p$ state. Considering the chemical bonding within the QLs, one can find the strongest chemical bonding between Se and Bi atoms, resulting in the energy splitting where the Bi states are pushed up, while the Se states pulled down. Because of the inversion symmetry in the crystal, these states can be considered as bonding ($|P1^+>$, $|P2^+>$) and anti-bonding ($|P1^->$,

$|P2^->$). Now, one can define the parity (+ or −) of these states. The energy diagram of both states is shown in region (A) in Fig. 1.14 in which the anti-bonding state has higher energy than the bonding state. Then, in the layered crystal structure, the perpendicular direction to the surface (z) is environmentally different from the in-plane direction (x, y) so the energy level for p_z separates from the p_x and p_y for all states. Thus, the energy level is turned into the region (B) in which the state of $|P1_z^+>$ mainly forms the conduction band while the state of $|P2_z^->$ forms the valence band. These energy levels are finally interchanged when the SOC is turned on as shown in the region (C) in Fig. 1.14. Since the both states have opposite parity, this swapping of energy levels leads to a band inversion at Γ point. This is a simplified picture of the topological insulator phase transition in Bi_2Se_3. After the band inversion, the bulk conduction and valence bands are dominated by $|P2_+^-, \pm\frac{1}{2}>$ and $|P1_-^+, \pm\frac{1}{2}>$. Generally, the SOC can mix the $p_{x(y)}$ orbital with the p_z orbital and entangle the orbitals with the spins, ↑ and ↓. However, *S.-C. Zhang et al.* pointed out that the energy splitting between $p_{x(y)}$ and p_z states is higher than the energy scale of SOC and thus the eigenfunctions near the bulk energy gap are governed by the p_z sates. Finally, they developed the model Hamiltonian using the 4×4 matrix for the bulk states within the bulk energy band gap as follows:

$$H_{eff} = \epsilon_k + \begin{pmatrix} M(\boldsymbol{k}) & B(k_z) & 0 & A(k_\parallel k_-)) \\ B(k_z) & -M(\boldsymbol{k}) & A(k_\parallel k_-)) & 0 \\ 0 & A(k_\parallel k_+)) & M(\boldsymbol{k}) & -B(k_z) \\ A(k_\parallel k_+)) & 0 & -B(k_z) & -M(\boldsymbol{k}) \end{pmatrix}$$

$$+ \frac{R_1(k_+^3 + k_-^3)}{2} \begin{pmatrix} 0 & i & 0 & 0 \\ -i & 0 & 0 & 0 \\ 0 & 0 & 0 & i \\ 0 & 0 & -i & 0 \end{pmatrix} + \frac{R_2(k_+^3 - k_-^3)}{2} \begin{pmatrix} 0 & -i & 0 & 0 \\ -i & 0 & 0 & 0 \\ 0 & 0 & 0 & i \\ 0 & 0 & i & 0 \end{pmatrix}$$

$$(1.24)$$

where the basis functions are $|P1_-^+, +\frac{1}{2}>, |P2_+^-, +\frac{1}{2}>, |P1_-^+, -\frac{1}{2}>, |P2_+^-, -\frac{1}{2}>$ and the details of the parameters are explained in Ref [24]. Since the band inversion occurs at the Γ point ($\boldsymbol{k}$=0), one only has to consider the diagonal components ($M_k=M_0+M_1k_z^2++M_2k_\parallel^2$), which includes the energy scale of SOC and can determine the energy level at the Γ point. Figure 1.15(a)-(c) shows the obtained band dispersions using the effective Hamiltonian in Eq. (1.24) when M_0 is set to (a) +1.0, (b) 0 and (c) −2.8, respectively. The
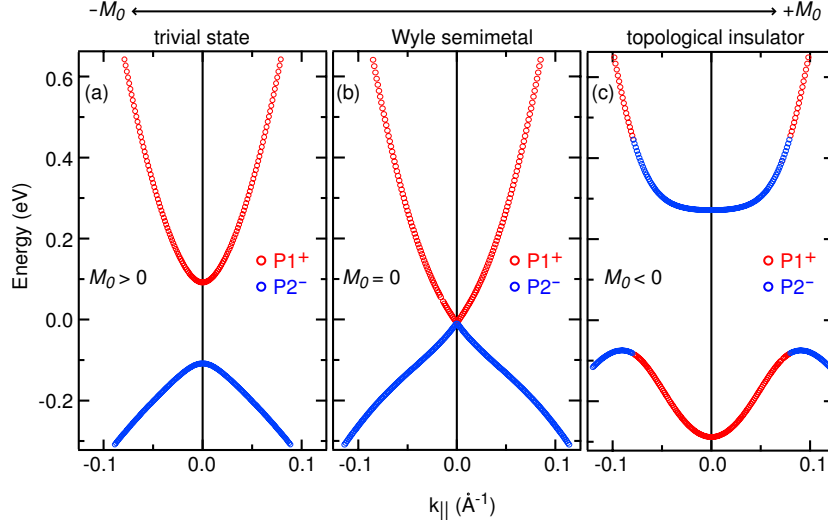
Figure 1.15: Calculated bulk band structure with the model Hamiltonian Eq. (1.24) where M_0 is (a) positive, (b) 0 and (c) negative. The same parameters are used as those listed in Ref. [24]. Red and blue colored circles indicate the bands dominated by $|P1_-^+, +\frac{1}{2}>$ and $|P2_+^-, +\frac{1}{2}>$ states, respectively.

other parameters are fixed at the same values as those listed in Ref. [24]. For simplicity, k_z and θ are assumed to be 0. Red and blue colored circles indicate the bands dominated by $|P1_-^+, +\frac{1}{2}>$ and $|P2_+^-, +\frac{1}{2}>$ states, respectively and the other basis states are neglected. In the negative M_0 region (Fig. 1.15(a)), the conduction and valence bands form parabolic energy dispersions, that is, a massive Dirac cone like energy dispersion in which the state with positive parity has larger energy than the negative parity state at all $k_\parallel$. However, this situation is changed if M_0 becomes negative as shown in Fig. 1.15(c). In particular, the basis states are switched around 0.8 $\mathring{A}^{-1}$ in the bands and the M-shaped energy dispersion appears in the valence band. These features are signatures of a band hybridization owing to the band inversion. Importantly, between the two situations, the energy gap must close at once with M_0 as demonstrated in Fig. 1.15(b). Thus, these results indicate the different Z_2 topological invariant between the states with the positive and negative M_0, which is quite similar to the parity anomaly. The gapless feature of the bulk sate is called Dirac semimetal in which a spin degenerate massless Dirac fermion is realized in the bulk.

Next we focus on the electronic structure of the surface (edge) state with the effective Hamiltonian developed by groups led by *L. Fu* and *S.-C. Zhang* independently [24, 25]. They solved the eigenvalue problem of the Hamiltonian and found that the eigenenergy is expressed as:

$$E_\pm = C_0 + C_2 k_\parallel^2 \pm \sqrt{A^2 k_\parallel^2 + 4R^2 k^6 cos^2 3\theta} \tag{1.25}$$

where C_0 determines the energy offset at $\overline{\Gamma}$ and A, C_2, R are the constants of liner (k), quadratic (k^2) and cubic (k_3) terms, respectively. The notation of $+$ $(-)$ indicate the energy state above (below) the Dirac point, the so-called upper (lower) Dirac cone. Then, the spin polarizations can be also evaluated as:

$$< \Psi_+ |\sigma_x| \Psi_+ > = \frac{2Ak_y}{N}(d_+ - 2Rk^3 cos3\theta)$$

$$< \Psi_+ |\sigma_y| \Psi_+ > = -\frac{2Ak_x}{N}(d_+ - 2Rk^3 cos3\theta) \tag{1.26}$$

$$< \Psi_+ |\sigma_z| \Psi_+ > = \frac{4Rk^3 cos3\theta}{N}(d_+ - 2Rk^3 cos3\theta)$$

where $d_\pm = \pm\sqrt{A^2 k_\parallel^2 + 4R^2 k^6 cos3\theta}$ and $N{=}A^2 k^2{+}(\sqrt{A^2 k_\parallel^2 + 4R^2 k^6 cos3\theta} - 2Rk^3 cos3\theta)^2$. The energy dispersion and spin polarization obtained with Eq. (1.25) and Eq. (1.16) are shown in Fig. 1.16. The parameters listed in Ref. [24] are used for the simulation. Around Brillouin zone center ($k_\parallel{=}0$), the gapless Dirac cone like energy dispersion is reproduced. In going away from the center, the shape of the constant energy contours (CECs) are hexagonally deformed by the k-cubic term. The CECs at several energies are shown in Fig. 1.16(b) denoted with black lines. Near $k{=}0$, the Dirac cone like surface state forms the isotropic CEC while the shape of CEC deforms into the hexagon shape at slightly far from the center point. When k is further increased, the hexagram shape of CEC is formed. The hexagonal deformation of CEC is called hexagonal warping effect, which is firstly pointed by *L. Fu* in 2010. It should be noted that the hexagonal warping effects can contribute not only to induce the deformation of CECs but also lead to the out-of-plane (z) spin polarization. The z spin polarizations for each k-point are shown in the k_x-k_y map (Fig. 1.16(b)). One can find that the z spin polarization is developing with increasing the CEC deformation. As a result of a mirror symmetry along $\overline{\Gamma}$-$\overline{M}$ high-symmetry line, the z spin polarization is strictly
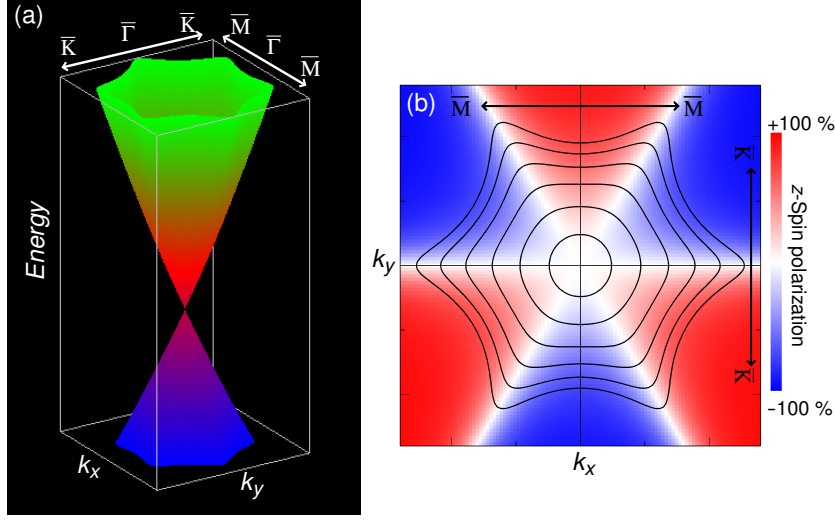
Figure 1.16: (a) Calculated surface band structure reproduced with the effective Hamiltonian describe in Eq. (1.25). (b) Constant energy contours at several energies with out-of-plane spin components by hexagonal warping effect.

0, while the maximum z spin polarization appears in $\bar{\Gamma}$-$\bar{K}$ line. Due to the term of $cos3\theta$ in Eq. (1.16), which is a consequence of the three-hold symmetry of the bulk, the z spin polarization should be antisymmetric with the $60°$, $180°$, $300°$ azimuthal rotations.

1.3.3 Experimental observation of electronic structures in the topological insulators

In order to verify that the materials are the topological insulators, one has to probe an existence of odd number of topological surface states within the bulk energy gap. The experimental verification can be done only with the angle-resolved photoemission spectroscopy (ARPES). Figure 1.17(a) and (b) show the observed Dirac cone like topological surface state along the $\bar{\Gamma}$-$\bar{M}$ direction in Bi_2Se_3 [22] and Bi_2Te_3 [23], respectively and their Fermi surfaces (FS). Apparently, it is found that the bulk conduction band (BCB) crosses the Fermi energy in both materials. This fact is known as a result of a spontaneous electron doping effect due to the chalcogen site vacancies in the as-grown bulk samples. The spin helical textures in these compounds have

(a) Bi$_2$Se$_3$
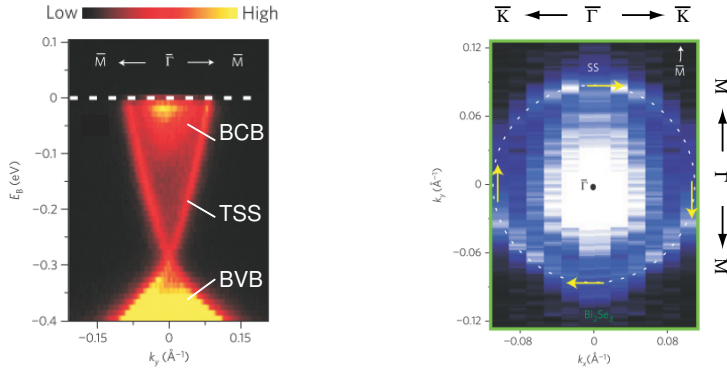
(b) Bi$_2$Te$_3$
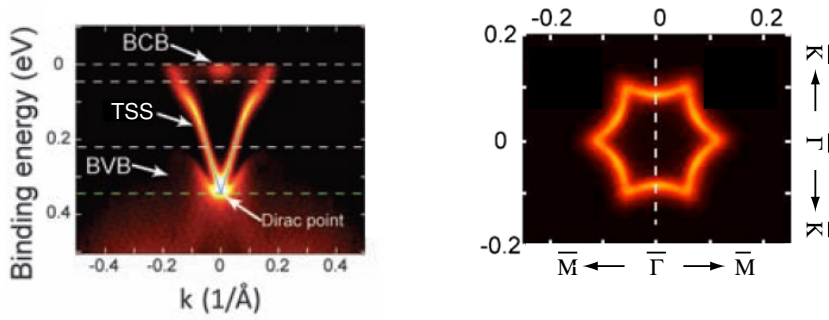
Figure 1.17: Previous ARPES results on the typical topological insulators, (a) Bi$_2$Se$_3$ [22] and (b) Bi$_2$Te$_3$ [23].

been confirmed by spin-resolved ARPES measurements [26, 27].

Though the Fermi surface of Bi$_2$Se$_3$ seems not clear as shown in Figure 1.17(a), it has been believed that Bi$_2$Se$_3$ has nearly ideal Dirac cone which shows a isotropic dispersions. On the other hand, hexagram shaped Fermi surface has been observed in the surface state of Bi$_2$Te$_3$, which is known to be due to the hexagonal warping effect as introduced in Sec 1.3.2. This effect deforms the shape of constant energy contour from a circle near the Dirac point to the hexagonal shape in going far from the Dirac point due to the crystal potential and induces the out-of-plane spin component.

The existence of perpendicular spin component along $\bar{\Gamma}$-$\bar{K}$ symmetry line has already been confirmed by SARPES measurement in Bi_2Te_3 [27].
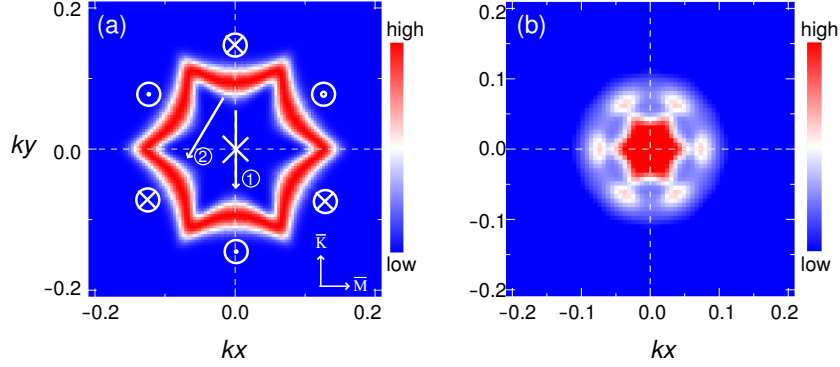
Figure 1.18: Simulation of the scattering pattern in heavily warped system. (a) Hexagram constant energy contours with the out-of-spin components. Arrows represent the possible nesting vector. (b) Simulation of the scattering pattern with Eq. (1.27) and (1.28).

Beside their band structure, $Q.$-$K.$ Xue's group experimentally demonstrated an existence of anisotropic electron scattering on the surface of Bi_2Te_3 in which the most of electron scatterings is absent along $\bar{\Gamma}$-$\bar{M}$ line but it happens in $\bar{\Gamma}$-$\bar{K}$ line even under the TRS [28]. Shortly after the experimental demonstration, its theoretical interpretations were provided by $L.$ $Fu.$ He stressed that the hexagonal warping effect can open electron scattering channel through the nesting of constant energy contour and the z spin components, which gives the anisotropic scattering pattern. For a circular Fermi surface, the electrons cannot be back-scattered in the presence of the TRS. However, for a hexagram shape as shown in Fig. 1.18(a), the nesting vectors on the Fermi surface induces the new scattering channels denoted with arrows-1 and -2 in the figure. The electron back-scattering from k to $-k$ (arrow-1) is strictly forbidden even if the z spins are considered because the z spins are aligned anti-parallel due to the presence of TRS. However, the scattering denoted with arrow-2 will be opened because the z spin components are aligned parallel to each other. Furthermore, with an assistance from the strong nesting along this direction in the hexagram shaped CEC, the back-scattering probability of arrow-2 can be high. To reproduce the scattering vector map, the spin-dependent scattering probability (P_{SSP}) is

defined as:

$$P_{SSP} = \int I(\boldsymbol{k})T(\boldsymbol{q},\boldsymbol{k})I(\boldsymbol{k}+\boldsymbol{q})d^2\boldsymbol{k} \tag{1.27}$$

where $\boldsymbol{q}$ is a scattering vector, $I(\boldsymbol{k})$ is a density of state at k. $T(\boldsymbol{q},\boldsymbol{k})$ is spin-dependent transition probability including the spin vectors at $\boldsymbol{k}$ ($\boldsymbol{S}(\boldsymbol{k})$), which can be expressed as:

$$T(\boldsymbol{q},\boldsymbol{k}) = |<\boldsymbol{S}(\boldsymbol{k})|\boldsymbol{S}(\boldsymbol{k}+\boldsymbol{q})>|^2 \tag{1.28}$$

The obtained scattering vector map obtained with the Eq. (1.27) and (1.28) from Fig. 1.18(a) is shown in Fig. 1.18(b). It is found that this simulation can reproduce the experimental result quite well [28]. Accordingly, to suppress back scatterings, the topological surface state should have a more liner energy dispersion as well as th isotropic Fermi surface.

1.3.4 Possible Orbital-Spin texture

Soon after the discovery of the topological insulators, the electron spin in the topological surface state is considered to accompany the spin-helical texture in k-space with 100% spin polarization. This idea is originated from Ref [21] showing an idea that the p_z states dominate both of the bulk conduction and valence bands even if the strong SOC mixes the orbitals with the spins. This is because the energy level of $p_{x,(y)}$ state are energetically far from the p_z due to the strong crystal field. Therefore, the basis functions forming the topological surface state are generally assumed to be the p_z orbitals and thus this can create the 100% spin polarized states. Nevertheless, *J. E. Moore* and *S. G. Louie* theoretically reinvestigated on the topological surface states in the tetradymite compounds and finally proposed that the strong spin-orbit entanglement can reduce the spin-polarization of their surface states to ∼50% [29]. Their prediction is actually consistent with the experimentally observed spin polarization of ∼50-70% obtained [26]. Nowadays, the both facts of the spin-orbital entanglement and less than 100% spin polarizations are widely accepted.

Beside the spin polarization, *C.-Y. Kim*'s group proposed the realization of the spin-orbital texture in k-space as a consequence of the spin-orbit entanglement by the strong SOC [30]. The orbital angular momentum (OAM) is generally quenched by the crystal field but it can be recreated through the total angular moment (j). According to the *ab-initio* calculation as we explained in Fig. 1.14, the wave function forming the topological surface state

in Bi_2Se_3 is the $|j=1/2>$ state where the orbital (l) and spin (s) are coupled in anti-parallel as described as follows:

$$|\pm> = u_{\pm}(|p_x,\downarrow> \pm i|p_y,\downarrow>) \pm v_{\pm}|p_z,\uparrow> \qquad (1.29)$$

where $\pm$ indicate $j_z = \pm\frac{1}{2}$ that is corresponding to the upper (lower) Dirac cone, and u (v) is the coefficient of the in-plane (the out-of-plane) orbital. They found that the local OAM in a Bloch state can produce an asymmetric charge distribution (an electric dipole) in z direction near the surface. As a consequence of the dipole interaction, the OAM is strongly locked by k, which results in helical OAM texture. The spins are now coupled with the OAM by the strong SOC so that it can form the helical spin texture can be formed as a secondary effect trough helical OAM texture.

This spin-orbital texture model was furtherer developed by *S.-C. Zhang* [31]. They analyzed the basis wave function for the surface state using $k{\cdot}p$ method to quantitatively include p_x and p_y contributions within a first-order. Finally, they obtained the basis wave function with $k^{(1)}$ term as follows:

$$
\begin{aligned}
|+> = (u_0 - v_1 k)|p_z, CW> &- \frac{i}{\sqrt{2}}(v_0 - u_1 k - w_1 k)|p_r, CW> \\
&+ \frac{1}{\sqrt{2}}(v_0 - u_1 k + w_1 k)|p_t, CCW> \\
|-> = (u_0 + v_1 k)|p_z, CCW> &+ \frac{i}{\sqrt{2}}(v_0 + u_1 k + w_1 k)|p_r, CCW> \qquad (1.30)\\
&- \frac{1}{\sqrt{2}}(v_0 + u_1 k - w_1 k)|p_t, CW>
\end{aligned}
$$

where u_0, v_0 are the coefficients of the zeroth-order wave functions and u_1, v_1, w_1 are for the first-oder ones. CW and CCW indicate the spin textures in clock-wise and counter clock wise direction, p_r and p_t are radial and tangential orbital textures. Fig. 1.19 shows the spin-orbital textures obtained from the Eq. (1.30) for (a) p_z, (b) p_r and (c) p_t states in $|+>$. p_z orbitals have CW spin texture for the upper Dirac cone. In contrast, the in-plane orbitals (p_x and p_y orbitals) shows characteristic features. For the upper Dirac cone of surface states, a radial orbital texture is coupled to the same spin texture as that for p_z orbitals but a tangential one is coupled to a CCW spin texture, which results in less than 100% spin polarization. It is clear from

41
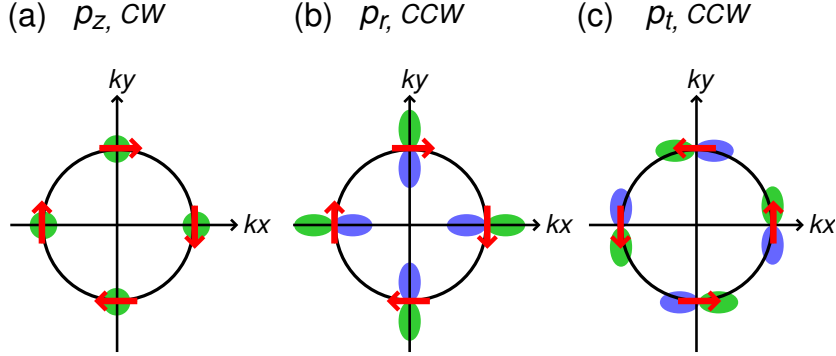
Figure 1.19: Predicted entangled spin texture for the upper Dirac cone [31]. (a) p_z orbital texture coupled with the clock-wise spin texture (CW). (b) Radial orbital (p_r) texture with the clock-wise spin texture (CW) (c) Tangential orbital (p_t) texture with the counter-clock-wise spin texture (CCW).

Eq. (1.30) that the coupling between spin and orbital textures is completely antisymmetric at upper and lower Dirac cones. The total spin polarization which depends on the weights of $p_{x,y,z}$, has been figured out with *ab-initio* calculation by *S.-C. Zhang* group. The result has shown that the p_z orbitals (50 %) dominate the states near the Dirac point with each in-pane orbital only around 30 %. Therefore, the net spin texture shows CW for the upper Dirac cone and CCW for the lower Dirac cone, the same as that of p_z orbitals, as well as the total angular momentum texture. The possible orbital textures has been experimentally investigated by the ARPES measurement probing the linear polarization dependences by *Dessau*'s group [32]. However, the orbital texture dependence of the spin textures is still under discussions.

1.3.5 Transport properties

By now, as a foothold to study intriguing phenomena by the topological surface state, so many experimental efforts have been paid to obtain the transport properties of the surface state. However, as mentioned in Sec 1.3.3, the as-grown bulk samples generally shows the metallic bulk features confirmed by ARPES measurements, which causes unfavorite situations that the transport properties is dominated by the bulk state and thus the surface properties is hardly observed [33]. With these reasons, the first issue for studying the

topological insulators is to develop a methodology for the fabrication of the bulk insulator phase. One of the basic ideas to overcome this issue is to dope holes or electrons into the bulk crystal with impurities [34]. However, in spite of the efforts, the bulk metallic feature dominates the transport properties even if ARPES results show that the Fermi energy is located within the energy gap [35].

The surface transport properties has been firstly observed for Bi_2Te_3 by *R. J. Cava-N. P. Ong* group [36]. In contrast to the bulk crystal of Bi_2Se_3 with Se-site vacancies, the anti-site defects mainly contribute to the spontaneous carrier doping in the crystal of Bi_2Te_3 with a compositional gradient. Therefore, it has become possible to obtain the nonmetallic crystal with a nearly stoichiometric chemical composition and to measure the surface quantum transport. However, the resistivity is still low $\sim$12 mΩcm and the surface contribution to the transport did not exceed $\sim$0.3 % [37].

In 2010, *Y. Ando et al.* has found that a tetradymite material, Bi_2Te_2Se with the basic quintuple layer unit of Te-Bi-Se-Bi-Te is a fascinating platform to study the surface transports with a high resistivity exceeding 1 Ωcm. In this compound, it can be expected that the defects can be suppressed by the characteristic crystal structure, which results in the nonmetallic feature during the sample growth. Finally, high surface contribution $\sim$6 % was achieved with this compound, which is $\sim$20 times larger than that in Bi_2Te_3. They have successfully made the nonmetallic bulk sample also in the tetradymite crystal with a solid solution, $Bi_{2-x}Sb_xTe_{3-y}Se_y$. With variable compositions, they found that there is an adequate compositions in which the acceptors and donors compensate and thus present a bulk insulating phase. In the series, the surface contribution is estimated to be $\sim$5 % which is comparable to that for Bi_2Te_2Se [38].

Chapter 2

Experimental Methods

2.1   Angle-resolved photoemission spectroscopy

2.1.1   Overview
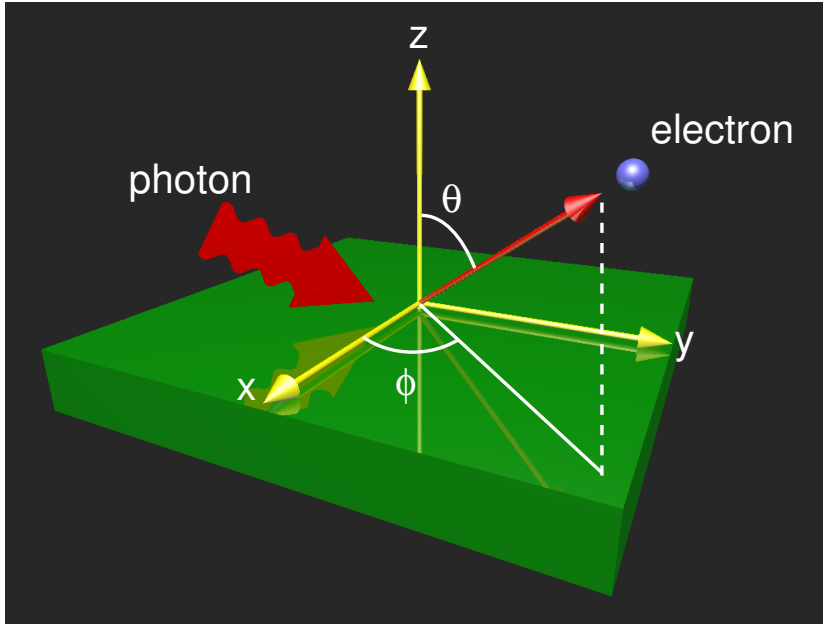
Figure 2.1: Schematic image of angle resolved photoemission spectroscopy.

Electron behaviors in solids play an important role in various physical properties like electronic, thermal resistivities and magnetism. To understand and control the intriguing properties of materials, it is therefore important to know the electronic structure. Angle-resolved photoemission spectroscopy (ARPES) is a very powerful experimental technique to meet the requirement because ARPES can probe the electronic states of materials in energy and momentum axes. Figure 2.1 represents schematic image of ARPES measurement, where photoelectrons are emitted by incident light and then detected by an electron analyzer with their kinetic energy (E_{kin}) and emission angles. Thus, ARPES basically measures intensity of photoelectrons (I) as a function of E_{kin} and θ, i.e. $I(E_{kin}, \theta)$ that can be actually transformed into the relation $I(E_B, \boldsymbol{k})$ with basic formulas as follows:

$$E_{kin} = h\nu - E_B - \Phi \qquad (2.1)$$

46

$$\boldsymbol{k}_{\parallel} = \sqrt{\frac{2m}{\hbar^2}}\sqrt{E_{kin}}sin\theta \qquad (2.2)$$

$$\boldsymbol{k}_{\perp} = \sqrt{\frac{2m}{\hbar^2}}\sqrt{E_{kin}cos^2\theta + V_0} \qquad (2.3)$$

where $h\nu$, Φ represent a photon energy of incident light and vacuum level of the material, $k_{\parallel}$, $k_{\perp}$, V_0 indicate momentum of electron in-plane and out-of plane components and inner potential, respectively. Details of these basic formulas are introduced in Sec. 2.1.2 and Sec. 2.1.5.

An electron analyzer is considered as an important part of ARPES measurement because both energy and angular resolutions are basically determined by a performance of the analyzer. After development of high performance modern spectrometer equipped with a two-dimensional micro-channel plate (MCP) and CCD camera, the use of ARPES technique is further spread out for the research of condensed matter physics. This high performance detector allows to measure $I(E_{kin}, \theta)$ spontaneously and the realization of E_{kin}-θ parallel measurement, i.e. E_B-$\boldsymbol{k}$ parallel, has improved high energy and angular resolutions for ARPES measurement. This type of electron analyzer is further explained in Sec. 2.1.6.
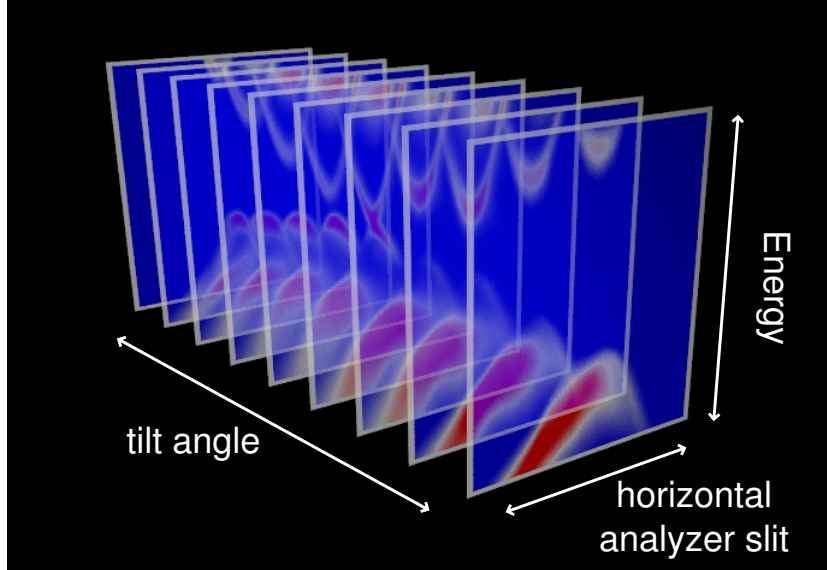
Figure 2.2: Schematic image of constant energy contour mapping with multi-channel ARPES combined with multi-axis goniometer.

Using the multi-channel analyzer combined with a multi-axis goniometer, the constant energy mapping can be effectively performed. Figure 2.2 shows a schematic view of the constant energy contours mapping. Thanks to the multi detection ability of the analyzer, the E-k_x (θ) can be acquired at once. If the sample are rotated in the perpendicular direction to the k_x using goniometer, one can access energy dispersion in k_y (ϕ) direction as well and finally obtain the volume image E-k_x-k_y including the information of the constant energy contours.

In addition, it should be noted that one can access also E-k_z dispersion if a tunable photon such as synchrotron radiation is applied as the incident light, which thus means that one can determine the entire electronic structure in three dimensional momentum axes. Two-dimensional state such as surface state of solids depends only in-plane momenta while three-dimensional bulk state basically is dispersive with respect to the k_z. Therefore, from the results acquired with different photon energies, the surface and the bulk origin can be identified.

Owing to these great aspects of ARPES measurement combined with synchrotron radiation, this method has so far been applied for various condensed matter systems [39], such as superconductors, strong-correlated electron systems, low dimensional systems and various intriguing surface states.

2.1.2 Basic concepts of photoemission spectroscopy

Photoemission spectroscopy (PES) is widely known as an powerful technique to directly investigate the electronic structure. This technique is based on the photoelectric effect that was firstly discovered more than one hundred years ago and the theoretical explanation was proposed by *Albert Einstein* who thus won the Nobel Prize in Physics in 1921. Figure 2.3 represents a schematic image of the principle of PES experiment. The kinetic energy (E_{kin}^{vac}) of photoelectrons emitted from the solid to the vacuum via the photoemission process is determined by the energy of photons ($h\nu$), the binding energy (E_B) of the electron and the work function (Φ) of the materials following the energy conversation rule as described in as equation:

$$E_{kin}^{vac} = h\nu - E_B - \Phi \tag{2.4}$$

where E_B is the measured from the Fermi energy (E_F). To simplify the PES method, the photoemission process is generally approximated with *three-step*
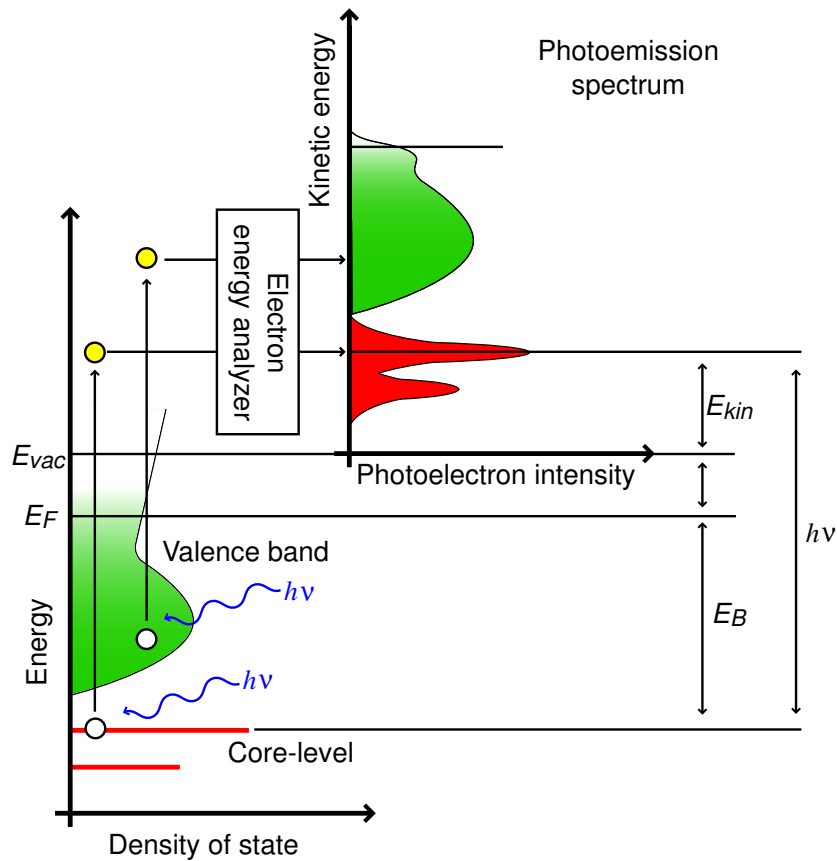
Figure 2.3: Schematic energy diagram of photoemission spectroscopy.

model. In the model, the process can be separated into three independent processes:

(i) Locally electrons are excited from an initial to a final state by the photons.

(ii) Excited electrons in the final state travel through the bulk to the surface with elastic and inelastic scatterings.

(iii) Electrons go out into the vacuum and then are detected.

With these processes separately, important concepts of PES measurement can be extracted. Firstly, one can imagine that the process (i) can be described by coupling between a final state and an initial state as described

with an Hamiltonian describing polarized light-matter interaction. In fact, by simplifying the coupling between initial and final state described with a matrix element, a further diverse features of PES can be understood, which will be discussed in Sec. 2.1.3. Secondly, the process (ii) indicates that the only excited electrons located within a specific depth in the bulk are able to reach the surface while the others are inelastically scattered before reaching and partially contribute to intensity backgrounds. Therefore, the surface sensitivity of the PES measurement should be always considered to interpret the experimental results. We will introduce the inelastic mean free path of photoelectrons in 2.1.4. Finally, the process (iii) can give a picture of the momentum conservation rule during photoelectron emission from the surface, which leads a very important principle of ARPES. We will further discuss the process in 2.1.5.

2.1.3 General formulations

The most general and widely utilized theoretical description of PES is based on Fermi's golden rule in a dipole approximation. The intensity of photo-electrons (I) is the result of a photon induced excitation system from the ground state $|\psi^i>$ into a final state $|\psi^f_n>$ denoted with quantum number n as described below:

$$I(E_B) \propto \sum_n | < \psi^f_n | H_{PES} | \psi^i > |^2 \delta(h\nu - E_k - E_B - \Phi) \qquad (2.5)$$

where Delta function indicates energy conservation rule during the photoemission process, which is corresponding to the Eq. (2.4). H_{PES} describes the interaction of electrons with the electromagnetic potential ($\boldsymbol{A}$) where the momentum operator ($\boldsymbol{p}$) is transformed to $\boldsymbol{p} - \frac{e}{c}\boldsymbol{A}$. Therefore, one can obtain the expression of the Hamiltonian:

$$
\begin{aligned}
H =& \frac{1}{2m_e} \left(\boldsymbol{p} - \frac{e}{c}\boldsymbol{A} \right)^2 + eV(\boldsymbol{r}) \\
=& \frac{p^2}{2m_e} + \frac{e}{2m_e c} \left(\boldsymbol{A} \cdot \boldsymbol{p} + \boldsymbol{p} \cdot \boldsymbol{A} \right) + \frac{e^2}{2m_e c^2} A^2 + eV(\boldsymbol{r}) \\
=& H_0 + H_{PES}
\end{aligned}
\qquad (2.6)
$$

$$H_{PES} = \frac{e}{2m_e c} \left(\boldsymbol{A} \cdot \boldsymbol{p} + \boldsymbol{p} \cdot \boldsymbol{A} \right)$$

where the A^2 is ignored. The communication relation leads to the relation:

$$H_{PES} \propto \boldsymbol{A} \cdot \boldsymbol{p} + \boldsymbol{p} \cdot \boldsymbol{A} = 2\boldsymbol{A} \cdot \boldsymbol{p} + i\hbar\nabla \cdot \boldsymbol{A} \tag{2.7}$$

Especially, because of the the inversion symmetry in the solid, it is clear that $\nabla \cdot \boldsymbol{A}$=0 so that only the dipole term can remain. Therefore, one can obtain the PES intensity description as follows:

$$I(E_B) \propto \sum_n |<\psi_n^f|\boldsymbol{A} \cdot \boldsymbol{p}|\psi^i>|^2\delta(h\nu - E_k - E_B - \Phi) \tag{2.8}$$

In the VUV radiation regime below the photon energy of sub 100 eV, the wavelength is large compared to the atomic distance and therefore the electromagnetic field of photons can be approximately taken as a constant. Thus, the Eq. (2.8) can be finally rewritten into:

$$I(E_B) \propto \sum_n |<\psi_n^f|\boldsymbol{A} \cdot \boldsymbol{r}|\psi^i>|^2\delta(h\nu - E_k - E_B - \Phi) \tag{2.9}$$

where $\boldsymbol{r}$ is a position operator.
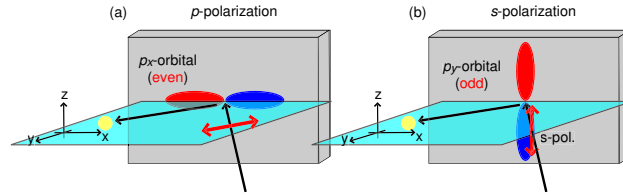
Figure 2.4: (a) *p*- and (b) *p*-polarization geometry.

The Eq. (2.9) can lead to an important aspect of PES, the selection rule of photoemission process. At first, the photoemission from p_x orbital is considered as an example, with the detector set in the mirror plane of the target. From the Eq. (2.9), the whole overlap must be an even function with respect to the mirror plane to obtain non-zero photoemission intensity. Since the final state with odd-parity would be zero everywhere on the mirror plane and therefore also at the detector, the final state wave function $\phi_f^{\boldsymbol{k}}$ should be even. In particular, at the detector the photoelectron is described by an even-odd parity plane-wave state $e^{i\boldsymbol{k}\cdot\boldsymbol{r}}$ with momentum in the mirror plane. This gives a hint that $(\boldsymbol{A} \cdot \boldsymbol{r})|\phi_i^{\boldsymbol{k}}>$ should be even. In the case where $|\phi_i^{\boldsymbol{k}}>$ is even, the photoemission process is symmetry allowed for $\boldsymbol{A}$ even or in-plane

and forbidden for $\boldsymbol{A}$ odd or normal to the mirror plane. Thus, for a initial state of either even or odd symmetry with respect to the mirror plane, the non-zero photoemission intensity is allowed in the polarization conditions as summarized bellow:

$$< \phi_f^{\boldsymbol{k}}|\boldsymbol{A}\cdot\boldsymbol{r}|\phi_i^{\boldsymbol{k}} > \begin{cases} |\phi_i^{\boldsymbol{k}} > \text{ is even} & \text{therefore } < +|+|+ > \boldsymbol{A} \text{ is even} \\ |\phi_i^{\boldsymbol{k}} > \text{ is odd} & \text{therefore } < +|-|- > \boldsymbol{A} \text{ is even} \end{cases} \quad (2.10)$$

Especially, the condition, where $(\boldsymbol{A} \cdot \boldsymbol{r})$ is even and odd, are called p- and s-light polarization, respectively (see Fig. 2.4).

2.1.4 Probing depth of photoelectrons
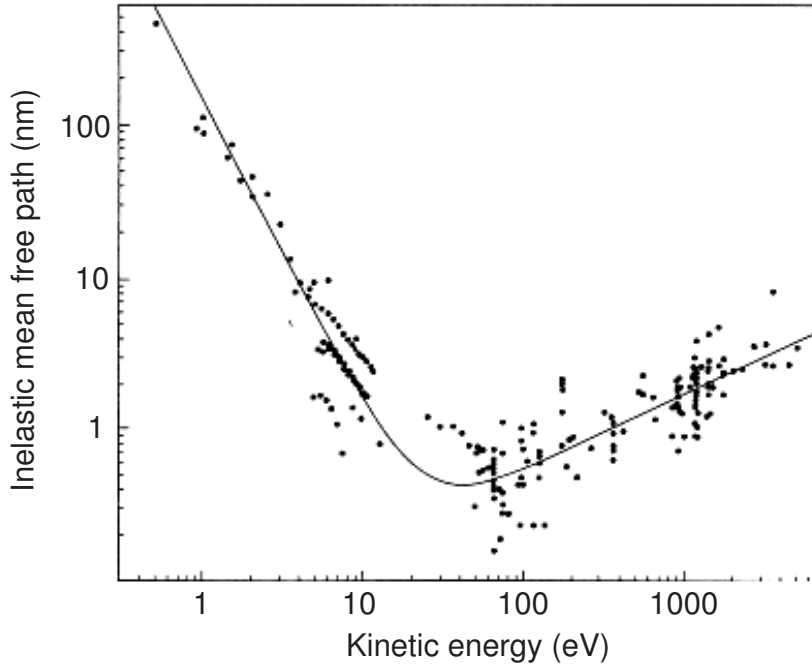
Figure 2.5: Universal curve of inelastic mean free path of photoelectron, taken from M. P. Seah [40].

The second step of three-step model as mentioned in Sec. 2.1.2 presents a photoelectron transport to the surface. At this step, the photoelectrons is scattered elastically and inelastically by electron-electron interaction. The

inelastic mean free path (IMFP) of photoelectrons strongly depends on their kinetic energy (E_k) as illustrated in Fig. 2.5 [40]. As can be seen in the curve, the photoelectrons with $E_k > 1000$ eV exhibit large bulk sensitivities, which can achieve sub nm. On the other hand, those with E_k typically around 30-50 eV are extremely surface-sensitive with its IMFP up to ~0.5 nm. Therefore, PES measurement with vacuum ultra violet (VUV) radiations is only capable of probing within the first few atomic layers of the materials. Remarkably, for the low $E_k < 10$ eV, the IMFP is prolonged due mainly to a lack of plasmon excitation. The E_{kin} dependence of the IMFP tells us that the surface sensitivity would affect the PES result and always should be considered to interpret the data.

2.1.5 Momentum conservation
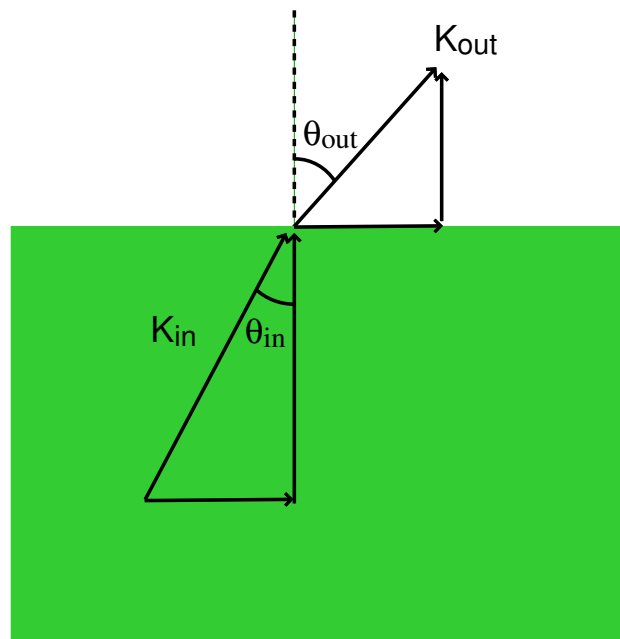
Figure 2.6: Schematic image of photoelectrons ejected through the surface. $\boldsymbol{K}_{in}$ is a momentum of excited electron in a solid and $\boldsymbol{K}_{out}$ is a momentum of detected photoelectron.

One can easy imagine that the incident photons transfer their momentum to electrons when the incident photons excite electrons in the solid and the

momentum conservation rule should be expressed below:

$$\boldsymbol{K}_f = \boldsymbol{K}_i + \boldsymbol{K}_p + \mathbf{G} \tag{2.11}$$

where $\boldsymbol{K}_{f(i)}$, $\boldsymbol{K}_p$ are the momentum of electrons in the solid as a final (an initial) state and the momentum of the photons, $\mathbf{G} = (2n_x\pi/a,\ 2n_y\pi/a,\ 2n_z\pi/a)$ is a reciprocal lattice vector, and n_x, n_y and n_z are integers. If the low photon energy below 100 eV, $\boldsymbol{K}_p$ term can be considered to be negligible and thus the momentum conservation rule in Eq. (2.11) demands vertical transition.

A schematic image of escape condition for the photoelectron trough the surface is shown in Fig. 2.6. When the electron is emitted trough the surface, the wave vector perpendicular to the surface ($\boldsymbol{K}_\perp$) can be modified by the potential barrier of the so-called inner potential (V_0) because of the discontinuous periodic potential at the surface while the wave vector parallel to the surface ($\boldsymbol{K}_\parallel$) is conserved. Therefore, the following relationship is satisfied between the wave vector parallel to the surface of the emitted electron, $\boldsymbol{k}_{f\parallel}$ and $\boldsymbol{K}_{i\parallel}$,

$$\boldsymbol{k}_{i\parallel} = \boldsymbol{K}_{f(in)\parallel} = \boldsymbol{K}_{f(out)\parallel} \tag{2.12}$$

where $\boldsymbol{k}_{i\parallel}$ is the in-plane momentum of the initial state in the solid, $\boldsymbol{K}_{f(in)\parallel}$ and $\boldsymbol{K}_{f(out)\parallel}$ are the ones of the final state in incident and emitted electrons, respectively. Since $\boldsymbol{k}_{f\parallel}$ is related to the polar emission angle θ, ϕ and the photoelectron E_{kin} through

$$\boldsymbol{k}_{i\parallel} = \sqrt{\frac{2m}{\hbar^2}}\sqrt{E_{kin}}sin\theta \tag{2.13}$$

and finally one can obtain the formula for the momentum in the perpendicular direction as follows:

$$\boldsymbol{k}_{i\perp} = \sqrt{\frac{2m}{\hbar^2}}\sqrt{E_{kin}cos^2\theta + V_0} \tag{2.14}$$

With Eq. (2.13) and (2.14), one can obtain momentum of electrons in solids. This is a basic principle of ARPES measurement.

2.1.6 Electronic Analyzer with multi channel detector

A photoelectron detector is an important part for the photoemission measurements to detect the electronic structure. Figure 2.7(a) shows a schematic
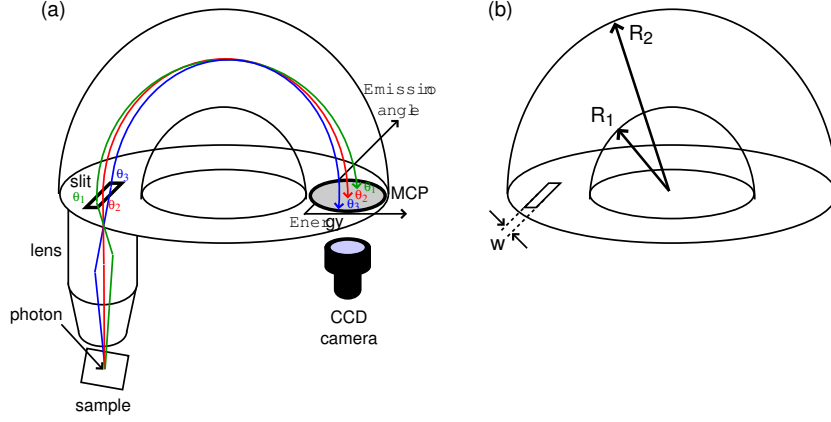
Figure 2.7: (a) Transparent image of analyzer and photoelectron trajectory. (b) Basic concepts of photoelectron analyzer. The hemispherical analyzer is constructed from the inner and outer hemispheres, where radius of hemispheres denote R_1 and R_2, respectively.

image of hemispherical analyzer with multi-channel detections. The hemispherical analyzer consists of an electric focus lens, an entrance slit, outer and inner hemispheres and a multichannel plate (MCP) with a fluorescence screen. At first, emitted photoelectrons from the surface enter the electron lens and are focused by electrostatic fields. The electron beam is decelerated by a retarding potential (V_R) before going into the hemispheres. The analyzer transmits only photoelectrons with a given energy, the so-called pass energy (E_P). Finally, the photoelectrons reach MCP and are accelerated at the fluorescent screen so that the emitted light can be detected by CCD camera. The relationship between the V_R and the E_P is given by:

$$E_P = E_{kin} - eV_P - \phi_A = \frac{eV_P}{R_2/R_1 - R_1/R_2} \qquad (2.15)$$

where ϕ_A is the work function of the analyzer, and V_P is applied voltage between inner and outer hemispherical analyzer. R_1 and R_2 indicate radius of the inner and outer hemispheres, respectively (see Fig. 2.7(b)). One can sweep E_{kin} by sweeping E_P or V_R. Then, the energy resolution ΔE is determined by the slit width ω of inner and outer hemispheres:

$$\Delta E = \frac{\omega E_P}{R_1 + R_2} \qquad (2.16)$$

In the actual experiments, E_P is usually kept as a constant and V_R is swept so that ΔE is kept as a constant and independent on E_{kin}. Previously, channeltrons were widely used as an electron detector. However, to overcome the detection efficiency of photoelectrons in the single-channeltron system, E_P or ω must be made larger, making ΔE worse according to Eq. (2.16). To improve the detection efficiency with keeping E_P, and the MCP is installed in the SCIENTA analyzers for the detector. Each channel detects photoelectrons which take different trajectories in the hemisphere, meaning that each channel detects electrons with different pass energies. By calibrating such differences, one can improve the detection efficiency without degrading ΔE worse.

2.2 Spin- and Angle-resolved photoemission spectroscopy

2.2.1 Spin Polarimeters

Spin-ARPES is an unique tool to directly probe the spin dependent electronic structure of materials with k-resolution. Basically, the experimental set-up is the same as the ARPES measurement except for the part that the spin polarimeter is located behind the electron analyzer. The principles of spin polarimeters are generally based on the spin-dependent electron scattering events, that lead to asymmetric intensities of the scattered electrons when the incident electron has non-zero spin polarization. The unknown spin polarization of the incident electron beam along a given axis ($\alpha{:}x, y, z$), P_α, is proportional to the measured normalized intensity asymmetry, A_α, between two distinct scattering channels, $I_{1,\alpha}$ and $I_{2,\alpha}$. The proportionality is generally expressed as the effective Sherman function, S_{eff}, which evaluates the spin analyzing power of the given scattering effects and thus depends on electron spin detectors. The spin polarization of incident electron beam is determined by the following equation:

$$P_\alpha = \frac{A_\alpha}{S_{eff}} = \frac{1}{S_{eff}} \frac{I_{1,\alpha} - I_{2,\alpha}}{I_{1,\alpha} + I_{2,\alpha}} \tag{2.17}$$

Here, obtained spin P_α can be described with the asymmetry between the populations of spin-up ($I_{\alpha\uparrow}$) and spin-down ($I_{\alpha\downarrow}$) electrons and as written below:

$$P_\alpha = \frac{I_{\uparrow,\alpha} - I_{\downarrow,\alpha}}{I_{\uparrow,\alpha} + I_{\uparrow,\alpha}} \tag{2.18}$$

From Eq. (2.18), the spin-up and spin-down spectra can be yielded from the following equations:

$$I_{\uparrow(\downarrow),\alpha} = \frac{1}{2}(1 \pm P_\alpha)I_{tot} \tag{2.19}$$

where I denotes total incident electrons (sum up $I_{1,\alpha}$ and $I_{2,\alpha}$).

Despite of the great advantage of the spin-resolution, due to a substantial intensity loss through the scattering process, the spin-resolved experiment is usually performed with increased analyzer slit width, which sacrifices both the energy and momentum resolutions. Nevertheless, time-consuming measurement are still required to achieve a high S/N ratio. In order to argue the

efficiency of a given spin polarimeter, one often defines the figure of merit (FOM), ϵ, given by the following equation:

$$\varepsilon = \frac{I}{I_0} S_{eff}^2 \qquad (2.20)$$

where I_0 and I are total incident electrons (sum up I_1 and I_2) and total counted electrons at the polarimeter, respectively. The statistical error of the spin polarization measurement is given by:

$$\frac{\delta P}{P} = \frac{I}{S_{eff}} \frac{\delta A}{A} = \frac{1}{\sqrt{\varepsilon I_0}} \qquad (2.21)$$

Thus, the efficiency of SARPES measurement is governed by both spin resolving power S_{eff} and scattering possibility I_0/I. Typical S_{eff} and I_0/I of the several representative spin detectors are summarized in Table. 2.1.

	spin-dependent scattering	S_{eff}	I_0/I	FOM	Ref
Compact-type Mott detector	spin-orbit	0.1-0.15	1×10^{-2}	2×10^{-4}	[41, 42, 43, 44]
SPLEED	Spin-orbit	0.1-0.15	0.27	1.5×10^{-4}	[45, 46]
VLEED	exchange splitting	0.42	0.12	1.9×10^{-2}	[47, 48, 49, 50]

Table 2.1: List of electron spin polarimeters. Typical values of effective Sherman function (S_{eff}), electron scattering probabilities (I/I_0), and total efficiencies (FOM) cited from the references indicated are summarized.

Available spin dependent scatterings for conventional spin polarimeters are commonly based on spin-orbit coupling as well as spin-exchange interactions. As summarized in Table 2.1, spin-orbit interaction are more widely applied to the spin polarimeters, such as the Mott detector, spin low energy electron diffraction (SPLEED) detector. To achieve high spin-orbit interaction, that is, the high S_{eff}, heavy materials such as Au and Th are utilized as the target and also the high operation energy 10 keV-100 keV is required because the spin-orbit interaction results from the relativistic effect [51]. Among two spin polarimeters, the Mott detector is known as a conventional spin detector for SARPES measurement and has been already commercialized by

several companies [52, 53]. Also, the spin-dependent low-energy electron scattering with the spin-exchange splitting unoccupied states of ferromagnetic materials can give us a spin resolution power. This spin polarimeter is called as very low energy electron diffraction (VLEED) spin detector. Details of Mott and VLEED type spin detectors are further introduced in Sec. 2.2.2 and 2.2.3, respectively.

2.2.2   Mott type spin polarimetry
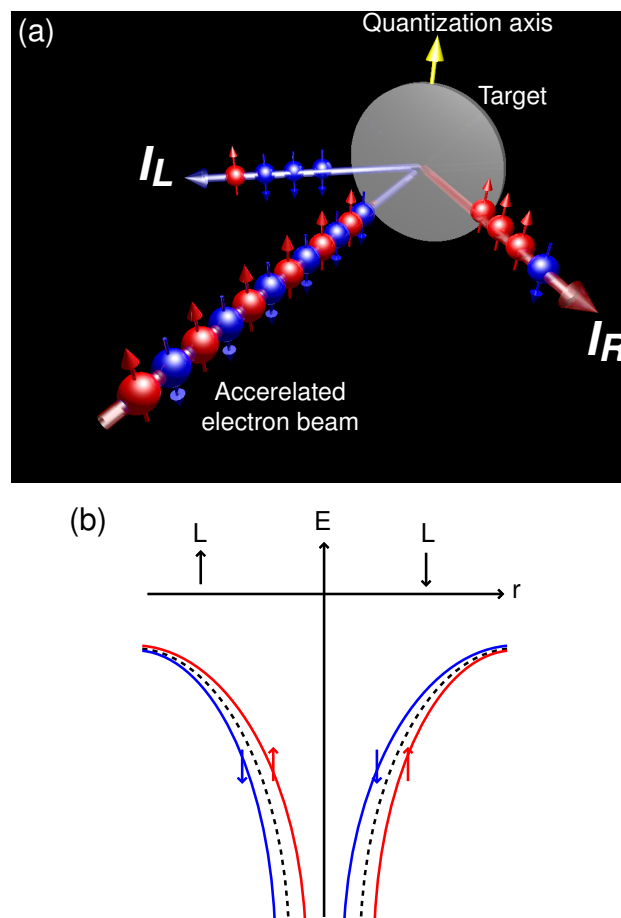
Figure 2.8: (a) Schematic illustrations of Mott scattering. (b) Spin-dependent potential of spin-orbit interaction.

Mott type spin detector is based on counting back-scattered electrons

by heavy element, where the two electron detectors are mounted on the scattering plane as shown in Fig. 2.8(a). When the incident electrons are accelerated well with high voltage $\sim$10 keV-100 keV, the electrons feel the spin-dependent potential near the nucleus of the heavy element through the spin-orbit interaction as shown in Fig. 2.8(b), which hence leads to the spin dependent probabilities of scattering to left and right directions on the scattering plane. This scattering with the strong spin-orbit interaction is called Mott scattering. Therefore, if the incident electrons are spin polarized, one can expect asymmetric electron intensity between the two channels. With the obtained asymmetry and Eq. (2.17), the spin-polarization of the incident electrons can be quantitatively evaluated. However, since there would be a asymmetric factor in each independent electron counter, it should be noted that the result can seriously be affected by the extrinsic asymmetry of the instrument itself [54]. Thus, Eq. (2.17) should be modified to the equation with the instrumental asymmetry contribution for SARPES measurement with Mott type spin detector as follows:

$$P = \frac{1}{S_{eff}} \frac{I_L - A_{inst} I_R}{I_L + A_{inst} I_R} \tag{2.22}$$

where A_{inst}, $I_{R(L)}$ are the instrumental asymmetry and the intensity of electrons counted by right (left) channels, respectively. Fortunately, such an instrumental asymmetry can be eliminated by measuring with oppositely magnetized samples and canceling out the instrumental asymmetry in case of magnetic materials as follows:

$$P_+ = \frac{1}{S_{eff}} \frac{I_{L,+} - A_{inst} I_{R,+}}{I_{L,+} + A_{inst} I_{R,+}}$$
$$P_- = \frac{1}{S_{eff}} \frac{I_{L,-} - A_{inst} I_{R,-}}{I_{L,-} + A_{inst} I_{R,-}} \tag{2.23}$$

where $+(-)$ indicates magnetization direction of the magnetized sample. Considering the symmetry of the magnetization, it is clear that the $P_+ = -P_-$ and thus the Eq. (2.23) can be finally transformed into the independent

one from A_{inst} as follows:

$$P = \frac{1}{S_{eff}}\frac{X-1}{X+1}$$

$$X = \sqrt{\frac{I_{L,+}I_{R,-}}{I_{L,-}I_{R,+}}} \tag{2.24}$$

This technique is called "*cross asymmetry*" method [54]. However, one may notice that the technical analysis cannot be utilized for the nonmagnetic samples. Thus, in the SARPES measurement using Mott detector, there is a possibility that the artificial asymmetry can be always superimposed on the intrinsic asymmetry from the real spin-polarization. This is a serious weak point of Mott detector as a spin detector. In order to subtract the factor of the instrumental asymmetry, the non-spin polarized state such as contaminated materials is measured and A_{inst} obtained with the result is utilized for given samples.

As listed in Table 2.1, the typical S_{eff} and I/I_0 of the electrons by the target in Mott detectors are in the range of 0.1-0.2 and on the order of 10^{-2}, respectively. Thus, the FOM becomes on the order of 10^{-4} [41, 42, 43, 44], which indicate that 10^4 times longer acquisition time would be required to obtain a spectrum with the same S/N ratio than for the conventional spin-integrated photoemission measurements.

This extremely low efficiency of the SARPES measurement using the Mott detector degrades the performance of SARPES measurement with high energy and/or angular resolutions; the typical resolutions are 100 meV in energy and 1° in angle even with high flux photons. However, Mott type spin detector is used as standard spin detector because of their stability in operation even though high-voltage treatment is difficult. Besides, the scattering angle and energy dependent S_{eff} in Mott scattering for several kinds of atomic core has been calculated [51]. Thus, one can directly expect the experimentally observed asymmetry and calculated the Sherman function in advance, which helps us to calibrate S_{eff} the Mott detector. This capability of self-calibration of the S_{eff}, which is very important for determining the value of spin polarization of the electron precisely. Furthermore, it is noteworthy that one can resolve the multi-spin-components at once if another pair of electron channels are orthogonally set to another pair of detectors.

2.2.3   VLEED type spin polarimetry
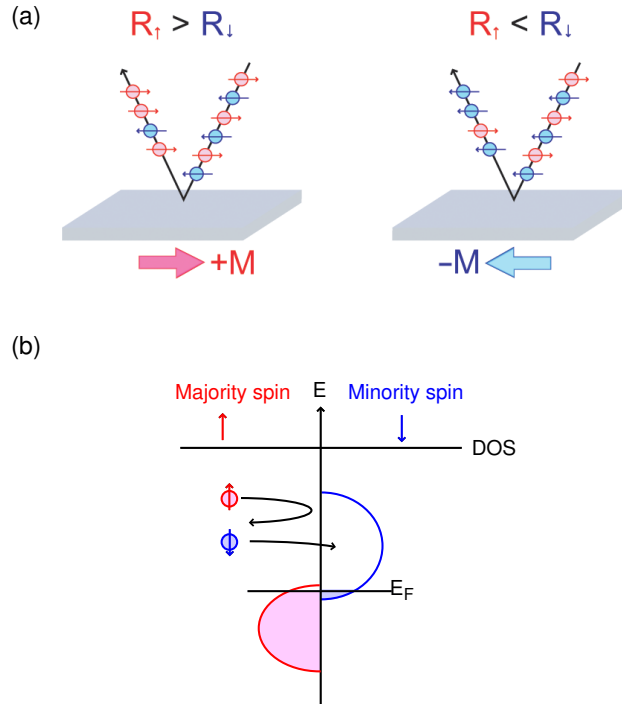
Figure 2.9: (a) Schematic illustrations of spin-dependent reflection of ferromagnetic surface. (b) Image of spin-dependent reflection together with spin asymmetric density of state.

As mentioned above, one needs to sacrifice energy and angular resolutions with Mott type spin detector to obtain high intensity of incident electrons and thus it makes it more difficult to resolve very steep energy dispersion such as topological surface state. In order to overcome this problem, a high efficient spin detector is strongly required. As listed in Table. 2.1, very low energy electron diffraction (VLEED) type electron spin detector possesses a large FOM. The VLEED detector is based on the spin-dependent electron reflectivity of very low energy electrons, which originates from the spin-exchange interaction of the ferromagnetic target as shown Fig. 2.9(a). Owing to higher scattering probability of the low energy electrons (E_k ~6-10 eV) compared to the high energy electrons (E_k ~20-100 keV) for the Mott scattering and relatively higher S_{eff}, VLEED type spin detector presents ~100 times higher FOM than that for Mott type conventional spin detector. Thus, VLEED de-

tector can be considered as a key to the realization of high efficient SARPES system.

As shown in Fig. 2.9(b), the probability of electron absorption and reflection is proportional to the density of states of materials. In the ferromagnetic materials, the density of states in the unoccupied state is not identical between majority and minority spin states because of the spin-exchange splitting in the energy bands. Therefore, the probabilities of electron absorption and reflection should be different between the cases of parallel and anti-parallel spin electron injection with respect to the magnetization direction and thus one can determine the spin polarization of incident electrons if the intensity of absorbed or reflected electrons by a magnetized target is measured. This is a principle of spin detection with VLEED detector. In the actual VLEED spin detector, we measure the intensities of reflected electrons by plus and minus magnetized ferromagnetic targets (I_{+M_α} and I_{-M_α}), and obtain the asymmetry between two as follows:

$$P_\alpha = \frac{1}{S_{eff}} \frac{I_{+M_\alpha} - I_{-M_\alpha}}{I_{+M_\alpha} + I_{-M_\alpha}} \tag{2.25}$$

where α is quantized axis of magnetized target.

Despite VLEED detector possesses high FOM, Mott type detector is more conventional spin detector because there is a issue in the magnetic target of VLEED detector. In contrast to high-energy electrons utilized in Mott scattering, reflection of low-energy electrons with the magnetic target are very surface-sensitive. Therefore, the VLEED detector cannot keep a high performance for long-time scan owing to the oxidation of the Fe film by the residual gas. This complexity of target preparation and the quick deterioration of the Fe film prevents the use of the detector in spite of its high efficiency.

In 1998, *R. Bertacco* and *F. Cicacci* proposed that the pre-oxidization of a Fe(001) film with pure oxygen, Fe(001)-$p(1\times1)$-O system, which can prevent the film from further oxidation [55]. The pre-oxidization increases the lifetime of the film markedly from a few hours to a few days and keeps the high performance. Furthermore, even after a slight degradation of the film, the spin resolving power and the reflectivity can be recovered with just short annealing at about 600 C∘ for 1 min. Owing to these great properties of the method, several groups have recently developed new SARPES machines equipped with VLEED spin detectors.

Chapter 3

Experimental Systems

3.1 BL-9B: spin-ARPES end-station (ESPRESSO machine)

3.1.1 Overview
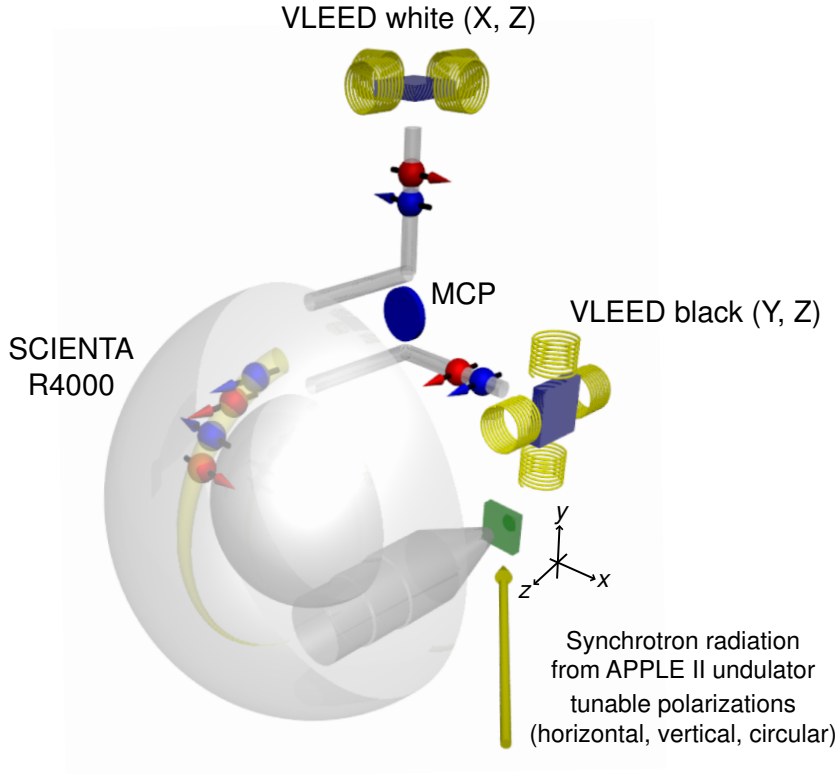
Figure 3.1: Schematic image of high efficient SARPES system at HiSOR, ESPRESSO machine.

A high efficient SARPES system named ESPRESSO (Efficient SPin REsolved SpectroScopy Observation) machine has been developed at the multi-polarization undulator (quasi-periodic APPLE-II) beamline, BL-9B, of Hiroshima Synchrotron Radiation Center (HiSOR) [56]. The schematic image of ESPRESSO machine is shown in Fig. 3.1. In this system, the two-independent VLEED type spin detectors, named "*white*" and "*black*", are equipped with the multi-channel spectrometer SCIENTA R4000 through 90 ° electron deflectors and set to the different directions. Magnetic targets in

66

each detector can be magnetized in-plane directions for the targets by the two pairs of electric coils installed orthogonally beside the targets. Thus, not only in-plane spin components but also the perpendicular to the sample surface can be measured and finally one can three-dimensionally determine the spin-electronic structure with ESPRESSO machine. Technically, the combination with the multi-channel spectrometer makes it possible not only to perform three dimensional (3D) SARPES but also spontaneous ARPES-SARPES parallel measurement, which can greatly provide us with an ability to determine k-position accurately for SARPES measurement. Technical information about the ARPES-SARPES parallel measurement with ESPRESSO machine will be mentioned in Sec. 3.1.2. The instrumental description of VLEED detector will be introduced in Sec. 3.1.5.

Beside, it is a noteworthy advantage of ESPRESSO machine that the quasi periodic APPLE-II undulator is utilized as an incident photon source in the beamline. This type of undulator can provide us with a high flux and high monochromatic light as well as tunable light polarizations (horizontal, vertical and circular). A use of the high flux and monochromatic light can further raise the efficiency of SARPES measurement and thus both energy and angular resolutions can be extremely improved. Moreover, using the variability of light polarization, one can focus on the precise spin electronic structure through the light polarization dependences. The further description about APPLE-II undulator is mentioned in Sec. 3.1.6.
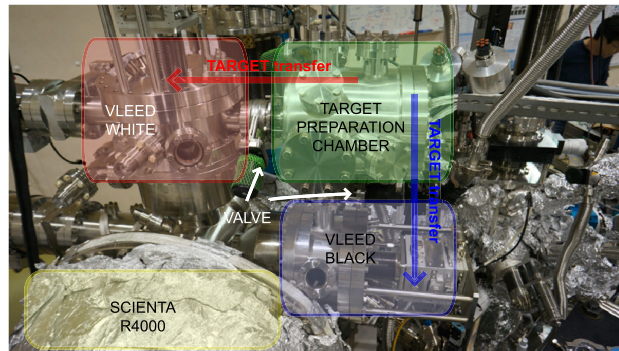
Figure 3.2: A view around the detection systems of ESPRESSO machine, which include SCIENTA R4000 spectrometer, VLEED white and black detectors, VLEED prep chamber.

Figure 3.2 shows a view around the detection systems of ESPRESSO machine. A target preparation chamber is directly connected to the both of

VLEED detectors, which is isolated from them with vacuum valves (ICF70). Before the SARPES measurement high quality targets are prepared under the ultra high vacuum chamber and smoothly transfered into the VLEED detectors without vacuum breaking. Details of the target preparation are introduced in Sec. 3.1.3.

3.1.2 Two-hole type ARPES-SARPES parallel measurement
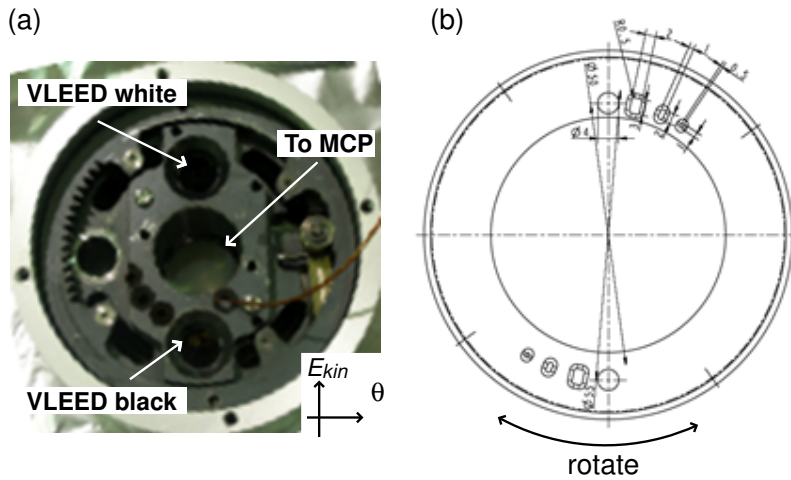
Figure 3.3: (a) Two-hole type spin detection system in which a large hole located at the center is a way to the multi-channel ARPES detection and the next small two holes are paths to VLEED white and black spin detectors. (b) A schematic of the aperture for SARPES measurement. For each VLEED channel, four types of aperture sizes are available, which can be selected with manual rotation from the out-side of the vacuum chamber.

In order to perform ARPES-SARPES parallel measurement, two-hole type spin detection is employed. Promptly behind the hemispherical analyzer, paths of photoelectrons screened out to the spin-integrate and spin-resolved detections with the shield as shown in Fig. 3.3(a), where a large hole is located at the center with surrounded and small holes are arranged next to the large one. Energy and angular axises of the shield are also shown in Fig. 3.3(a). Photoelectrons through the large hole are detected with MCP as a spin-integrated ARPES measurement and the E_{kin}-θ intensity map are

acquired at once. On the other hand, photoelectrons through the small holes located above and below the large one are transfered into the "*white*" and "*black*" VLEED spin detectors and finally counted with a single channeltron as a spin resolved measurement. The all holes in the shield are arranged in the E axis so that the ARPES-SARPES parallel measurement can be performed with sweeping the measured E_{kin} .

	Aperture			
Lens mode	$\phi4$	2×3	1×2	0.5×1
Angular 30	±3	±1.5	±0.75	±0.38
Angular 14	±1.4	±0.70	±0.35	±0.18
Angular 7	±0.70	±0.35	±0.18	±0.09

Table 3.1: Angular resolutions of SARPES measurement as a function of the electron acceptance angles in different analyzer lends modes with different aperture sizes.

	Aperture			
Slit (mm)	$\phi4$	2×3	1×2	0.5×1
0.2	18.4	14.0	9.3	4.9
0.5	18.6	14.2	9.5	5.4
1.5	19.9	15.9	11.9	8.9
4	27.2	24.4	22.0	20.6

Table 3.2: Calculated energy resolutions of SARPES measurement as a function of the aperture and the entrance slit sizes at the analyzer pass energy of E_p=2 eV. Expected energy resolutions are generally proportional to the E_p.

The size of MCP in ESPRESSO machine is 25 mm in diameter and actually smaller than the original one for conventional VG-SCIENTA R4000 analyzer in which the diameter of the MCP is 40 mm. However, the acceptance angle of ARPES image is still kept to be ±15 ° by the wide acceptance angle lens of the modified analyzer. The acceptance angle can be changed by using different lens modes to ±7.0 and ±3.5 for the high-angular resolution measurement. After thorough the small holes for the spin detections, the

photoelectrons are further selected with small aperture. Four types of aperture sizes are available in the machine as shown in Fig. 3.3(b) and they can be manually selected from the out-side of the vacuum chamber. Therefore, one can select the optimum experimental set-up for the SARPES measurement. As can be expected from the geometry of the two-holes in Fig. 3.3(a), the angular resolution for the spin detection is proportional to the transverse size of apertures and the energy resolution for the spin detection depends on the longitudinal aperture size as well as the entrance slit size of the analyzer. Several experimentally estimated angular and energy resolutions are summarized in Table. 3.1 and Table. 3.2, respectively.

Figure 3.4 shows an example of performance ARPES and SARPES measurement on Bi(111) film grown on Si(111) surface. With the six-axis goniometer (x, y, z, polar, tilt, azimuth), one can perform the volume mapping of ARPES measurement includes, E-k_x and E-k_y energy dispersions as well as constant energy contours (k_x-k_y maps) as shown in Fig. 3.4(a). For SARPES measurement, one always has to take account into k position especially in very steep energy dispersion such as topological surface states and also Rashba spin split bands. In ESPRESSO machine, one can get the k position accurately from the volume mapping obtained by the multichannel ARPES measurement and thus determine the precise k dependent spin textures. Figure 3.4(b) represents the result of the parallel measurement that the ARPES mapping are acquired with MCP with large acceptance angle (top panel) and at the same time the spin-resolved EDCs with both VLEED detectors are obtained (bottom panel) where the red (blue) line shows the EDCs obtained at $+$ $(-)$ magnetization of the targets. The back line in the top panel shows the EDC integrated withing the green color rectangle that indicates the angular resolution of SARPES measurement as listed in Table 3.1. It is clear that the integrated EDC is equally to the spin-resolved EDCs. To compare the ARPES measurement, the energy and angular resolutions in SARPES are poor so that it can sometimes mask specific energy dispersions. However, using combination of SARPES with ARPES using the multichannel spectrometer, one can follow the details of the complicated energy dispersions and thus precisely identify the spin structure with ARPES-SARPES parallel measurement.

(a) **ARPES with multichannel detector**

(b) **Spin-ARPES with two VLEED detectors**
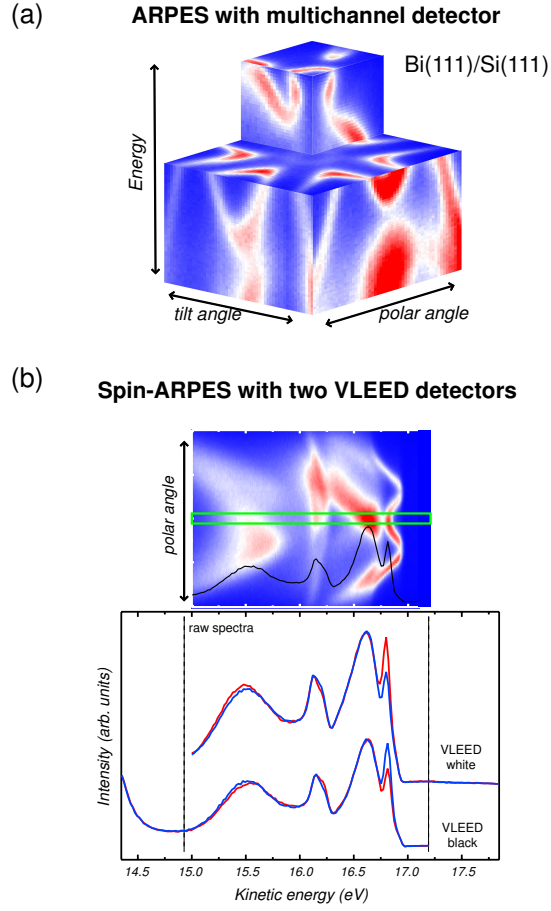
Figure 3.4: (a) Volume image of two-dimensional energy dispersion (E_{kin}-$\theta(k_x)$-$\phi(k_y)$) of Bi film on Si(111). (b) ARPES (top panel) and SARPES (bottom panel) in the parallel measurement with two-hole system. In top panel, green rectangle indicates the measurement angle position for SARPES spectra. Black line represents the integral energy distribution curve from ARPES map within the angular resolution for SARPES, which is shown by the width of the green rectangle.

3.1.3   Instrumental set-up of VLEED spin detector

Our instrumental set-up of VLEED detector is shown in Figure 3.1.3(a) and (b) that show the detection system with a shield covering the components around the ferromagnetic target stage and the detection system without a shield, respectively. The detection components consist of a target stage, four coils, their covers, and two channeltrons.

71
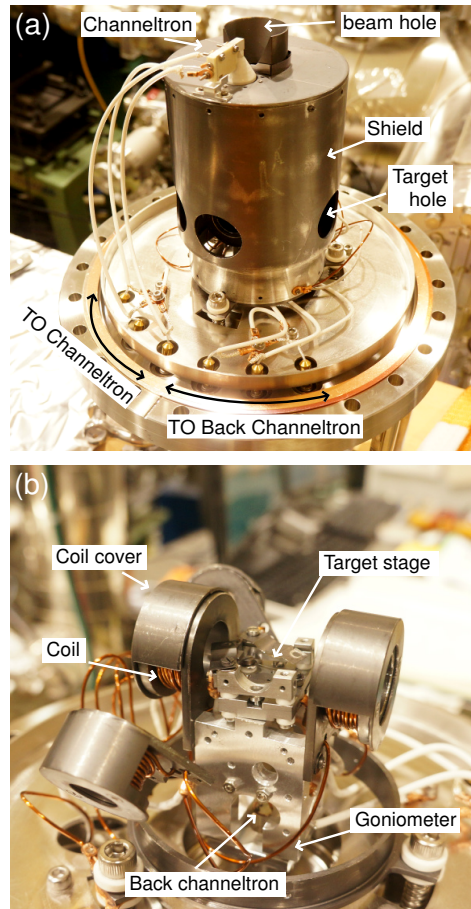
Figure 3.5: (a) Completed VLEED detector where the target stage is covered with the shield. (b) Detection components around the target stage.

Two coils are arranged face-to-face with each other beside target stage and the other pair is put orthogonally to the pair. The surface of the coil wire is covered with kapton to hold a insulation between the contacts and therefore the coil assemblages need to be covered with metallic components to prevent them from charging up during the measurement. The screw direction of a coil pair must be equivalent; otherwise the magnetic fields from the each coil will cancel out at the target position. The electrical current in coil pairs, that is, the magnetic field is switched by bipolar condenser bank that can be remotely controlled (Tsuji Co.).

A one of channeltron is inserted behind the target stage. If target is removed from the stage, the back channeltron can be available and count the incident electron. This set-up is very useful to count the total incident electrons, which is necessary to determine the FOM of the detector, and it is also available to evaluate the spot size of the incident electron beam.

These components are mounted on the goniometer that is controllable in angles and x-y positions with two swivels and x-y stage (Kohzu Precision Co.), and are covered with the shield. The other channeltron is set on the shield, which is utilized to count electrons reflected from the target for the spin detection. The angle between the surface normal of the target and the channeltron is designed to be 7 °. So, the target stage must be tiled as to make the surface normal point to the channeltron with the goniometers before starting measurement.

3.1.4 Performance of ESPRESSO machine
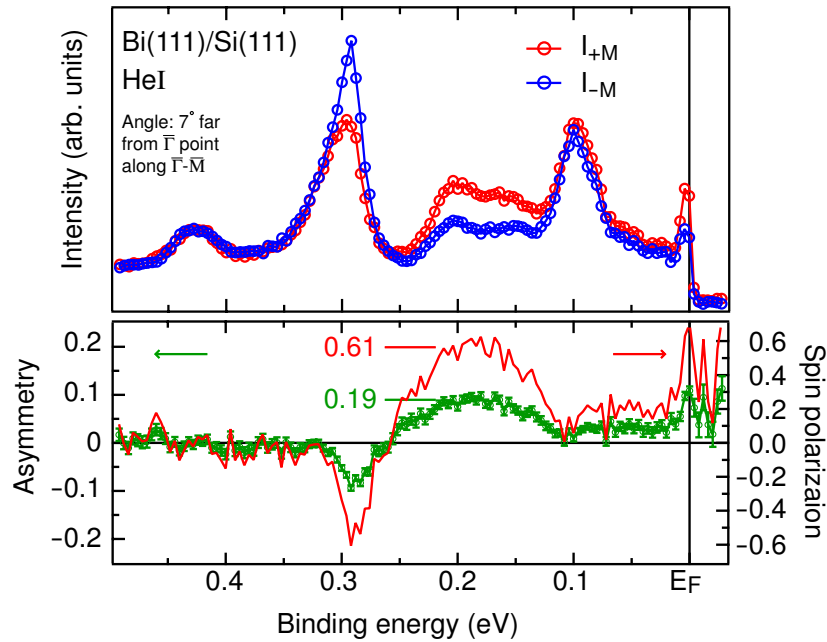
Figure 3.6: (a) Obtained spectra of Bi film with the positive (red) and negative (blue) magnetized target. (b) Asymmetry obtained from (a) (green) and the spin polarization with S_{eff}=0.31 (red).

73

E_k	S_{eff}	I_0/I	FOM
5.8 eV	$\sim$0.31	0.1	3.1×10^{-2}

Table 3.3: Summarized the performance parameters of SARPES measurement in ESPRESSO machine.

As mentioned in Sec. 2.2.3, it is a problem that there is no well-established procedure of self-calibrating a spin-resolution power, the so-called S_{eff}, for the VLEED spin detector, which is in contrast to a conventional Mott spin detector. To determine the S_{eff} of magnetic target in our VLEED instruments, a Bi(111) film on a Si(111) clean surface is employed as a standard sample. Firstly, the spin polarization of Bi(111) film is determined using an another SARPES system equipped with a compact type Mott detector in Hiroshima university whose S_{eff} was correctly calibrated with secondary electrons in Ni(110). Since the observed asymmetry can be affected by energy and angular resolutions as well as experimental geometry, we compare the data taken with the same experimental geometry in a similar resolution setting at a specific k-point. Figure 3.6(a) represents the obtained spectra with the $+$ (red) and $-$ (blue) magnetized target obtained at ESPRESSO machine. The measurement performed with He non-monopolized discharge lamp at 7° far from the surface normal along $\bar{\Gamma}$-$\bar{M}$ line. Asymmetry obtained from the spectra is shown with green line in Fig. 3.6(b). Then, the spin polarization from the Asymmetry is compared to that with Mott detector (not shown). In particular, S_{eff} is fitted to be the value that make the large asymmetry 0.19 ($E_B=\sim$0.2 eV) be 0.61 spin polarization which has been evaluated by Mott detector. Following the procedure, the S_{eff} is determined to be $\sim$0.31. In our system, the values of the S_{eff} are usually higher than 0.25, the highest being 0.42. The reflectivity of the electron by a target can be estimated by measuring the incoming and reflected electron intensities at the target position using both of channeltrons that are behind the target stage and beside the exit of the transfer lens. Although the reflectivity depends on the target, it is usually about 10 % higher than that for Mott type spin detector. Thus, the total efficiency (FOM) is improved nearly one hundred with respect to that for the Mott detector. These parameters indicating the performance of spin detector are summarized in Table. 3.3. [56].

74

3.1.5 Target preparations
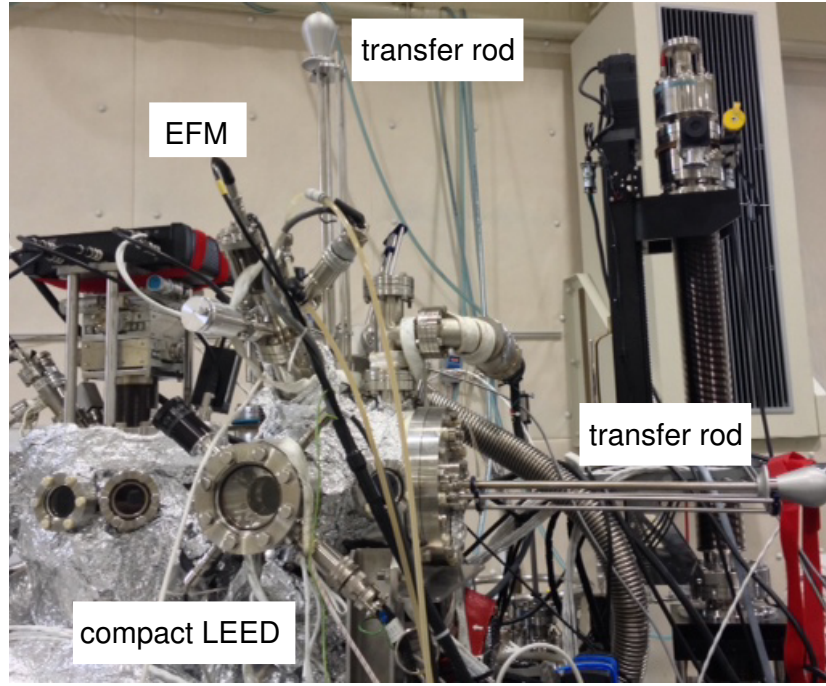
Figure 3.7: VLEED preparation chamber with transfer systems to VLEED black and white detectors.

A preparation of VLEED target is an important to SARPES experiment. In ESPRESSO machine, Fe(001) film on MgO is utilized as a VLEED magnetic target. To make growth of a high quality Fe film ultra-high vacuum, Fe evaporator and evaluation system are necessary and furthermore an *in-situ* transfer system to each spin detector are significant. Figure 3.7 shows an overview of the target preparation chamber between two spin detectors. The target preparation chamber is equipped with the OMICRON type EFM (Evaporation with Flux Monitor), the compact low energy electron diffraction (LEED) system, target annealing system in the vacuum chamber with target bank, O_2 gas line and transfer systems (Ferrovac Co.) to both VLEED white and black detectors. MgO (100) plate is prepared and polycrystalline Au is deposited on the part of MgO plate before mounted on a target holder because MgO is well know as an insulator. Then, the MgO plate is mounted on the target holder and installed into the target preparation chamber. In

the ultra-high vacuum chamber, the target preparation is advanced with the procedure as follows:

(1) Annealing MgO plate around 700 °C till the pressure is better than 2×10^{-7} Pa.

(2) Fe deposition on the MgO plate at room temperature with around 25 n A/s and total amount is 3×10^5n
    A.

(3) Post annealing with 600 °C for 20 min.

(4) O_2 exposition on the Fe(001) film with 5×10^{-5} L. ($1.4 times 10^{-5}$ Pa for 5 min)

(5) Flush annealing the Fe(001) at around 600 °C for just 1 min.

Figure 3.8(a)-(d) represents LEED patterns of the target during proceeding with the several processes. The LEED pattern of the target after post annealing following Fe deposition (Figure 3.8(c)) is similar diffraction pattern to that for MgO clean surface and thus the Fe atoms is well ordered on the MgO (100) surface. After O_2 exposure and further flush annealing, it will be cleared and sharper diffraction pattern. This feature is a signature that a monolayer O_2 molecule covers the Fe(001) surface and thus it is confirmed that the pre-oxidized Fe target is successfully prepared. Figure 3.8(e) and (f) shows a comparison between LEED patters of a clean and a contaminated target surfaces. As is clearly seen in Fig. 3.8(f), c($2 times 2$) superstructure is appeared if the target get some contamination. The superstructure is originated from carbon impurities in the Fe(001). As long as one can see the superstructure, the target cannot be expected to be a VLEED target and usually it is too hard to remove only the impurities. Obtained target usually shows S_{eff} ~0.3 and works as a VLEED target more than one week without any annealing under 1×10^{-8} Pa. After long scans or exposed by air at the order of 10^{-4} Pa, one can obtain the fresh target with a flush annealing around 600 °C for 1 min, without any deduction of S_{eff} at so many times.
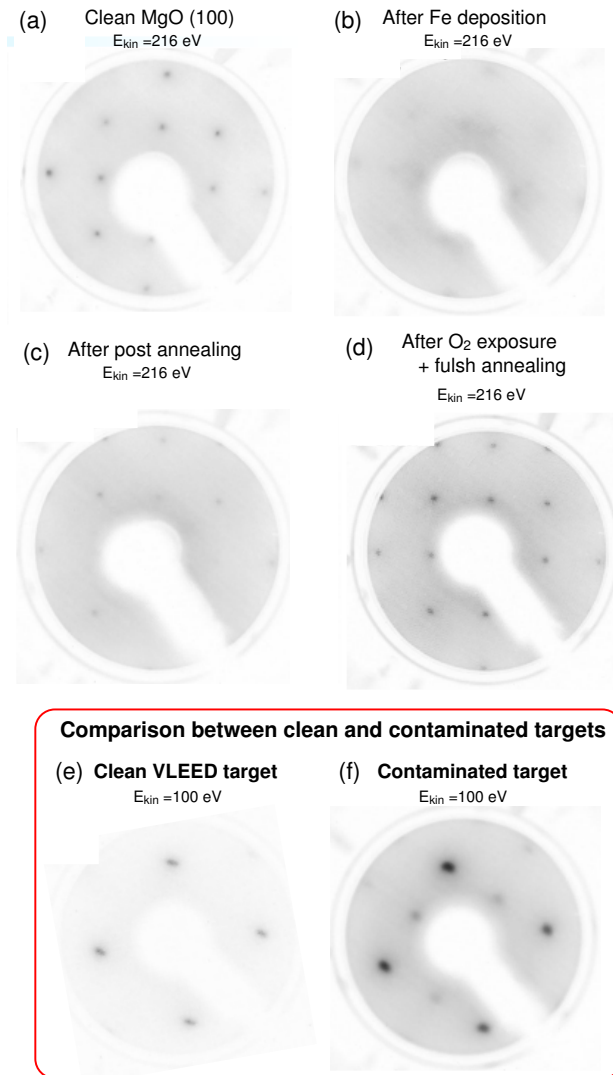
Figure 3.8: Low energy electron diffraction (LEED) patterns during the VLEED target preparation.

3.1.6 BL-9B: a branch of APPLE II undulator beamline

ESPRESSO machine is an end-station of BL-9B that is a beam line of the quasi-periodic APPLE-II undulator. The APPLE-II undulator installed is shown in Fig. 3.9(a). An undulator is an insertion device in a synchrotron

(a) (b)
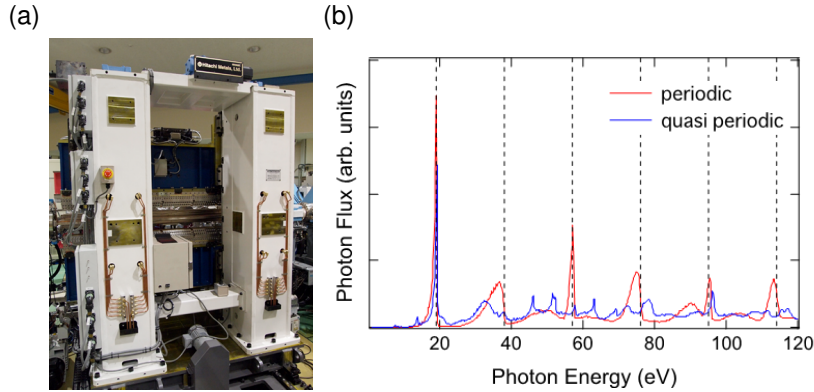
Figure 3.9: (a) Installed quasi-periodic APPLE-II undulator at HiSOR (b) Comparison of calculated spectra for periodic and quasi-periodic undulator.

storage ring and consists of periodic dipole magnets. Electrons going through the periodic magnet field are forced to be undulated resulting in the radiation. Due to the superposition of the light the radiation from an undulator is very intense and more monochromatic compared to that from the bending magnet. However, even in the undulator higher order lights can not be negligible and may interrupt PES measurement that photoelectron signals from the fundamental radiation will overlap with that emitted by the higher order light. The quasi-periodic type undulator is recently developed to suppress the higher order lights. Figure. 3.9 (b) shows calculated photon flux of the periodic undulator and quasi-periodic APPLE-II undulator. It is clear that the high order lights is suppressed for the APPLE-II undulator. Furthermore, the APPLE-II undulator provides with a variability of light polarization, horizontal, vertical and circular polarization by moving magnetic arrays. Therefore, not only the high efficient spin-ARPES measurement with high intense light source but also with variable light polarization is available at ESPRESSO machine.

The beamline is a Dragon-type grazing incidence monochromator beamline as shown in Fig. 3.10. The photon beam generated from the undulator is firstly focused in the horizontal direction by a spherical mirror (M0) and an next spherical mirror (M1) focused the beam in the vertical direction onto the entrance slit (S1). Behind the slit, a plane mirror (M2) reflect the the beam downwards to the spherical monochromator grating. The monopolized beam is then focused on the exit slit (S2). Finally, the toroidal mirror (Mf)
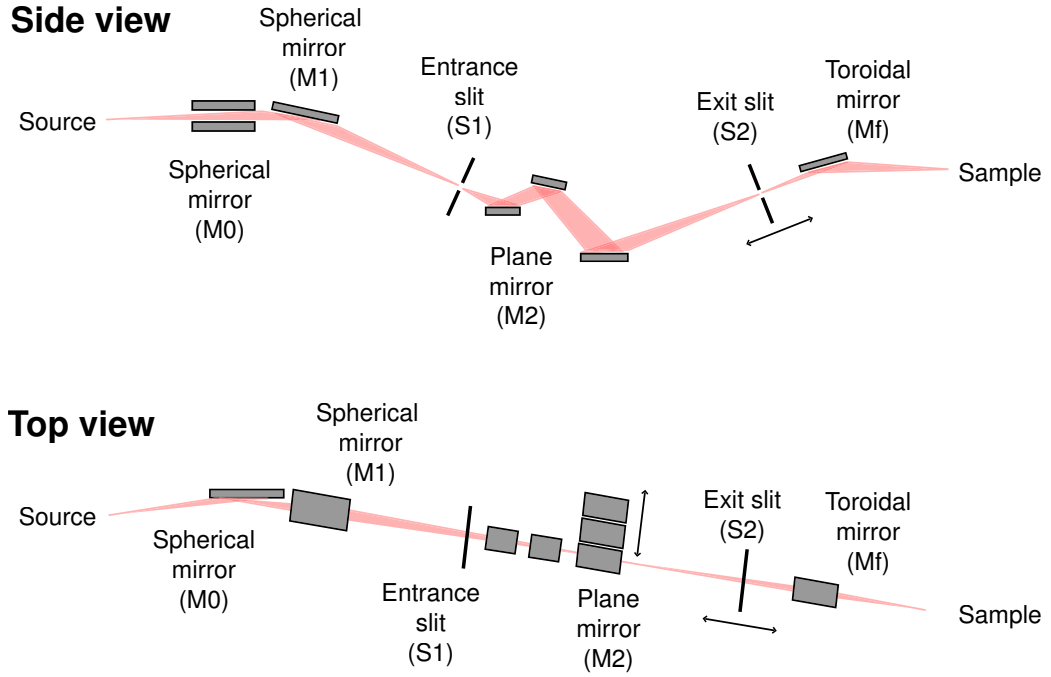
Figure 3.10: Schematic view of BL-9B of HiSOR.

then focuses the beam onto the sample position. The positions of the grating and S2 are accurately controlled by the stepping motor.

The beam line is equipped with three monochromator gratings (Gr1: 900 lines/mm, Gr2: 600 lines/mm, Gr3: 1200 lines/mm) to cover wide photon energy range in 15 to 300 eV. The resolution powers for the gratings are listed in Table. 3.4, which has been determined by measuring the absorption spectra of gaseous samples of Neon, Helium, Argon, and Krypton. The degree of circular polarization is $\sim$70 %.

Grating	$h\nu$	S1/S2	$E/\delta E$ (δE)
Gr1 (900 l/mm)	21 eV	10μm/10μm	14400 (1.6 meV)
Gr2 (600 l/mm)	48 eV	10μm/10μm	15000 (3.1 meV)
Gr3 (1200 l/mm)	244 eV	10μm/10μm	7800 (31.4 meV)

Table 3.4: Energy resolution power ($E/\delta E$) of the three gratings at BL-9B.

3.1.7 Details of analysis
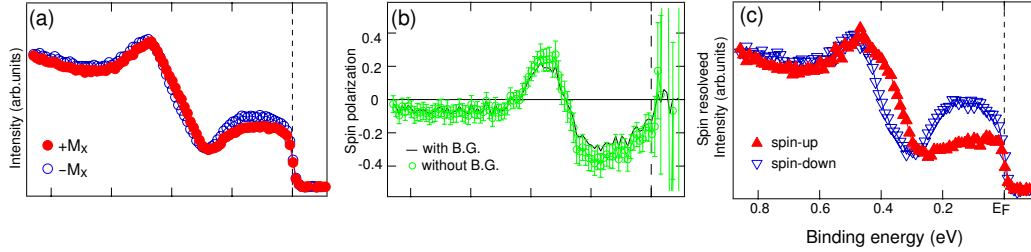
Figure 3.11: (a) Energy distribution curves (EDCs) measured with different magnetization directions that are parallel (red closed circles) and anti-parallel (blue open circles). (b) Spin polarizations as a function of binding energy obtained from the spin-resolved analysis. (c) Finally obtained EDCs for spin-up (red closed triangles) and spin-down (blue open triangles) channels.

Here, we show how to obtain the spin resolved spectra with the ESPRESSO machine. Without top-up electron injection into a storage ring at HiSOR, the photoelectron intensity superimposed on the extrinsic background is reduced with unavoidable decay of the electron current in the storage ring. This could be a problem because the photoelectrons need to be counted at least twice with opposite in-plane magnetization directions of the target to get the intensity asymmetry. In order to solve this problem, we have taken the SARPES spectra in a measurement cycle; $+\boldsymbol{M} \to -\boldsymbol{M} \to -\boldsymbol{M} \to +\boldsymbol{M}$ and the two spectra are finally averaged for each magnetization direction as shown in Fig. 3.11(a). To achieve sufficient statistics of the spectra, the same cycle several times is repeated and subsequently the obtained spin polarization spectra are averaged as shown in Fig. 3.11(b). Focusing on the intensity above E_F in Fig. 3.11(a), one will have the non-spin polarized background signal probably owing to the higher-order light from the monochromator. This unpolarized background may mask the spin polarization of photoelectron emitted by the first-order light, and should be removed before the spin analysis. In Fig. 3.11(b), the green open circle shows the spin polarization after the background subtraction, which is assumed to be constant. Comparing to the spin polarization without the background subtraction, one can see slightly larger spin polarizations. The resultant spin-resolved EDCs are shown in Fig. 3.11(c).

3.2   BL-9A: Low Energy ARPES
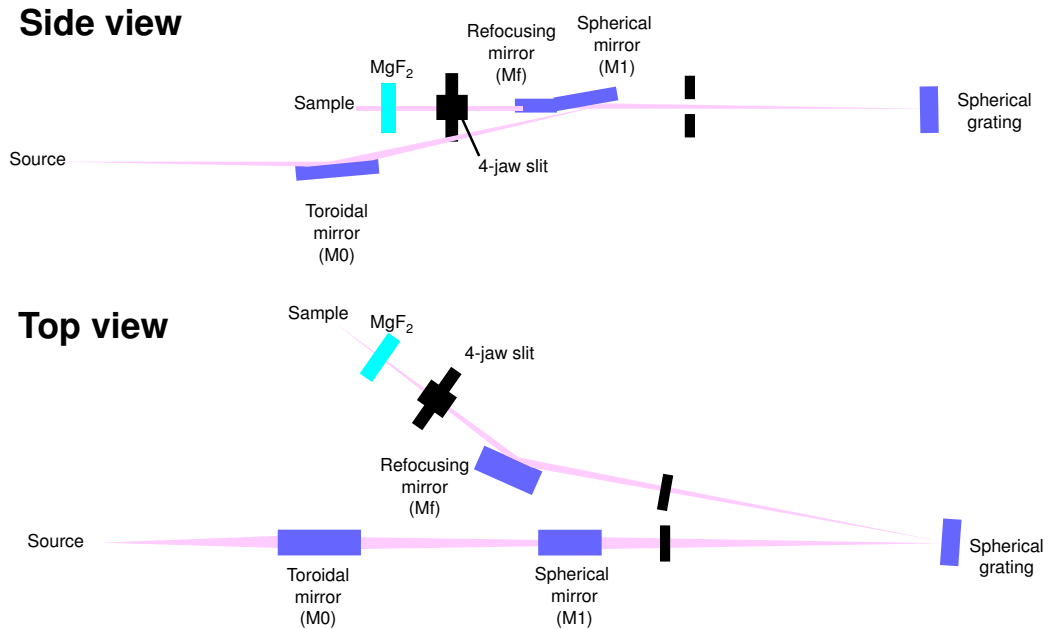
Figure 3.12: Schematic view of BL-9A of HiSOR.

BL-9A is a branch beam line for low energy high-resolution photoemission spectroscopy beamline equipped with a off-plane eagle mount normal incidence monochromator as shown in Fig. 3.12. Extracting M0 in BL-9B, one can switch the measurement for BL-9B to this beam line. The low photon energies, 4-40 eV, is available at this beam line. Furthermore, owing to the normal incidence mode for the monochromator the exit and entrance slits can be mounted at far from the spherical grating around ~3 m and thus the energy resolution is improved compared to that for the dragon type monochromator. MgF_2 window can be inserted behind the monochromator to cut the higher order light when the low photon energy below 10 eV is used.

A high resolution angle-resolved photoemission spectroscopy system equipped with the hemispherical electron-energy analyzer R-4000 (GAMMADATA-SCIENTA) was installed at the end of the beam line. with its excellent resolving power. The liquid-He-flow-type 5-axis goniometer (x, y, z, *polar*, *tilt*) was installed for constant energy contours mapping which are shown in

the Fig.3.3 (b). Azimuthal angle also can be manually controlled between $\pm 20\,°$.

3.3   BL-1: High-resolution ARPES end-station with Linear Undulator

BL-1 is the beamline which provides with ultraviolet linearly polarized undulator radiation. The monochromator set-up in BL-1 consists of dragon type grazing incidence monochromator (see Fig. 3.10). There are three interchangeable gold coated spherical gratings (G1, G2 and G3) in the monochromator to cover the photon energy from 20 to 300 eV. Two plane mirrors can be inserted between S1 and the grating to reduce the included angle. These are set for total resolving power > 7000 for the wide $h\nu$ ranges. A high
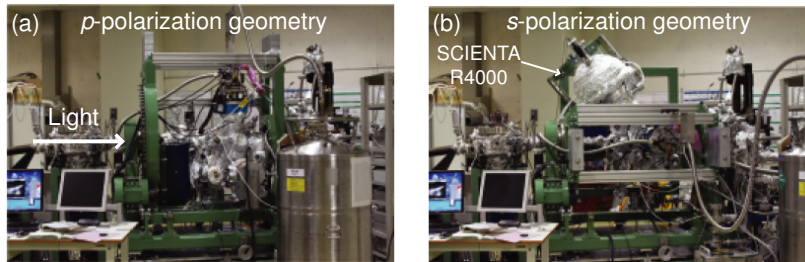
Figure 3.13: (a) *p*- and (b) *s*-polarization geometries at BL-1.

resolution angle-resolved photoemission spectroscopy system was installed on the the beam line. The hemispherical electron-energy analyzer R-4000 (GAMMADATA-SCIENTA) with its excellent resolving power. The liquid-He-flow-type 6-axis goniometer (x, y, z, *polar*, *tilt*, *azi*) was installed for constant energy contours mapping. Moreover, the greatest feature of this system is realizing the observation of *s*-and *p*-light polarization dependence on ARPES measurement by rotating the whole measurement chamber as shown in Fig. 3.13. The measurement chamber can rotate by 90 $°$ without braking ultra high-vacuum.

3.4 BL-7: ARPES end-station with the bending magnet section of the HiSOR ring

BL-7 is a ARPES beamline, which covers wide $h\nu$ range, 20-300 eV, from the synchrotron radiation at bending magnet section of the SOR ring. The dragon type grazing incidence monochromator is adopted in this beamline. The measurement chamber is equipped with the hemispherical electron-energy analyzer (SCIENTA SES 2002) and with the liquid-He-flow-type 5-axis goniometer (x, y, z, *polar*, *tilt*). Typical resolution power ($E/\delta E$) including the monochromator and the electron spectator is 1000.

Chapter 4

Electronic and magnetic structures in Bi$_2$Se$_3$ doped with magnetic and non-magnetic elements

4.1 Introduction

In this chapter, we study electronic and magnetic structures of the prototypical topological insulator Bi_2Se_3 with non-magnetic and magnetic impurities. As mentioned in Sec. 1.3, binary chalcogenides such as Bi_2Se_3 and Bi_2Te_3 have known as prototypical topological insulators (TIs) since a single topological surface state (TSS) is realized on the surfaces of these materials [21, 22, 23]. These binary chalcogenides form a tetradymite crystal structure with a stacking of quintuple layers (QLs) (X-Bi-X-Bi-X atomic layers, X: Se or Te) weakly coupled via van-der-Waals forces as shown in Fig. 1.13(a). Especially, Bi_2Se_3 has a large bulk energy gap (300-350 meV) which exceed room-temperature energy scale (30 meV), and furthermore the TSS shows the Dirac cone like energy dispersion [22]. Accordingly, the novel surface of Bi_2Se_3 has been expected to be a suitable ground for realizing high-temperature spintronic devices as well as studying the new intriguing phenomena under the time-reversal symmetry breaking. In the Sec. 4.2, we firstly focus on the precise electronic structure of the non-trivial surface state in Bi_2Se_3 with angle-resolved spectroscopy (ARPES). We further investigate the magnetic structure in Mn doped Bi_2Se_3 by means of ARPES and magnetic circular dichroism in Sec. 4.3.

4.2 Hexagonally deformed topological surface state and bulk carrier tuning in Bi_2Se_3

4.2.1 Introduction

In the previous ARPES results for the family (see Fig. 1.17), heavily warped Fermi surface (FS) has been observed in Bi_2Te_3, which indicates that the warping term in the effective Hamiltonian of the TSS as introduced in Sec. 1.25 is large in Bi_2Te_3. Due to the large warping term, the electron spin orientation acquires a surface perpendicular along $\overline{\Gamma} - \overline{K}$ symmetry line and new scattering channels can be turned on in Bi_2Te_3 [24, 25]. Actually, this surface electron scattering effect has already been confirmed in this compounds [28]. For the TSS of Bi_2Se_3, it has been believed that it has nearly ideal Dirac cone although the FS of Bi_2Se_3 seems not clear (see Fig. 1.17) [22]. For a circular FS, the electron cannot be back-scattered in the presence of the time-reversal symmetry. Accordingly, the ideal topological insulator has a perfect

linear dispersion and its shape of FS is a circle, where the back-scattering is strongly suppressed. Up to now, the warping effect has been observed only for case of Bi_2Te_3.

In order to precisely determine the shape of FS in Bi_2Se_3 and confirm whether it has the warping effect, we have observed its TSS with high-resolution ARPES measurement using synchrotron radiation and finally found that the FS of naturally electron-doped Bi_2Se_3 is hexagonally deformed, while the constant energy contour is circular-shaped near the Dirac point. We also demonstrated that the Fermi energy can be effectively tuned by doping the sample with Mg.

4.2.2 Experimental Set-up

The single crystallines of Bi_2Se_3 were grown by a standard procedure using the Bridgman method. Stoichiometric mixtures of Bi (5N: shots, Mitsuwa), Se (5N: shots, Mitsuwa) were melted in evacuated quartz ampules at 800 °C and below 5×10^{-7} Torr for a day and then slowly cooling at the speed of 1.5 °C/h to 550 °C for about three days. Then, the temperature was kept for a day to soft annealing the sample and gradually cooling down to the room temperature. Here, we summarize the procedure to make a single crystal of the Bi_2Se_3 as follow.

(1) Cleaning high-purity elements with nitric acid (1N) and acetone for 5 minutes, respectively.

(2) Enclosing these elements in the evacuated quartz ampules below 5×10^{-7} Torr.

(3) Heating ampules in Bridgman furnace and gradually cooling under the temperature program as described in Fig. 4.1.

The resultant crystals are cleaved along the basal plane (111) with a shining mirror like surface as shown in Fig.4.2(a) and the typical size is about 2 cm^3. The crystal structure of the Bi_2Se_3 was confirmed by Laue pattern, X-ray powder diffraction pattern and these results are shown in Fig.4.2(b) and (c). In Fig.4.2, we find that single crystalline sample is successfully obtained because very sharp diffraction spots were clearly observed. In Fig.4.2(c), we fitted the experimental data (red color line) to calculated one (blue color line) and these peak position are corresponding to each other. Angle-resolved
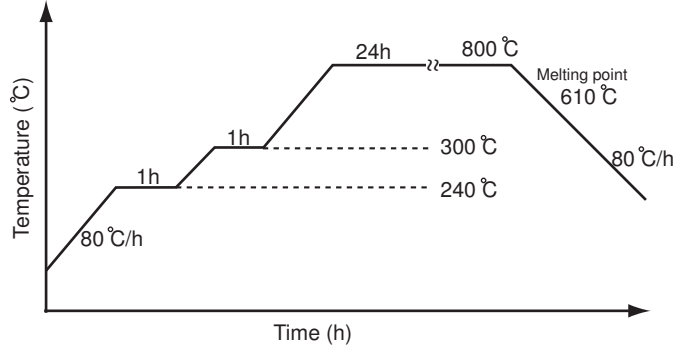
Figure 4.1: Temperature control sequence of Bridgman furnace for the fabrication of a single crystal of the Bi_2Se_3.
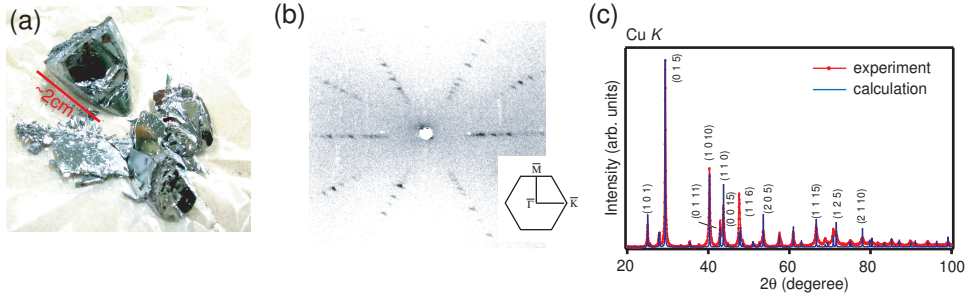
Figure 4.2: (a) Photo of the cleaved Bi_2Se_3 surface. (b) Laue diffraction pattern of (111) plane. (c) X-ray powder diffraction pattern.

photoemission spectroscopy was performed with the photon energy of 31 eV at the linear undulator beam line (BL1) of Hiroshima Synchrotron Radiation Center. The photoemission spectra were acquired with a hemispherical photoelectron analyzer (VG-SCIENTA R4000) at $\sim$10 K, by using linearly polarized light p- and s-polarized light . The constant energy contours were obtained by changing the azimuthal angle. The overall energy and angular resolutions were set at 15 meV and $\pm 0.1°$, respectively. The clean surface was obtained under the ultra-high vacuum below 1×10^{-8} Pa and at $\sim$10 K.

4.2.3 Results and Discussion

Fig.4.3 (a) shows the energy band dispersion acquired by ARPES measurement along $\overline{\Gamma}$-$\overline{M}$ line with photon energy of 31 eV with $p-$polarized light
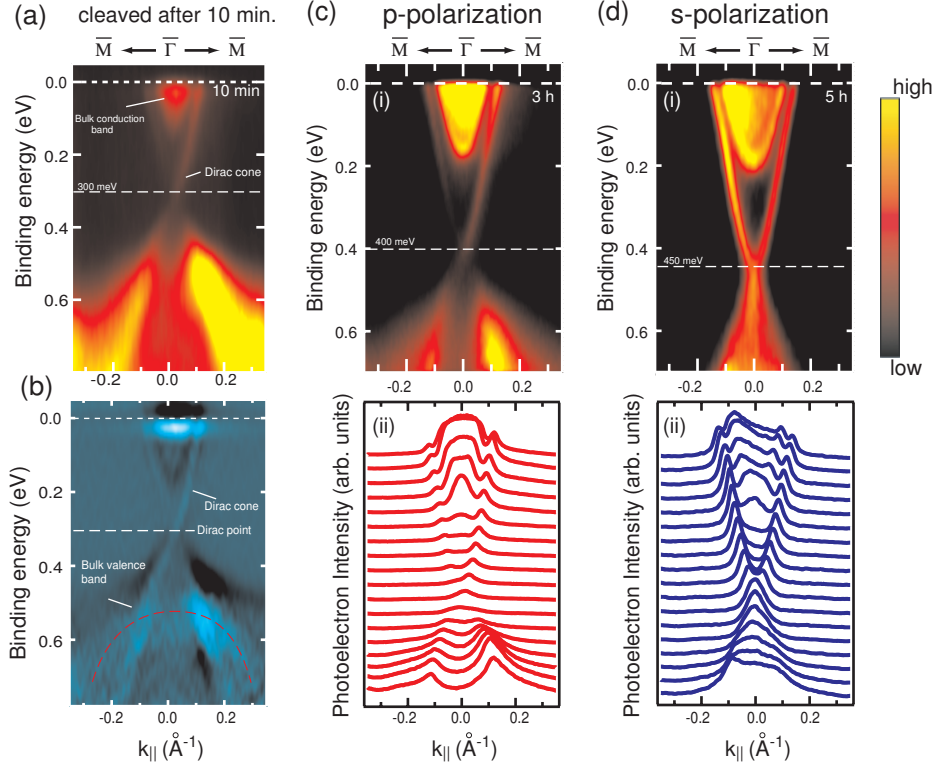
Figure 4.3: (a) The energy band dispersion acquired by ARPES 10 minutes after the sample is cleavage. (b) $k_\parallel$ dispersion and (ii) momentum distribution curves with photon energy of 31 eV with (a) p- and (b) s-polarized light along $\overline{\Gamma} - \overline{M}$ line. (c), (d) the ARPES energy dispersion measured in 3 hours and 5 hours after the cleavage, respectively.

10 minutes after the cleavage and its corresponding second energy derivative intensity plot is shown in (b). We find that the the surface bands cross E_F and these bands intersect at the Dirac point (DP) which is located at the binding energy (E_B) of 300 meV. Here, we also find that the bulk conduction band (BCB) is enclosed inside upper Dirac cone and it crosses E_F which shows that the natural electron doping occurs also for this sample. These results are consistent with the previous reports [22]. In Fig.4.3(b), we find that the bulk valence band (BVB) is located below the DP and its maximum binding energy is around 520 meV. We should note that these energy band can move toward the higher E_B as time goes by after the cleavage of the sample due to the molecular absorption on the surface which works as a dopant [57].

Fig. 4.3(c) shows the ARPES result acquired of 3 hours after the cleavage (i) and its momentum distribution curves (MDCs) (ii). From this result, we see that DP is shifted to 400 meV, which corresponds to electron doping feature and the photoelectron intensity of TSS has asymmetric weight at the positive and negative $k_\parallel$, while the bulk intensities are symmetric. From the MDCs, we find that the bulk state intensity is much higher than that of surface state. Here, we should note that the photoelectron intensity from the bulk state can be suppressed by a tuning the incident light polarization, as a consequence, the surface intensity can be enhanced. Fig.4.3 (d) is the result with $s-$polarized light, which shows symmetric photoelectron intensity from TSS while the bulk intensity is asymmetric and the spectral weight of the bulk conduction band is suppressed. This result is in contrast to the one obtained with the $p-$polarized light. Since it has been acquired 5 hours after the cleavage, the DP shifted toward higher E_B to 450 meV and then, the shift has been saturated at this energy.
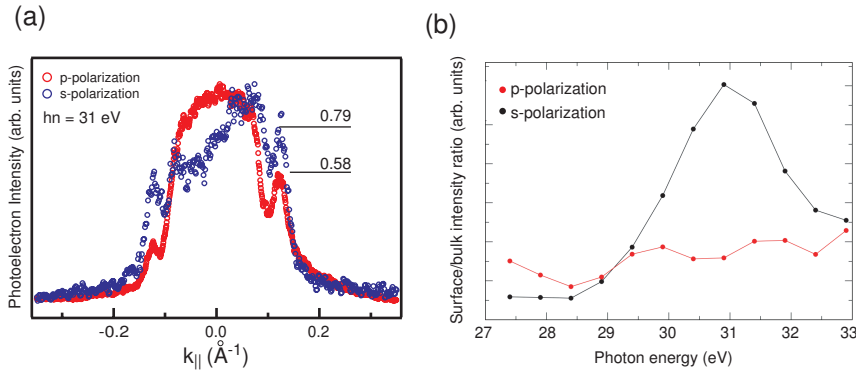
Figure 4.4: (a) The momentum distribution curves from Fig.4.3(a)-(ii) and (b)-(ii) at the binding energy for $k_\parallel = 0.12 \mathring{A}^{-1}$ of the surface state. (b) The calculated polarization and photon energy dependence of the photoelectron intensity from the surface state related to the bulk state versus the photon energy from 27 eV to 33 eV.

From the MDCs obtained for both polarizations, the photoelectron intensities are compared in Fig4.4(a). The red color and blue color circles correspond to the MDC at the binding energy when the $k_\parallel$ of the TSS is 0.12 $\mathring{A}^{-1}$ and these are normalized by the intensity maximum of the bulk state near the $\overline{\Gamma}$ point. The surface/bulk intensity ratios surface/bulk are $\sim$0.58 and 0.79 for the $p-$ and $s-$polarizations, respectively, which clearly

shows that the surface state is enhanced with the $s-$polarized light. Then, we show our calculation result to demonstrate photon energy dependence of the photoelectron intensity ratio as shown in Fig.4.4(b). It is clearly shown that the ratio is higher when using the $s-$polarized light in photon energy range from 30 to 32 eV and, more importantly, 31 eV is a critical photon energy where the ratio acquires the maximum value. These results imply that the experiment with $s-$polarized light is suitable for the high-resolution FS mapping of the TSS. Therefore, we have used the $s-$polarized light to precisely probe the TSS of Bi₂Se₃.
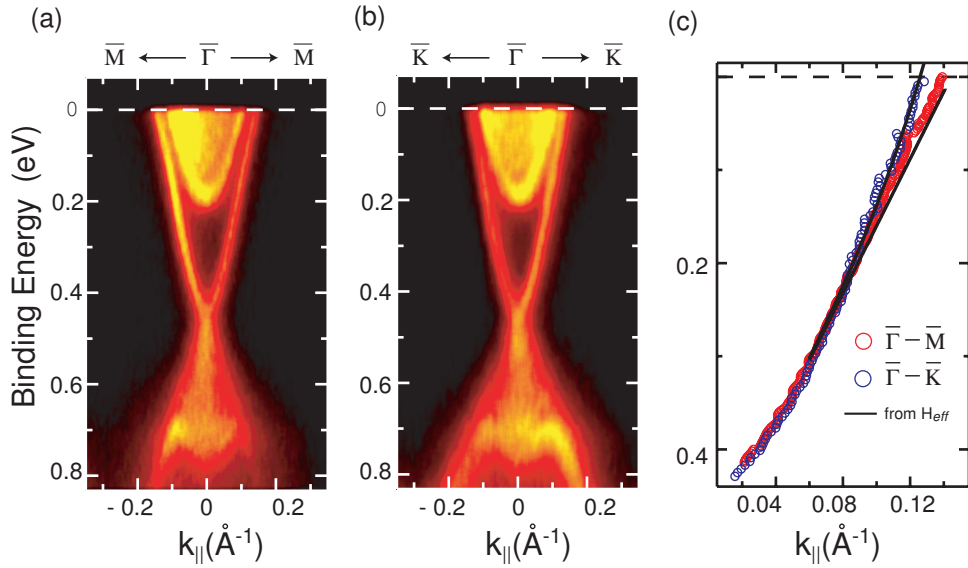
Figure 4.5: (a) The energy dispersion near the Fermi level along (a) $\overline{\Gamma} - \overline{M}$ and (b) $\overline{\Gamma} - \overline{K}$. (c) Intensity maximum of ARPES spectra along two high symmetry lines.The solid lines are a fit with the effective Hamiltonian. These figures are reproduced from reference [58].

Fig.4.5 (a) and (b) show the energy dispersion curves acquired by ARPES along two high symmetry lines, $\overline{\Gamma}$-$\overline{M}$ and $\overline{\Gamma}$-$\overline{K}$, respectively. The M-shaped valence band is also recognized below E_B=680 meV although this state is not clear with the $p-$ polarized light (see Fig. 4.3(c)), which indicates that the valence band can also be enhanced with the $s-$polarized light. Here, we should note that the energy dispersion along $\overline{\Gamma}$-$\overline{M}$ to is almost linear, while along $\overline{\Gamma}$-$\overline{K}$ it is warped toward the smaller k, which are clearly shown by the intensity maximum of ARPES result in Fig.4.5 (c). The magnitude of the

wave vectors at E_F (Fermi wave vector k_F) can be estimated to be 0.140 and 0.131 $\mathring{A}^{-1}$ along the $\overline{\Gamma}$-$\overline{M}$ and $\overline{\Gamma}$-$\overline{K}$ directions, respectively. The different k_F values correlate with the anisotropy of energy dispersions between these high-symmetry lines, which has not been revealed so far. The anisotropic energy dispersion can be described with the effective Hamiltonian,

$$H(\boldsymbol{k}) = \frac{k^2}{m^*} + v(k_x\sigma_y - k_y\sigma_x) + (\frac{\lambda}{2})(k_+^3 + k_-^3)\sigma_z \qquad (4.1)$$

where $k_{\pm} = k_x + k_y$ and v, λ and σ_z denote the Fermi velocity, warping parameter and z component of Pauli matrix, respectively [25]. We find that the experimental dispersions are reproduced well by the calculated one by using the effective Hamiltonian with the parameters v=3.55 eV·$\mathring{A}$ and λ=128 eV·$\mathring{A}^3$ as shown in Fig.4.5.

According to energy dispersion shown in Fig.4.5, the FS should also be anisotropies. Fig.4.6 (a) summarizes two-dimensional slices in k space at several energies from the DP to E_F of Bi$_2$Se$_3$. The whole results have been acquired within two hours in oder to avoid an energy shift, For the present FS mapping, we used a different sample with a lower defect concentration, resulting in shallower DP (350 meV from E_F) than that in Fig.4.5. At 100 meV, a circular-shaped constant energy contour is clearly identified. In going from the Dirac point toward E_F, the shape of constant energy contour evolves from a circle to a hexagon above 200 meV with increasing FS area. It is noticed that the shape of the constant energy contour is nearly a circle when the bulk conduction band is absent in the same energy region but the deformation starts to occur above 200 meV, when the bulk conduction band begins to be enclosed inside the surface constant energy contour as clearly seen in the slices at 250, 300 and 350 meV.

The observed hexagonal constant energy contour enclosing the bulk states near the E_F follows the crystal symmetry of Bi$_2$Se$_3$. However, the effective Hamiltonian, where the effect of the bulk electronic structure is neglected, is insufficient to gain further insight into the origin of the observed hexagonal deformation of the FS. We have performed a first principles calculation of the surface states with slab of 5 f.u. with a two-dimensional self-consistent full-potential augmented plane wave method. The calculated constant energy contours are shown for 250, 300, 350 and 435 meV relative to the DP in Fig. 4.7 (a). The shape is nearly a circle from zero to 250 meV, and it starts deforming at 300 meV. The theoretical Fermi wave vector magnitude at 435 meV is 0.142 $\mathring{A}$ in the $\overline{\Gamma}$-$\overline{M}$ direction and 0.118 $\mathring{A}^{-1}$ in the $\overline{\Gamma}$-$\overline{K}$, which
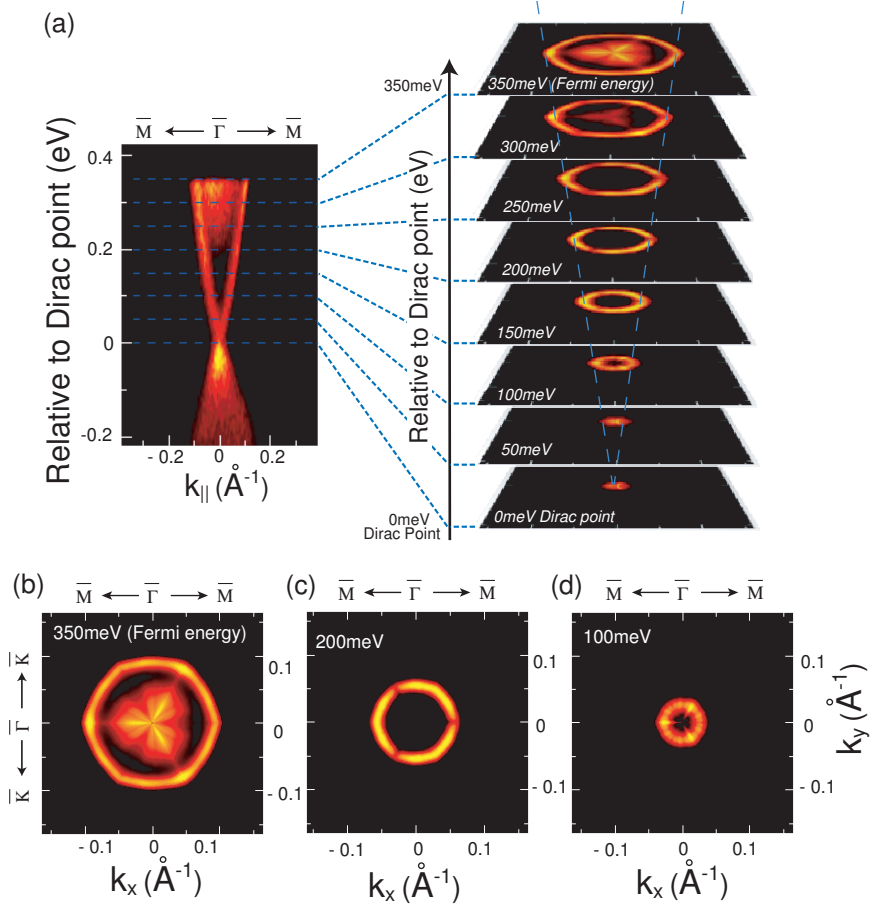
Figure 4.6: (a) Constant energy contours at several energies from 0 (the Dirac point) to 350 meV (Fermi surface). Adopted from reference [58].

is consistent with the observed values. From Fig. 4.7 which shows the comparison with calculation and experiment results for 350 meV, it is clearly found that this calculation reproduces experimental result quite well. More importantly, the electron spin begins to go vertical in a surface perpendicular orientation accompanied by the FS deformation. The out-of-plane spin polarization is maximal in the $\overline{\Gamma}$-$\overline{K}$ direction, where at 350 meV it reaches 12 % and acquired by more higher spin polarization in the unoccupied state while it vanishes in the $\overline{\Gamma}$-$\overline{M}$ line due to the mirror symmetry, as shown by Fig. 4.7 (c).

Here, we should emphasize that the experimental discovered hexagonal
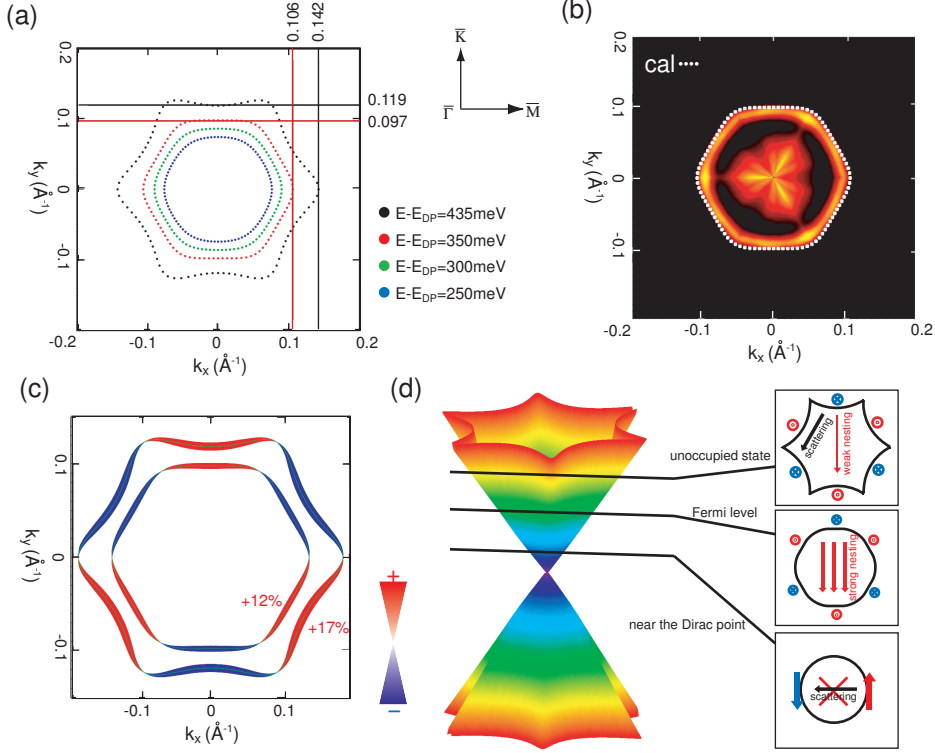
Figure 4.7: (a) Calculated constant energy contours at 250 , 300, 350 and 435 meV for a slab of 5 f.u. (b) The experimental result of Fermi surface mapping compared with the calculation result. (c) Predicted surface perpendicular projection of spin polarization for the constant energy contours at 350 and 435 meV.

deformation of the FS of Bi_2Se_3, which was believed to have an ideal Dirac cone, opens a possibility to realize the new quantum phases on the topological insulator surface. On the ideal TSS with a circular FS, the formation of a charge density wave or a spin density wave (SDW) is forbidden. Although the hexagonal deformation in Bi_2Se_3 is weaker than in Bi_2Te_3 [23], the two flat segments of hexagonal FS that faces each other with a distance of $2k_F$ along the $\overline{\Gamma}$-$\overline{K}$ direction would lead to a strong nesting and possibly generate a SDW in the surface [25]. Note that the quasi-particle interference might still be a minor effect in the vicinity of non-magnetic defects or step edges on the surface because the spin directions at the two flat segments are completely opposite due to the time-reversal symmetry. This is in contrast to the heavily warped FS in Bi_2Te_3, where the quasi-particle interference is clearly observed

in the recent STM experiment. However, the present calculation, which reproduces the observed constant energy contours quite well, further predicts that quasi-particle interference could occur above E_F where the shape of the constant energy contour becomes a snow flake like at 435 meV measured from the DP which as shown in Fig. 4.7(a). Since the predicted out-of-plane spin polarization further increases to 17 % at 435 meV, the scattering channel could be opened mainly through the vertical spin orientation as discussed for the Bi_2Te_3 surface. Furthermore, in the presence of the magnetic impurities, the quasi-particle interference will be allowed and the scattering could be affected by the shape of the FS. More importantly, since the indirect exchange coupling between the magnetic impurities is mediated by the helical TSS, we expect that one can control the magnetic order or the spin alignment by tuning the magnitude of the Fermi wave vector (k_F) on the surface of three-dimensional topological insulator [59]. Besides, a peculiar magnetic order and a colossal magnetic anisotropy would appear in the presence of the deformed FS. The summary of the hexagonal warping effect is shown in Fig. 4.7(d).
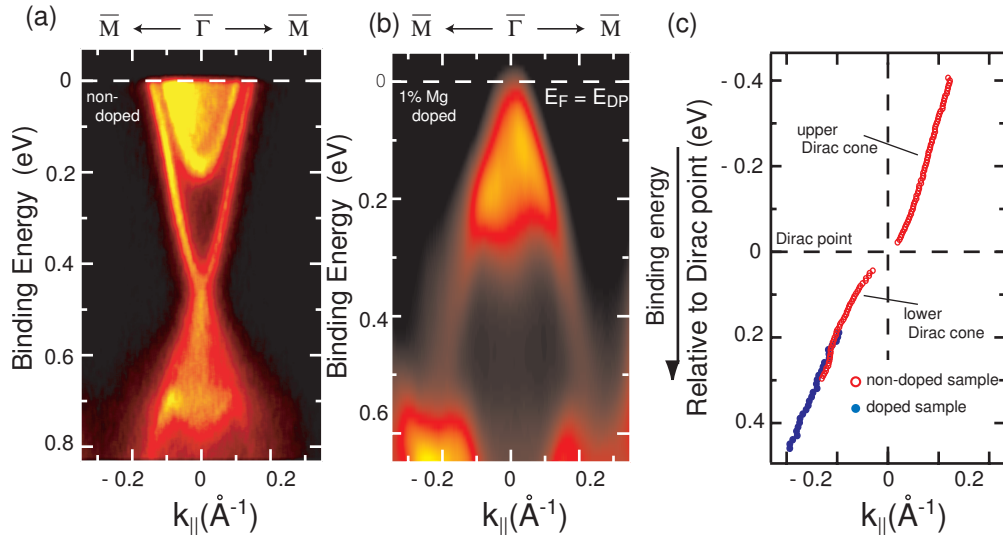
Figure 4.8: The energy dispersion curves of (a) Non-doped Bi_2Se_3 and (b) 1 % Mg-doped Bi_2Se_3 along the $\overline{\Gamma} - \overline{M}$. These intensity maxima of the Dirac state plots (c). Intensity maxima plots of the surface states of non-doped and Mg-doped samples. The longitudinal axis are set with respect to the Dirac point for non- doped sample, while for Mg doped sample, it are set the binding energy.

In order to realize the quantum topological transport, the E_F should be

brought into the energy gap by doping with non-magnetic elements. It also enables us to tune the k_F and the shape of the FS from a hexagon to a circle, associated with electron scattering and magnetic ordering as mentioned above. It should be noted, on the other hand, that the dopant themselves could become a scattering source. Among several scattering factors, a spin-orbit coupling might affect the spin lifetime significantly. As is predicted for Bi$_2$Te$_3$ surface, the impurity with a significant spin-orbit coupling could enhance quasi-particle interference especially with large momenta. It may also be expected that the foreign atom doping, which is generally adopted for tuning the topological insulator, could induce the backscattering. To minimize the backscattering originating from spin-orbit coupling, a light element with a negligible spin-orbit coupling should be chosen for the hole doping. In this work, we have tried to realize the hole doping in Bi$_2$Se$_3$ with Mg, which is light enough to have negligible spin-orbit coupling. The ARPES energy dispersion curve along $\overline{\Gamma}$-$\overline{M}$ of Mg-doped Bi$_2$Se$_3$ (Bi$_{1.98}$Mg$_{0.02}$Se$_3$) is shown in Fig. 4.8(b). While the upper Dirac cone crosses the E_F in Fig. 4.8(a), it is not seen and the E_F shifts to DP in Fig. 4.8(b). The intensity maxima plots of the TSS in both ARPES result is shown in Fig. 4.8(c) where the longitudinal axis are set with respect to the DP for non-doped sample, while for Mg doped sample, it are set as the E_B. Note that the TSS can not be identified near the DP due to the strong bulk intensity. Here, we should emphasize that the lower Dirac cone of Mg-doped sample touches non-doped one. This result indicates that the E_F is located just at DP by replacing 1 % of Bi atoms with Mg. This successful tuning of the carrier density clearly demonstrates that Bi$_2$Se$_3$ can be brought into the quantum topological transport regime.

4.3 Study for the surface magnetism and electronic structure in Mn doped Topological Insulator Bi$_2$Se$_3$ with XMCD and ARPES

4.3.1 Introduction

Dirac surface state in the the topological insulators can be distinguished from the spin-degenerate Dirac state in Graphene because the surface state in the topological insulators is described by the real spin in stead of the pseudo-spin. Therefore, it is able to directly combine with the magnetic moment, and some new physical phenomena have been theoretically proposed [60, 61, 62]. For example, while the Dirac surface state always shows gap-less feature as long as it has the time reversal symmetry, the finite gap would open at the Dirac point (DP) when the Dirac surface state combines with the local magnetic moment in perpendicular to the surface. Moreover, it has been proposed that the ferromagnetic long range ordering would appear at the surface of topological insulator with the existing magnetic impurities, due to the Ruderman-Kittel-Kasuya-Yosida (RKKY) interaction between the surface state and the local magnetic moment of magnetic impurities. This situation might be occur when Fermi energy (E_F) is located near the DP because of small k_F of Dirac surface state leading long range RKKY interaction [63].

In this section, we study the surface magnetic structure in Mn doped Bi$_2$Se$_3$ in which the gapped Dirac state has been experimentally confirmed in the previous ARPES work [64]. According to this report, the DP have been successfully tuned near the E_F possessing the small gap $\sim$ 7 meV for 1 % Mn doped sample, which is close to the condition considered by theoretical calculation for realizing ferromagnetic ordering [63]. The magnetic property of the samples has been investigated by superconducting quantum interference device (SQUID), which shows paramagnetic feature even in low temperature $\sim$2 K [64]. However it should be noted that the result obtained by SQUID would be governed by the bulk properties, which can mask the surface properties. Thus, the surface sensitive probe of the magnetic properties is strongly required to understand the magnetic interaction between the local magnetic moment and the spin polarized Dirac surface state.

Here, we focus on the surface magnetic properties in Mn doped Bi$_2$Se$_3$ by means of surface sensitive X-ray circular magnetic dichroism (XMCD) that is one of the well-established experimental method to study the magnetic

properties. We have found that the Mn ions substituted for Bi atoms work as accepter and successfully controlled E_F into around the DP. Even in the optimal situation for the predicted RKKY interaction, our XMCD results present the paramagnetic property even at the low temperature. This result indicates that the more precise model is required to predict new feature of the surface Dirac cone in topological insulator.

4.3.2 Experimental set-up

Single crystals of Bi$_2$Se$_3$ with Mn doping were prepared with a standard procedure using Bridgman method. The X-ray absorption spectroscopy (XAS) and XMCD measurement were performed at the two helical undulator beam line (BL-23SU) of SPring-8. The data acquisition was done in Total Electron Yield (TEY). The photon energy was set to be the Mn $2p$ core level. The experiment have been done under the ultra high vacuum about 8×10^{-9} Pa. The photoemission spectra were acquired with a hemispherical photoelectron analyzer (VG-SCIENTA R4000) at 10 K, using He discharged lamp (21.22 eV) at BL-9B and 31 eV synchrotron radiation light at BL-1 in Hiroshima Synchrotron Radiation Center. The energy and angular resolutions were set below 20 meV and ± 0.1 °, respectively. The samples were *in situ* cleaved under the ultrahigh vacuum for all experiment. The CI cluster model calculation has been done with a program code developed by Tanaka by means of the recursion method. MnSe$_6$ cluster model with octahedral symmetry have been assumed for this calculation.

4.3.3 Results and discussion

Figures 4.9(a) and (b) show the results of ARPES measurements for non-doped and Mn doped Bi$_2$Se$_3$ near the E_F along high symmetry line $\bar{\Gamma}$-$\bar{M}$. For non-doped sample, we used the synchrotron radiation of 31 eV photon energy, on the other hand, we used HeI$_a$ ($h\nu$=21.22 eV) for doped sample. For non-doped sample, the DP has been located around E$_B$=400 meV and the bulk conduction band is crossing the E_F due to the naturally electron doping caused by Se site vacancy. On the other hand, for the Mn doped sample, it is found that the DP shifts to lower binding energy, which means the doping Mn atoms into the crystal of Bi$_2$Se$_3$ works as accepters. This result is very similar to the substitution of 2+ alkali earth ions for Bi ions in Bi$_2$Se$_3$ as shown in following consideration, A+Bi^{3+} $\rightarrow$ A^{2+}+Bi+*hole* (A: alkali earth
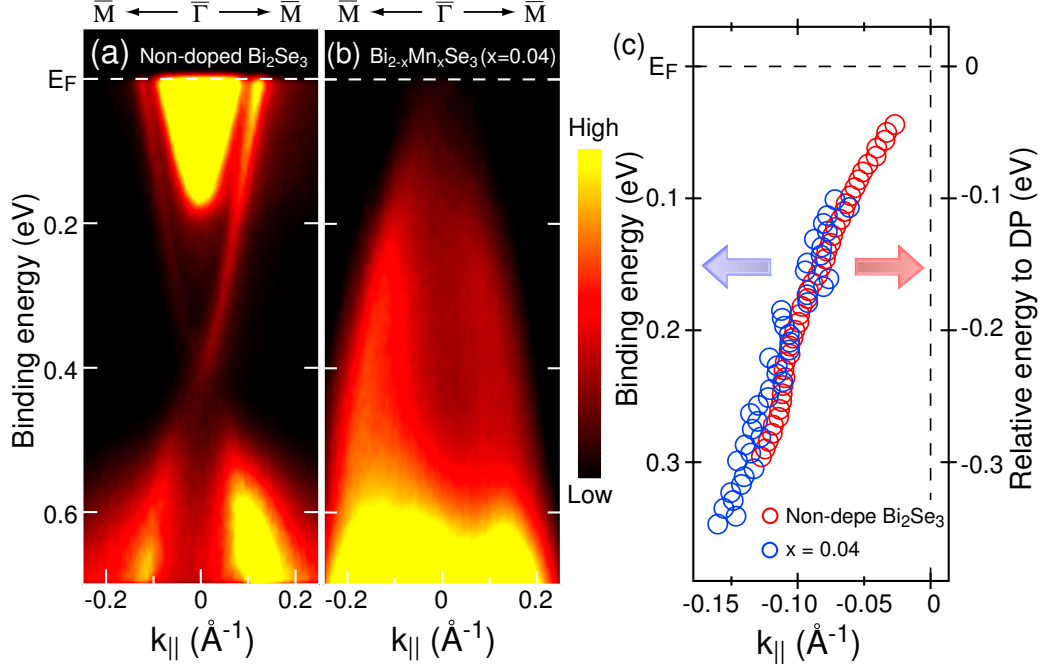
Figure 4.9: Energy band dispersion images along $\bar{\Gamma}\bar{M}$ symmetry line acquired with ARPES measurement for (a) non-doped $Bi_{2]}Se_3$ and (b) Mn doped ($x = 0.04$) sample, respectively. (c) the peak maxima plots for non-doped (red circle) and doped (blue circle) Bi_2Se_3.

metal). Note that this result also gives a evidence that Mn ions have been successfully concentrated into the bulk crystal. Figure 4.9(c) presents the comparison of the energy position of the lower part of Dirac surface state for the both samples. The peak positions have been fitted well each other. Therefore, one can expect the DP should be located near the E_F for the Mn doped sample in which thus the RKKY long range magnetic ordering can be expected at the surface due to nearly zero k_F of Dirac surface state forming spin-helical state.

In order to investigate the magnetic property at the surface for Mn doped samples, we have observed XAS and MCD spectra in the Mn $2p$ core excitation energy region of $Bi_{2-x}Mn_xSe_3$ with $x= 0.03$ and $x=0.04$. Figure 4.10(a) shows XAS spectra (μ_+, μ_- and ($\mu_+ + \mu_-$)/2) for $x=0.04$. These XAS spectra can be classified into two main structures due to the spin-orbit splitting
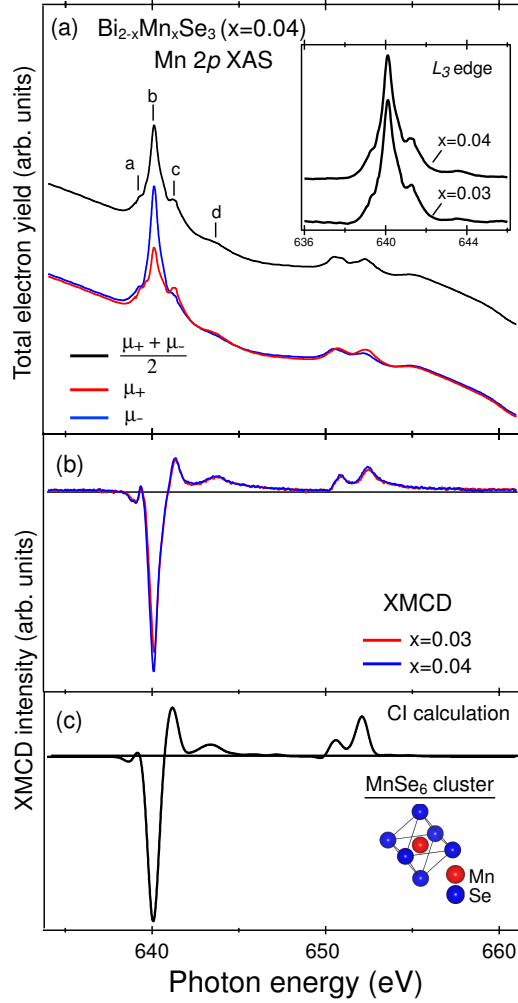
Figure 4.10: (a) Experimental Mn $2p$ XAS spectra of x=0.04 under the parallel magnetization (red: denoted by μ_+) and the anti-parallel (blue: denoted by μ_-), total XAS (black: denoted by $(\mu_+ + \mu_-)/2$) at 8.5 K and 7 T. (Inset) The total XAS spectra for x=0.04 and x=0.03 with subscribed back ground at L_3 energy region. (b) MCD spectra of x=0.03 (red) and 0.04 (blue), obtained by $(\mu_+ - \mu_-)$.

of the Mn $2p$ core hole as the final state, where L_3 (L_2) absorption is located in 638-646 eV (649-656 eV), denoted by $a - d$ for L_3. For L_3 XAS, the complicated structures are found, which are derived from the multiplet splitting of various final states excited by the dipole transition from $2p$ to

$3d$. The experimental Mn $2p$ absorption spectra can be reproduced well by the theoretical calculation of the Mn $2p$ XAS taking into account only $3d^5 \rightarrow 2p^5 3d^6$ [65]. Therefore, we concluded that the Mn ions substitution from the Bi atoms in Bi₂Se₃ mainly exist as Mn^{2+} (d^5) state. This result is consistent with our ARPES results that the Mn substitution for Bi dopes holes into the bulk possibly via the following process;

$$Mn + Bi^{3+} \rightarrow Mn^{2+} + Bi + hole \qquad (4.2)$$
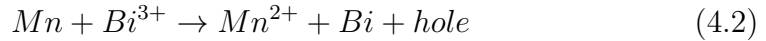
Figure 2(b) shows MCD spectra for samples with different doping level. These MCD spectra also show multiplet structures for L_3 edge region. The overall MCD features show a small negative hump at lower energy ~ 638 eV than where a negative prominent peak $\sim$640 eV, and two small positive signals at higher energy $\sim$642 eV in the L_3 region and positive double peak structures in L_2 region. Focusing on the small negative hump structure, one can find that there is in same energy to a state in the XAS spectrum. According to our CI calculation as explained below, the a state can be reproduced quite well with considering the crystal field and therefore we expect that Mn $3d$ electrons feel the crystal field from the around Se atoms. In addition, it has been well known for XAS and XMCD study of $Ga_{1-x}Mn_xAs$ that there are two components derived from the intrinsics and extrinsic Mn doped electronic structure and furthermore the spectra shape depends on the Mn doping level due to the inhomogeneous states [66]. However, from the inset figure in Fig. 4.10(a), the spectral feature of XAS is independent of the doping level. Thus, the Mn ions are considered to be in the Bi₂Se₃ homogeneously for our sample. Using the XAS and XMCD spectra, we have applied the XMCD sum rules [67] for both doped samples with the Mn $3d$ electron number ~ 5.1 obtained from our CI calculation as mentioned below. The spin magnetic moment $\langle M_S \rangle$ have estimated at 8.5 K and 7 T to be 2.7±0.6 and be 2.5±0.8 (μ_B per Mn ion) for x=0.04 and 0.03 samples, respectively. The ratio for the orbital magnetic moment ($\langle M_L \rangle$) to $\langle M_S \rangle$, $\langle M_L \rangle / \langle M_S \rangle$ to be $\sim$0.04 for both concentration, this result shows $\langle M_L \rangle$ is quite small probably due to the Mn $3d^5$ state, that is, the high spin state.

Next, we have carried out the $MnSe_6$ cluster model calculation to quantitatively understand the experimental Mn $2p$ XAS and MCD spectra. For the calculation, we assumed the cluster with octahedral symmetry as shown in the inset figure 4.10(c) and considered CIs for the $|3d^5 L\rangle$, $|3d^6 \underline{L}\rangle$ states in the Mn ground state, where $\underline{L}$ denotes a hole in the ligand bands. The calculated Mn $2p$ XMCD spectra are shown in Fig 4.10(c), which can reproduce quite

	Δ	$pd\sigma$	U	Q	$10Dq$
$x = 0.04$	3.0	0.8	4.0	5.0	0.4

Table 4.1: Electronic structure parameters for Mn doped Bi_2Se_3 $x = 0.04$. Δ, $pd\sigma$, U, Q and $10Dq$ are given in units of eV.

well the experimental one (Fig. 4.10(b)). The employed parameters for the CI cluster model calculation are as follows: The charge transfer energy Δ is defined as $\Delta = |3d^6\underline{L}\rangle$-$|3d^5L\rangle$, p-d transfer integrals are defined as $(pd\sigma)$, the $3d$ on-site Coulomb interaction is defined as U, the Coulomb interaction between $3d$ electron and $2p$ core hole is defined as Q and the crystal field splitting is $10Dq$. The parameters optimized to reproduce the experimental results are listed in Table 4.1 and other parameters will be found in elsewhere [68, 69]. As a result, the weights of the $3d^5L$, $3d^6\underline{L}$ configurations in the Mn ground state of $Bi_{2-x}Mn_xSe_3$ are estimated as 91%, 9%, respectively. The occupancy of the Mn $3d$ sate is evaluated as 5.1. Finally, we obtained the $\langle S \rangle$=2.48 and $\langle L \rangle \sim$0, which is consistent with our XMCD result in the point of the size of $\langle M_S \rangle$ and quenching the orbital moment due to the Mn $^{2+}$ (d^5) state.

In order to determine the magnetic feature at the surface, we have observed the temperature (T) and external magnetic field (H) dependence of XMCD peak intensity at the L_3. Figures 4.11(a) and (b) show the T dependence under H of 5 T and the H dependence at the low T of 8.5 K for the doped samples x=0.03 and x=0.04, respectively. The scale of longitudinal axis are set with our sum rule result at 8.5 K and under 7 T as we described above. For figure 4.11(a), we found that the T dependence is reproduced by Currie's law which scales $1/T$ even below low temperature around 10 K although the line shape has to be written by Currie-Weiss law in the case that the ferromagnetic ordering is realized. For figure 4.11(b), the H dependence could be reproduced well by the Langevin function and there is no hysteresis loop even for small H below 0.8 T as the inset figure. Therefore, we have concluded that the magnetic feature for x=0.03 and x=0.04 are para like even in the low $T \sim$8.5 K.

Here the surface contribution in the experiment will be discussed. According to ARPES study for the Bi_2Se_3 thin film [70], the charge distribution forming Dirac surface state in the Bi_2Se_3 are uniformity located within the two quintuple layers whose size are about 20 Å. Therefore, the special proper-
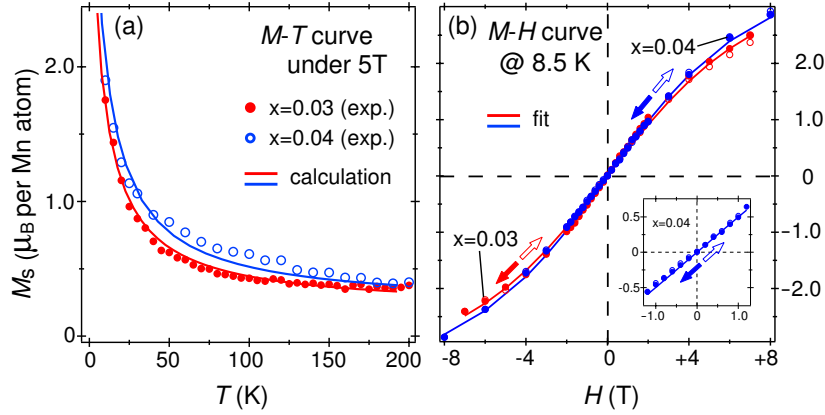
Figure 4.11: (a) Temperature (T) dependence of the M_S estimated with the XMCD spectra under 5T and calculation lines using curie's law with the parameter obtained by the Langevin function fitting described in (b) for x=0.03 (filled circles) and x=0.04 (open circles). (b) The external magnetic strength (H) dependence of the M_S at 8.5 K with fitting lines using Langevin function and the one for small H region (inset). The data taken from positive H to negative H (filled circles) and then back to positive H (open circles).

ties caused by the interaction between Dirac surface state and local magnetic moment will be found in this region. Considering the probing depth for our XMCD measurement with using soft x-ray and TEY, it usually would be about 20-80 Å. Therefore, we expect that the surface sensitivity should be high enough to acquire the surface magnetic properties and thus Mn $2p$ spectrum we obtained should be mainly derived from Mn ions surrounded by the Dirac surface state forming spin-helical state. This is why, it has been proved that the surface magnetic property is determined to be the para like in Mn doped Bi_2Se_3 even if the DP is located near the E_F. This result imply that it is not simple to realize the surface magnetism in the doped topological insulator, particularly, to predict new feature of the surface Dirac cone in topological insulator with precision, the more precise model is needed.

4.4 Conclusion

In conclusion, we have studied electronic and magnetic structures of the prototypical topological insulator Bi_2Se_3 with non-magnetic and magnetic

impurities.

The hexagonal deformation of the FS of TSS in Bi$_2$Se$_3$ has been established by our high-resolution ARPES experiment with linearly polarized lights. The flat segments facing each other in the hexagonal FS topology would enable a strong nesting, possibly leading to a new quantum phase such as a SDW. Further FS deformation can be expected in the unoccupied state, which would generate the quasi-particle interference even by a non-magnetic impurity on the surface. Finally, we have demonstrated that the E_F of naturally electron doped Bi$_2$Se$_3$ can be tuned by 1 % Mg doping in order to realize the quantum topological transport.

We have further investigated and studied the electronic and magnetic structures in the subtle magnetic impurity doped topological insulator, Bi$_{2-x}$Mn$_x$Se$_3$ (x=0.03 and x=0.04) by means of ARPES and XMCD measurements. Our ARPES result revealed that the Mn ions substituted for Bi atoms work as accepter and it is successful to move the E_F to around the DP. This situation is close to the condition considered by theoretical calculation for realizing ferromagnetic ordering. The XMCD results represent that the obtained XMCD spectra can be reproduced quite well by the CI considering Mn $3d^5$ state. Investigating the T and H dependence of L_3 peak intensity in XMCD spectra, it is finally revealed the surface magnetic structure that the paramagnetic property are formed between localized $3d$ electron in Mn atoms state even at the low temperature. This result imply that it is not simple to realize the surface magnetism in the doped topological insulator, particularly, to predict new feature of the surface Dirac cone in topological insulator with precision, the more precise model is needed.

Chapter 5

Searching of the ideal topological insulator in ternary chalcogenides

5.1   Introduction
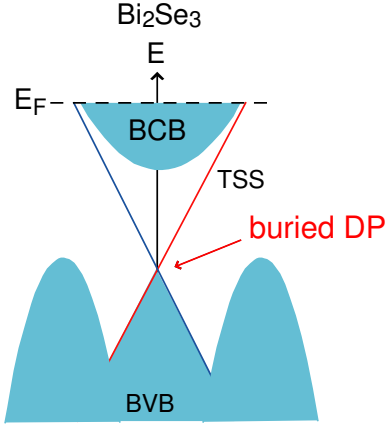
Figure 5.1: Schematic energy band structure images for Bi_2Se_3 as seen in the previous ARPES measurement [22] and our study in Chap. 4.2.

As a topological insulators, the band structure near the Dirac point (DP) is quite important because the novel topological surface state (TSS) has great potential to bring several electromagnetic topological phenomena into reality when the DP is located near the Fermi energy (E_F) within the bulk energy gap [60, 61, 62].

Up to now, the many experimental effort are exerted on the surface of th binary chalcogenide topological insulators, such as Bi_2Se_3 and Bi_2Te_3. However, as we studied in Chap. 4.2, the topological surface state even in Bi_2Se_3 is affected by the hexagonal warping effect, which may open the electron scattering channels. Furthermore, recent spin-resolved ARPES results [26, 71] have represented that spin-helical textures were clearly identified above the DP in these topological insulators but the relevant feature was obscured below it. This probably stems from their particular band structures, in which the lower part of the TSS (LP-TSS) is buried in the bulk valence band (BVB), as is actually observed in the ARPES spectra (Fig. 6.1(a)). Indeed, large bulk conduction mainly contributes to the transport in these materials. Therefore, it is quite important to extend the search for topological insulators with an ideal and isolated spin helical TSS to a wider range of materials. Recent first-principles studies suggested a variety of candidates with nontrivial electronic

structure [72, 73, 74, 75, 76]. In this chapter, we will focus on the thallium-based ternary compounds in Sec. 5.2 and the Pb-based ternary chalcogenides in Sec. 5.3.

5.2 Experimental Realization of a Three-Dimensional Topological Insulator Phase in Ternary Chalcogenide TlBiSe$_2$

5.2.1 Thallium based ternary chalcogenides
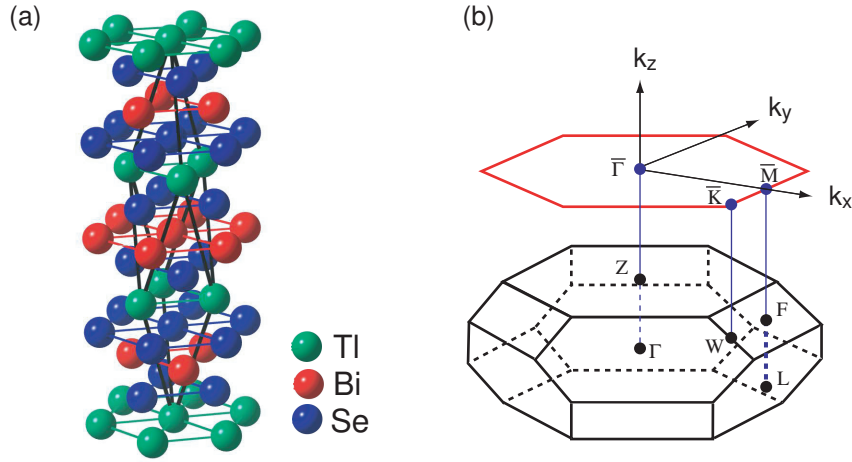
Figure 5.2: (a) Crystal structure of TlBiSe$_2$ (b) Surface and bulk Brillouin zones of TlBiSe$_2$

Thallium-based III-V-VI$_2$ ternary compounds (TlBiSe$_2$ and TlBiTe$_2$)have been proposed as a new family of three-dimensional topological insulators [72, 73, 74]. These compounds form rhombohedral crystal structure with the space group D_{3d}^5 ($R\overline{3}m$) as shown in Fig.5.2 (a) with the rhombohedral units cells described denoted with solid line. For rhombohedral description, the lattice parameter is $a_R = 7.728$ Å and $\alpha = 31.92°$, while $a_H = 4.24$ Å and $c_H = 22.33$ Å for the hexagonal one [77]. This structure is similar to Bi$_2$Se$_3$, where five-atomic layers form a quintuple layer Se1-Bi-Se2-Bi-Se1, and the coupling between two quintuple layers is of the van-der-Waals type. On the contrary, Thallium-based materials have a three-dimensional structure because each

Tl (Bi) layer is sandwiched by two Se layers with strong coupling between neighboring atomic layers. Because of these three-dimensional feature of the ternary compounds, the broken bonds at the cleaved surface may give rise to trivial surface states. The theoretical studies have indeed revealed the presence of such surface states in addition to the topological ones [78]. This calls for an angle-resolved photoemission spectroscopy (ARPES) experiment with broadly tunable photon energy, which allows us to separate out two-dimensional electron states in this new class of ternary compounds and it is a one of the most suitable method to directly prove the surface state. There are two main purposes in this study. The first one is to directly probe the existence of the TSS on the $TlBiSe_2(111)$ surface by ARPES using tunable synchrotron radiation. The second one is to determine the energy and k-space location of the bulk continuum states with respect to the Dirac cone. Because of the strongly three-dimensional character of the ternary compounds, a tunable photon energy is indispensable to map the three-dimensional bulk band structure.

5.2.2　Experimental set-up

The single crystalline of $TlBiSe_2$ were grown by using Bridgman methods. Stoichiometric mixtures of Tl (5N: grain, Kouzyundo-kagaku), Bi (5N: shots, Mitsuwa) and Se (5N: shots, Mitsuwa) were melted in evacuated quartz ampules at 800 °C and below $5{\times}10^{-7}$ Torr for a day to secure complete reaction and homogeneous melt at the higher temperature than the melting point of $TlBiSe_2$, 800 $°C$. Then slowly cooling with 0.5 °C/h in the vicinity of the melting point to room temperature for about three weeks. Here, we summarize the procedure to make a single crystal of the $TlBiSe_2$ as follow.

(1) Cleaning high-purity Bi and Se elements with nitric acid (1N) and acetone for 5 minutes, respectively.

(2) Cleaning Tl element with only acetone for 5 minutes in the N_2 flowing box.

(3) Enclosing these elements in the evacuated quartz ampules below $5{\times}10^{-7}$ Torr.

(4) Heating ampules in Bridgman furnace and gradually cooling under the temperature program as described in Fig.5.3.
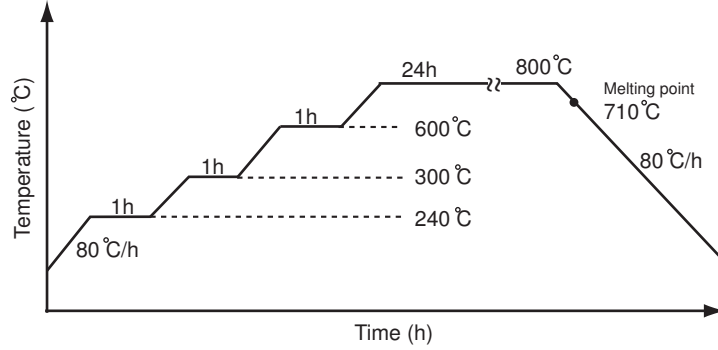
Figure 5.3: Temperature control sequence of Bridgman furnace for the fabrication of a single crystal of the $TlBiSe_2$.

Procedure (2) needs meticulous attention because Tl is very active material, which can be easily oxidized in air. In order to keep thallium shots be high-purity, the thallium shots is stored in liquid paraffin. Therefore, we removed liquid paraffin by the dilapidation of acetone in the N_2 gas flowing box.

The resultant crystals are cleaved along the basal plane (111) with a shining mirror like surface as shown in Fig.5.4 (a) and it is rigid than Bi_2Se_3 due to the non-weak bonding. The crystal structure of the $TlBiSe_2$ was confirmed by Laue pattern, and X-ray powder diffraction pattern as are shown in Fig.5.4 (b) and (c), respectively. In Fig.5.4, we find that single crystalline sample is successfully obtained because very sharp diffraction spots were obtained in Laue and LEED in Fig.5.4 (d). In Fig.5.4(c), we fitted the experimental data (red color line) to calculated one (blue color line) and these peak positions are corresponding to each other.

ARPES experiment was performed with synchrotron radiation at the linear undulator beam line (BL-1) and the helical undulator beam line (BL-9) of Hiroshima Synchrotron Radiation Center. The photon energy range was 22-58 eV to estimate the positions of the bulk state for BL-1, while for BL-9, 8.5 and 21 eV photon energies were used to resolved the Fermi surface of $TlBiSe_2$. The photoemission spectra were acquired with a hemispherical photoelectron analyzer (VG-SCIENTA R4000) under the 20 K. The overall energy and angular resolutions were set below 20 meV and 0.1 or 0.3 °. The samples were *insitu* cleaved under the ultrahigh vacuum below 1×10^{-8} Pa.
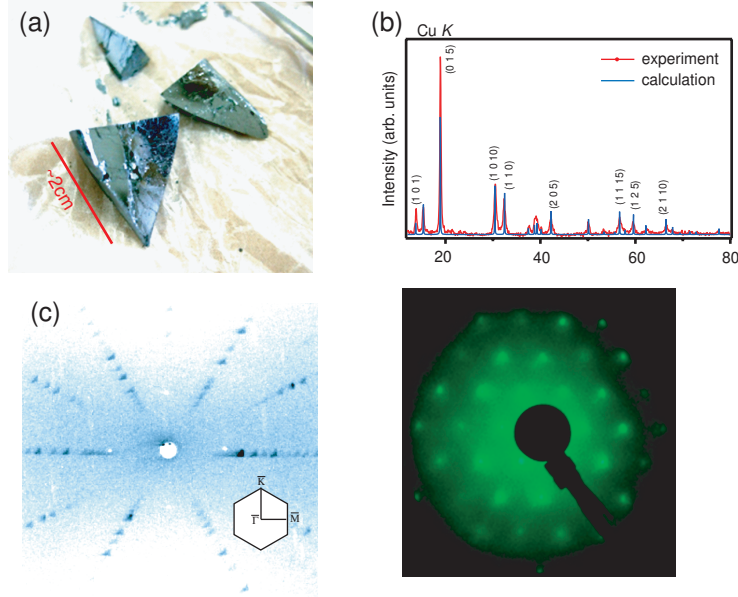
Figure 5.4: (a) Photo of TlBiSe$_2$. (b) X-ray powder diffraction pattern. (c) Laue diffraction pattern of (111) plane. (d) LEED pattern of (111) surface obtained with the kinetic primary electron beam of 180 eV.

5.2.3 Results and discussion

Fig.5.5 shows the experimental energy dispersion imaging and their corresponding second derivative intensity plot acquired by ARPES measurement along $\overline{\Gamma}$-$\overline{M}$ line with photon energy of 21 eV at BL-9. This result was symmetrized at $\overline{\Gamma}$ point. The $\overline{M}$ point of the surface Brillouin zone is ~ 0.86 $\mathring{A}^{-1}$ as denoted with dotted line in Fig. 5.5 a bulk of energy dispersions are clearly observed. Note that the liner dispersion which forms a cone in the two dimensional state are clearly observed near the $\overline{\Gamma}$ point and these bands intersect at the binding energy E_B=390 meV, corresponding to the DP. Moreover, we have found the bulk conduction band (BCB) is enclosed inside the upper Dirac cone (DC) and its band bottom is located at E_B=200 meV due to the spontaneous electron doping effect in the TlBiSe$_2$ samples, which changes the bulk state into metallic feature. The strong signals are observed at the binding energies E_B=1.5 and 2.0 eV near the $\overline{\Gamma}$ point. According to the first principle band calculation, there are other two-dimensional surface states in the bulk energy gap, which might contribute to a strong photoelectron intensity. The green dots in Fig. 5.5 show the peak energy positions obtained from
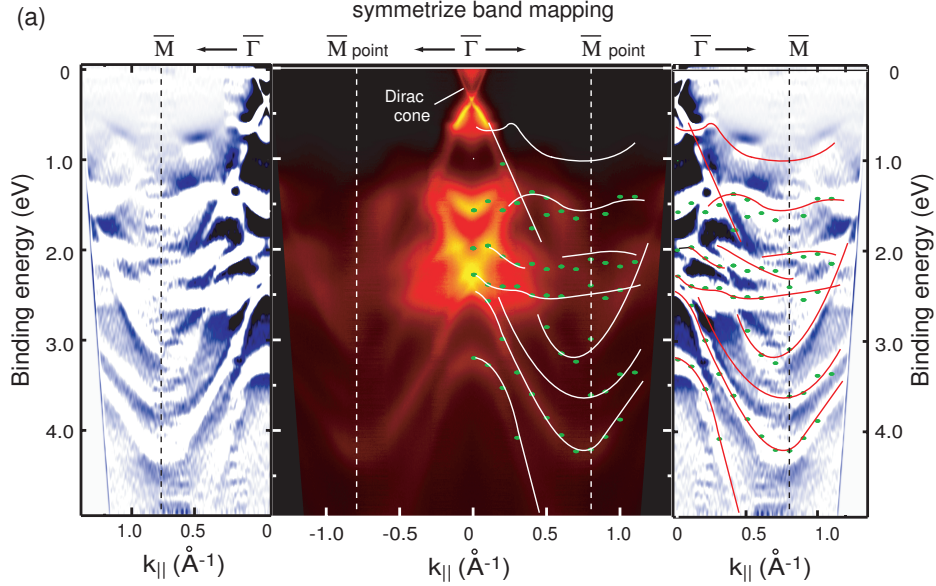
Figure 5.5: The ARPES result of s single crystal of TlBiSe$_2$ which is symmetrized at the $\overline{\Gamma}$ point and the second energy derivative intensity plot measured with photon energy of 21 eV at BL-9.

the energy distribution curves (EDCs) of and the solid lines correspond to the bulk energy band dispersion interpolated among green dots. Here, note that the no-state crosses the Fermi energy except for the TSS and BCB near the $\overline{\Gamma}$ point, so it can be determined that TlBiSe$_2$ is the three-dimensional topological insulator which possesses a single TSS at the $\overline{\Gamma}$.

Next, we focus on the TSS. In the experiment, the photon energy to have been changed precisely observation and tuning photon energy from 22 to 70 eV at BL-1. The photoelectron intensity from the BCB is enhanced at lower photon energies $h\nu$ = 22-30 eV. On the other hand, near 50 eV, the photoelectron intensity from BCB can be suppressed. Here, we show the ARPES results with photon energy of 58 eV with p-polarized light along the $\overline{\Gamma}$-$\overline{M}$ and $\overline{\Gamma}$-$\overline{K}$ lines in Fig. 5.6 (a) and (b), respectively. Here, we should emphasize that the spectral weight of the BCB is suppressed and the X-shaped massless energy dispersion clearly seen along both high-symmetry lines. The BVB energetically overlaps with the surface state below the DP and its maximum is located at E_B=540 meV away from the zone center (at $k_\parallel$=0.3 $\mathring{A}^{-1}$) as clearly seen in Fig. 5.6(a). The BVB is anisotropic become
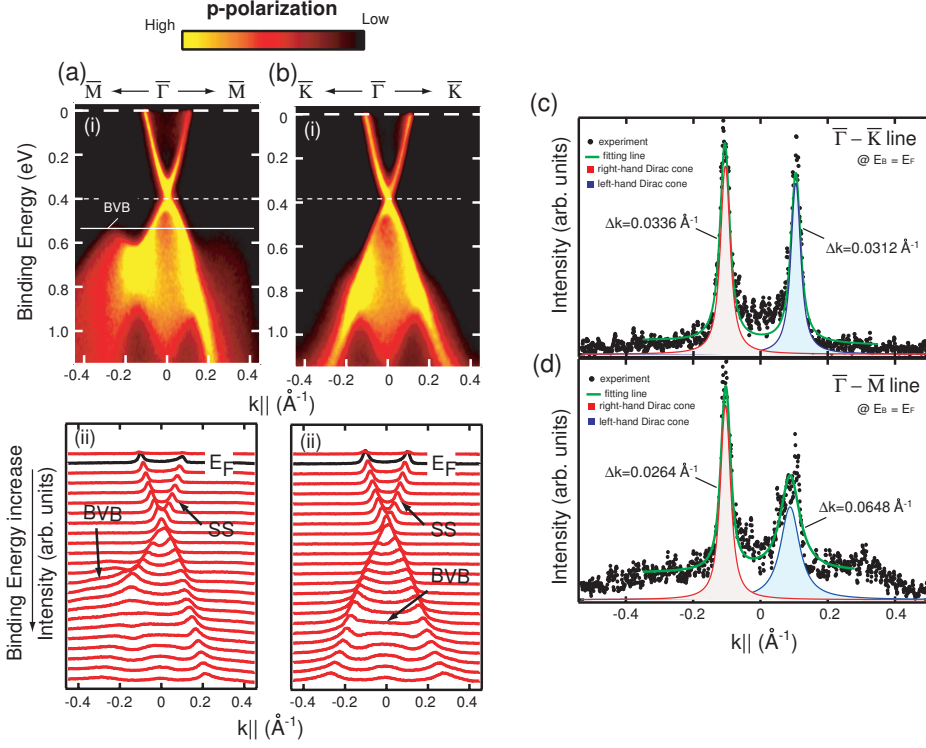
Figure 5.6: ARPES result of $k_\parallel$ dispersion and momentum distribution curves (MDCs) measured with photon energy of 58 eV with p-polarized light at BL-1 along the (a) $\overline{\Gamma}$-$\overline{M}$ and (b) $\overline{\Gamma}$-$\overline{K}$ lines adapted from reference [79]. (e) and (c) show the MDCs at the Fermi energy along $\overline{\Gamma}$-$\overline{K}$ and $\overline{\Gamma}$-$\overline{M}$, respectively and which energy window is 2 meV.

it lies much deeper in the $\overline{\Gamma}$-$\overline{K}$ than in the $\overline{\Gamma}$-$\overline{M}$ line.

Here, we show the results of the fitting analysis to the MDCs of surface Dirac cone at the E_F along both high symmetry lines by using two Lorentzian functions for Fig. 5.6(c) $\overline{\Gamma}$-$\overline{M}$ and (d) $\overline{\Gamma}$-$\overline{K}$, respectively. For both lines, the left (right) peaks as shown by the red (blue) color solid lines and the total fitting result including constant and linear background are shown by green one. The magnitude of the Fermi wave vector is estimated from the intensity maxima of MDCs to be 0.105 $\AA^{-1}$ for both $\overline{\Gamma}$-$\overline{M}$ and $\overline{\Gamma}$-$\overline{K}$ directions. This indicates that the an isotropic Dirac cone electron can be expected on the TlBiSe$_2$(111) surface, in contrast to the heavily warped Dirac cone in Bi$_2$Se$_3$ and Bi$_2$Te$_3$. Then, we have estimated the mean free path (l_m) from the MDC
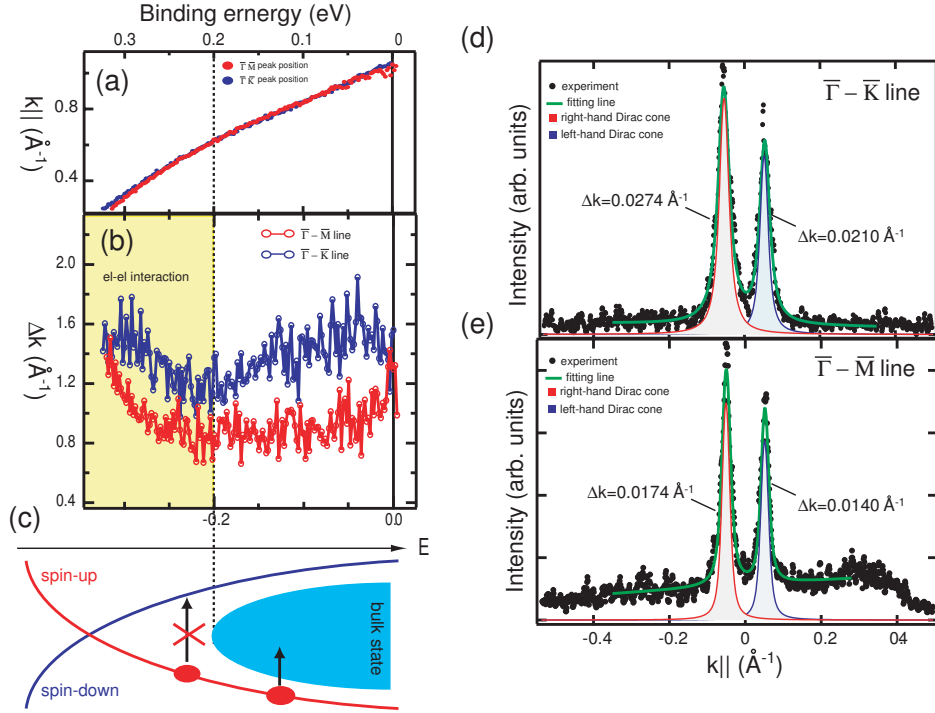
Figure 5.7: The MDC analysis of the Fig. 5.6 with two Lorentzian profiles: (a) The intensity maximal plots for the two high symmetry lines. These peak positions was identified with right hand side surface state. (b) The width of Lorentzian versus binding energy plots, which corresponds to $\frac{1}{l_m}$ where l_m is the mean free path. These obtained with the right (left) hand side surface state for $\overline{\Gamma}$-$\overline{K}$ ($\overline{M}$). (c) The schematic figure of the bulk conduction band and surface Dirac cone. (e) and (c) show the MDCs at E_B=250 meV where two Lorentzians are the most sharp along $\overline{\Gamma}$-$\overline{K}$ and $\overline{\Gamma}$-$\overline{M}$, respectively and which energy window is 2 meV.

width $\delta k_\parallel$ as given by,

$$l_m = \frac{1}{\delta k_\parallel} \tag{5.1}$$

For TSSs of topological insulators, it can be expected that the surface electron possesses the extremely long l_m due to the protection from the backscattering by non-magnetic impurities. Here, the result of $\delta k_\parallel$s of two Lorentzian profiles for $\overline{\Gamma}$-$\overline{K}$ lines are 0.0336 and 0.0312 $\mathring{A}^{-1}$ for the left- and right-peak of surface states, respectively. Note that, for the Shockley surface state, $\delta k_\parallel$ are generally about 0.020 $\mathring{A}^{-1}$ and its l_m is about 50 $\mathring{A}$ which is described

in [80]. So, this result implies that the l_m of the surface electron of TlBiSe$_2$ is smaller than that of the Shockley surface state, which is in contrast to people belief that topological insulator possess extremely large l_m. But the result for $\overline{\Gamma}$-$\overline{M}$ gives idea that the bulk intensity can affect the MDCs analysis. In Fig. 5.6(d), we find that the right peak has a small intensity and is strongly broadened with $\delta k_\parallel = 0.0648$ $\mathring{A}^{-1}$, while the left one shows much smaller width with $\delta k_\parallel = 0.0264$ $\mathring{A}^{-1}$. This asymmetric feature indicates that extra photoelectron small intensity from the bulk conduction band still remains which would affect the surface state if the bulk conduction intensity is suppressed by k_z dispersion features. Therefore, the right peak of the surface state can be much more affected by the bulk intensity than the left one.

Here, we should note that the bulk state, which energetically overlaps with the surface state, can induce some interaction into the topological surface state. As a consequence, the l_m will become shorter and thus $\delta k_\parallel$ will be larger. Fig. 5.7 (a) and (b) show intensity maxima and $\delta k_\parallel$ plots as a function of binding energy, respectively. From the result of Fig. 5.7 (a), we find that the energy dispersions along two high-symmetry lines almost overlap with each other, implying an isotropic feature, which is consistent with above discussion. From Fig. 5.7 (b), the $\delta k_\parallel$ initially decreases in going from lower E_B and starts to increase from E_B=200 meV for both high-symmetry lines. Note that this E_B corresponds to the bottom position of the BCB as schematically shown in Fig. 5.7 (c). Energetically overlapping with bulk state is an suitable state for TSS because the surface electron can be easily scattered into the bulk band. Therefore, the electron life-time becomes shorter, as a consequence, the $\delta k_\parallel$ larger. Recently, the similar is reported in Bi$_2$Se$_3$ [81]. However, we still expect the long l_m as a hallmark of the TSS state below the bulk conduction bottom. Here, we show the result of MDCs analysis at E_B=250 meV where $\delta k_\parallel$ takes minimum value (see Fig. 5.7 (b)) as shown in Fig. 5.7 (d) for $\overline{\Gamma}$-$\overline{K}$ and (e) for $\overline{\Gamma}$-$\overline{M}$. From this result, we see that the peak width crucially becomes sharper for both high-symmetry lines, especially, the $\delta k_\parallel$ is smaller than that of the Shockley surface state. Here, the l_m is estimated as 70 $\mathring{A}$ for $\overline{\Gamma}$-$\overline{M}$. More importantly, we should note that the $\delta k_\parallel$ is expected to be smaller if the E_F is tuned at this energy. Because electron-electron interaction should be suppressed near the E_F. Therefore, we can expect that topologically protected feature on the surface of topological insulator can be observed with ARPES measurement if the E_F is tuned into the bulk band gap.

Now, we compare the TSS of TlBiSe$_2$ with Bi$_2$Se$_3$. Note that, when ex-
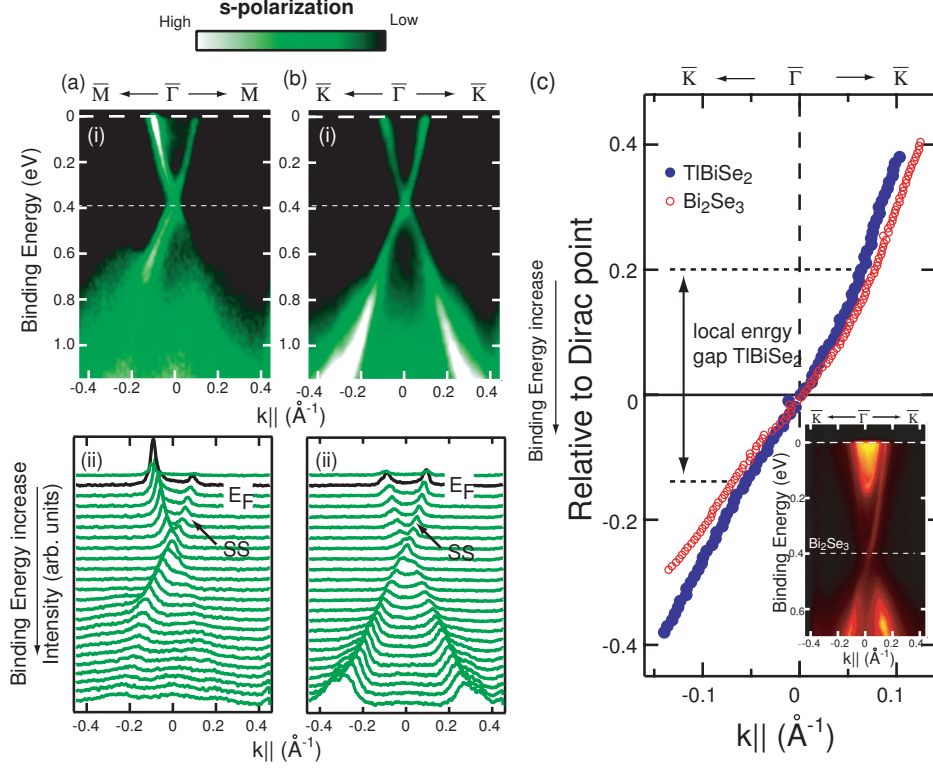
Figure 5.8: ARPES result of $k_\parallel$ dispersion and momentum distribution curves (MDCs) measured with photon energy of 58 eV with s-polarized light along (a) $\bar{\Gamma}$-$\bar{M}$ and (b) $\bar{\Gamma}$-$\bar{K}$ lines. (c) Intensity maxima of the surface state along $\bar{\Gamma}$-$\bar{K}$ line together with the result for Bi$_2$Se$_3$ (see Chap. 4.2). The Dirac point is located at E_B=390 meV and 400 meV for TlBiSe$_2$ and Bi$_2$Se$_3$, respectively. Adapted from reference [79]

cited with s-polarized light, the contribution of bulk valences band is strongly suppressed with respect to the surface state along $\bar{\Gamma}$-$\bar{K}$ line as shown in Fig. 5.8 (b), which enables us to evaluate the surface state character more precisely for TlBiSe$_2$. In Fig. 5.8 (c), we plot the energy versus $k_\parallel$ of the intensity maxima for the surface state measured from the DP along $\bar{\Gamma}$-$\bar{K}$ line and compare it with our that of Bi$_2$Se$_3$. The TSS is seen to be not exactly linear on TlBiSe$_2$(111), however, it is much closer to ideally linear in TlBiSe$_2$ than in Bi$_2$Se$_3$, especially in the local energy gap window, 150 meV below and 200 meV above the DP. The energy dispersions are slightly warped toward small $k_\parallel$ approximately 200 meV above the Dirac point, where the bulk

conduction band is enclosed inside the upper Dirac cone. The energy dispersion is steeper than in Bi_2Se_3: the evaluated Fermi velocity is 7×10^5 m/s in $TlBiSe_2$ and 6×10^5 m/s in Bi_2Se_3. Also the velocity near the DP is larger in $TlBiSe_2$ (3.9×10^5 m/s) than in Bi_2Se_3 (2.9×10^5 m/s).
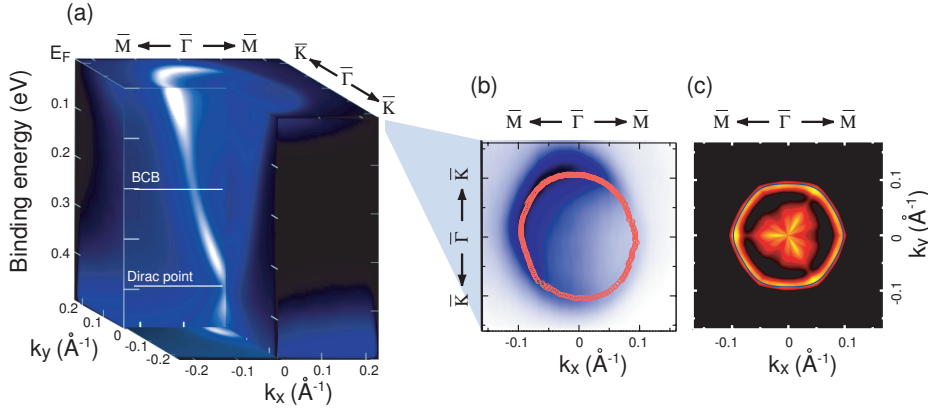
Figure 5.9: (a) Three-dimensional illustration of $TlBiSe_2$ (b) The Fermi surface of $TlBiSe_2$ obtained with the low photon energy of 8.5 eV at BL-9, where peak plots are shown by the red circle. (c) The Fermi surface of Bi_2Se_3 show together with calculated Fermi surface (see Chap.4.2).

Here, we should note that the confirming a shape of the FS is very important to determine the figure of merit of topological insulator. Especially, the hexagonal warping effect has been known as one of the most important factor which induces the scattering into the TSS. In order to precisely observe the Fermi surface of $TlBiSe_2$, we used the low photon energy of 8.5 eV at BL-9. Its result is shown in Fig. 5.9(a) with the FS of Bi_2Se_3 in Fig. 5.9 (b). For the Bi_2Se_3, the anisotropic band dispersion has been observed and the shape of Fermi surface is a hexagon due to a deformation of the constant energy contours caused by the warping effect. On the other hand, the anisotropic band dispersion is not observed in this work in the surface state of $TlBiSe_2$, which is shown in Fig. 5.7 (a). Reflecting this result, we observed almost isotropic Fermi surface in $TlBiSe_2$. Therefore, we found that ideal Dirac cone which possesses the isotropic Fermi surface for large energy region is realized on the surface of $TlBiSe_2$.

The three-dimensional k-space location of the bulk states should be elucidated because it determines the probability of the surface-bulk electron scattering. To know the k_z locations, we performed a detailed photon energy

116
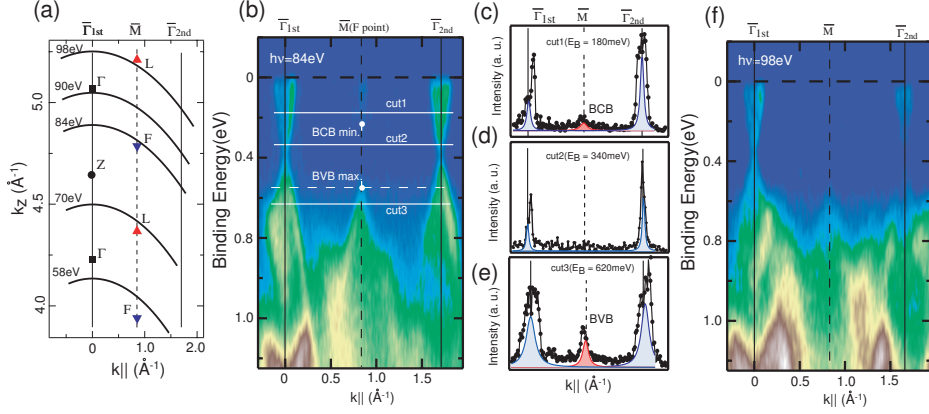
Figure 5.10: (a) k_z plot as a function of $k_{\parallel}$ with V_0=11.7 eV [22]. In going from $h\nu = 58$, and 70 to 98 eV, the whole Brillouin zone is scanned along the c axis. (b) ARPES energy dispersions for $h\nu = 84$ eV at BL-1 i the wide $k_{\parallel}$ range along $\overline{M} - \overline{\Gamma} - \overline{M}$ together with momentum distribution curves at the binding energies of (c) 180, (d) 340 and (e) 620 meV (cut1-3) where red (blue) color shows bulk (surface) state.

dependence study in a wide $k_{\parallel}$ range. At $h\nu$=84 eV, as illustrated in Fig. 5.10 (a), the ARPES spectrum mainly reflects the electronic states at the F point, which projects into the $\overline{M}$ point of the SBZ. Fig. 5.10 (b) shows the ARPES energy dispersions in the wide $k_{\parallel}$ range along $\overline{M}$-$\overline{\Gamma}$-$\overline{M}$ with $h\nu$=84 V at BL-1. The surface state at the $\overline{\Gamma}$ points in the 1st ($\overline{\Gamma}_{1st}$) and 2nd ($\overline{\Gamma}_{2nd}$) SBZs is confirmed to be identical. The intensity peak from the BCB moves downward as the incident photon energy increases from 74 eV and reaches the maximal binding energy at $h\nu$=84 eV (F point), as shown in Fig. 5.10 (b). Also, the emission from the BVB comes from near the $\overline{M}$ point at $h\nu$=84 eV. In order to more clearly see the band edges at $\overline{M}$, we show in Fig. 5.10 (c)-(e) MDCs at three binding energies. From these curves, we can determine the conduction band minimum to be at E_B=240 meV and the valence band maximum at E_B=540 meV. At $h\nu$=98 eV that corresponds to the emission from the L point, the intensity of the BCB vanishes as shown in Fig. 5.10 (f). As schematically summarized in Fig. 5.11 (a), no states other than the Dirac cone exist near the $\overline{\Gamma}$ point in this energy gap region (E_B=240-540 meV).

In order to confirm whether the experimental result of the bulk band .We have performed *ab-initio* calculations using the VASP code. The theoretical $k_{\parallel}$ projected bulk band structure calculated with experimental lattice pa-
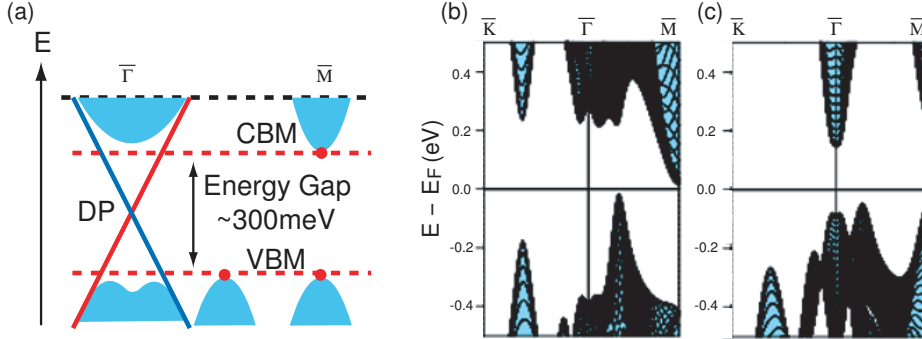
Figure 5.11: (a) The schematic energy dispersions of the surface state and bulk state of TlBiSe$_2$ derived from the experimental results. Theoretical projected bulk band structure of TlBiSe$_2$ obtained with ideal atomic position (b) and with fully optimized geometry (c). Lines show constant k_z contours. Adapted from reference [79]

rameters and ideal rhombohedral atomic positions is shown in Fig. 5.11(b), and the result for with optimized geometry in Fig. 5.11 (c). The geometry optimization was performed within the generalized gradient approximation (GGA) of the density functional formalism. The band structure is seen to be extremely sensitive to small changes in geometry. Especially, it strongly depends on the Se atom position: the optimization of this parameter leads to dramatic changes in the gap region over the whole SBZ; in particular, it widens the indirect gap in the $\overline{\Gamma}$-$\overline{M}$ line between $k_\parallel = 0.3$ $\mathring{A}^{-1}$ and $\overline{M}$ point and brings it close to the experimental value. At the same time, the relative locations of the BCB minima at $\overline{\Gamma}$ and at $\overline{M}$ points depend on the unit cell volume (which is known to be slightly overestimated in GGA). With the fully optimized lattice the BCB minimum is at $\overline{\Gamma}$ point (slightly below the minimum at $\overline{M}$ point), whereas with the experimental lattice parameters and fixed optimized fractional coordinates of the atoms the minimum is at $\overline{M}$ point. Thus, exact knowledge of atomic positions is absolutely necessary to reproduce the experimentally observed bulk features. We have also performed calculations of surface electronic structure in slab geometry with relaxation of outermost atomic layers for Se, Tl, and Bi terminations of the surface (35-41 atomic layers). On all the surfaces, we observe both the Dirac cone and the localized trivial surface states in the gap similar to those shown in [78] for TlSbTe$_2$. They have different character and different dispersion depending on the termination, and in all cases these states are well separated

from bulk bands. Our experiment, however, unambiguously rules out the presence of such states on the studied surface. The reason for that remains an open question.

5.3 Experimental Verification of PbBi$_2$Te$_4$ as a 3D topological insulator

5.3.1 Lead based ternary chalcogenides
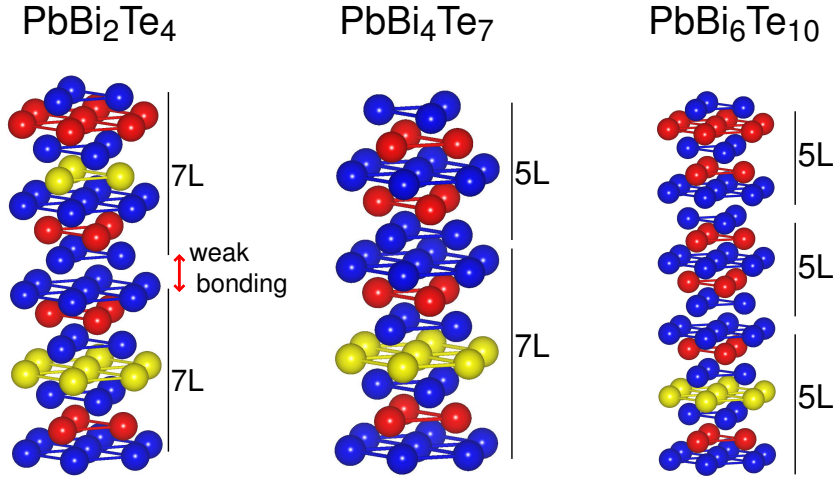
Figure 5.12: Crystal structure of the Pb-based ternary chalcogenides. (a) PbBi$_2$Te$_4$ (b) PbBi$_4$Te$_7$ (c) PbBi$_6$Te$_{10}$.

Some of the Pb-based ternary chalcogenides have been proposed as the 3D topological insulators which has a wide variety of mixed-layer crystal structure than the tetradymite topological insulators as shown in Fig. 5.12 [82]. All these systems have tetradymite-like layered structures but with distinct many layered slabs stacked along the c axis of the hexagonal unit cell. The bonding within the slabs is ionic-covalent, whereas the slabs are linked by weak van-der-Waals forces. The structure of PbBi$_2$Te$_4$ contains septuple layer (7L) slabs (a), whereas the rest of compounds in this series are formed by combining 5L and 7L building blocks (b) and (c) [75, 83]. In this section, we will focus on PbBi$_2$Te$_4$ forming the most fundamental structure unit among them. This material is composed of seven-layer (7L) blocks formed by the atomic layer sequence Te-Bi-Te-Pb-Te-Bi-Te as shown in Fig. 5.12(a). The theoretical analysis with an inclusion of spin-orbit coupling indicates that this compound is a three-dimensional topological insulator.
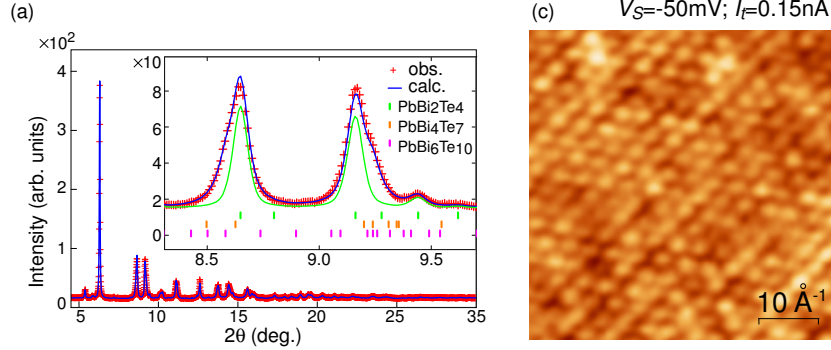
Figure 5.13: (a) Measured x-ray powder-diffraction pattern (+) and result of simulation (solid line) using Rietveld technique. (b) Scanning tunneling microscopy image acquired at a sample bias of -50 mV.

5.3.2 Experimental set-up

A single crystalline sample of PbBi$_2$Te$_4$ was grown by the standard procedure using Bridgman method [83]. Stoichiometric mixtures of Pb(5N), Bi(5N) and Te(5N) were melted in evacuated quartz ampules at 820 °C for a day and then slowly cooled down to 100 °C. Here, we summarize the procedure to prepare a single crystal of the PbBi$_2$Te$_4$ as follow:

(1) Cleaning high-purity Pb, Bi and Te elements with nitric acid (1N) and acetone for 5 minutes, respectively.

(3) Enclosing these elements in the evacuated quartz ampules below 5×10^{-7} Torr.

(4) Heating ampules in Bridgman furnace and gradually cooling under the temperature program as described in Fig. 5.3.

The sample quality was checked by high-precision synchrotron radiation powder diffraction experiments using the Large Debye-Scherrer Camera installed at SPring-8 BL02B2. The high-energy incident beam of 35 keV (wavelength 0.35368(3) Å) was used to reduce absorption by heavy atoms in the samples. The obtained diffraction pattern is mainly explained for PbBi$_2$Te$_4$ but the complete fit can be obtained by taking into account other small phases of PbBi$_4$Te$_7$ and PbBi$_6$Te$_{10}$ (see Fig. 5.13(a)). The molar ratios of these three materials in the sample powder were estimated to be 69:22:9 by adopting the Rietveld technique to the $d¿0.68$ Å data by using the reported structure

parameters. The samples were cleaved along the basal plane and cut into the size of $1.5 \times 1.5 \times 0.5$ mm^3 for the ARPES measurement. The cleaved surface plane clearly shows an atomically well-defined order with hexagonal lattice in the wide area as demonstrated by the scanning tunneling microscope as shown in Fig. 5.13(b). For ARPES measurement the samples were in situ cleaved along the basal plane. Photoemission experiment was performed with synchrotron radiation at the linear undulator beam line (BL1) and the helical undulator beam line (BL9A) of Hiroshima Synchrotron Radiation Center. The ARPES spectra were acquired at low temperature 17 K. The overall energy and angular resolutions were set to 10-20 meV and 0.3 °C, respectively.

5.3.3   Results and discussion
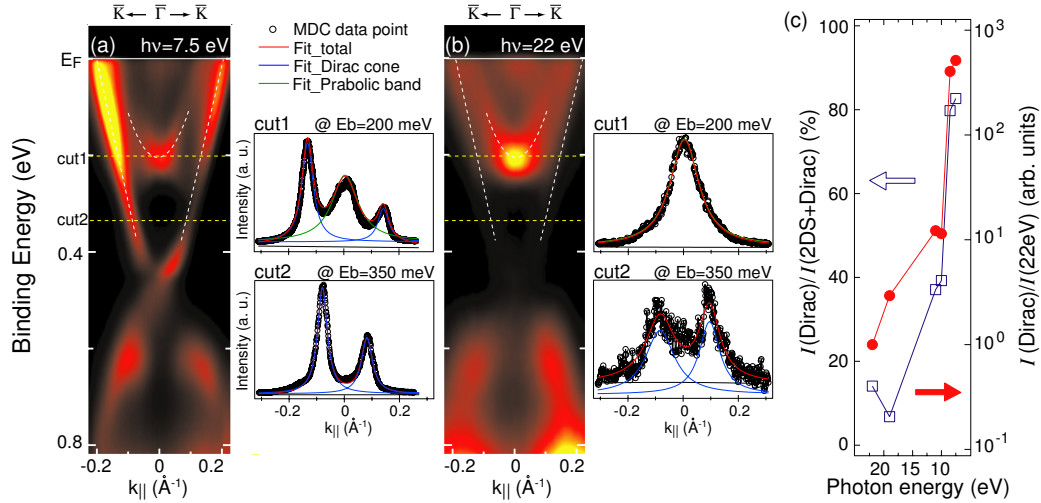
Figure 5.14: (a), (b) ARPES energy dispersion curves along the $\bar{\Gamma}$-$\bar{K}$ line acquired at $h\nu$=7.5 and 22 eV, respectively. In the right panels of (a) and (b) are shown momentum distribution curves (MDCs) at the binding energies of 200 and 350 meV for $h\nu$=7.5 and 22 eV, respectively. (c) Integrated photoemission intensity in the binding energy range 300-400 meV of the Dirac cone with respect to parabolic 2D state I(Dirac))/I(2D state+Dirac) (open square). Also the corresponding intensity normalized to that taken at $h\nu$=22 eV I(Dirac))/I(22eV) is plotted with filled circles.

Figures 5.14(a) and (b) show the ARPES energy dispersion curves along the $\bar{\Gamma}$-$\bar{K}$ line of the surface Brillouin zone measured $h\nu$=7.5 and 22 eV, respectively. First, we see the parabolic band with the energy minima at the binding energy (E_B) of 200 meV, exhibiting a strong photoelectron intensity near the $\bar{\Gamma}$ point for both excitation energies. The position of energy minima are unchanged regardless of different incident photon energy as seen in Fig. 5.14(a) and (b), which confirms the two-dimensional nature of this electronic state. More importantly, a linearly dispersive feature, i.e. the Dirac cone with a crossing point at E_B=470 meV is observed and it is pronounced when excited at $h\nu$=7.5 eV, while it is quite weak at $h\nu$=22 eV. As the incident photon energy increases, the Dirac cone intensities are suppressed with respect to the parabolic band structure around $k_{\parallel}$=0 Å^{-1}. In the right panels of Fig. 5.14(a) and (b) are shown momentum distribution curves (MDCs) at the E_B of 200 and 350 meV for $h\nu$=7.5 and 22 eV, respectively. There is a single contribution from the surface Dirac cone at E_B=350 meV, where only two Lorentzian functions are used for the fit, whereas one more function is needed at E_B=200 meV to describe the additional 2D state. Here, we have tried to extract the photoelectron intensities of the Dirac cone and the 2D state separately from these MDCs by fitting them with the following Lorentzian function

The integrated photoemission intensity in the E_B region of 300-400 meV normalized to that taken at $h\nu$=22 eV, where only the Dirac cone exists, is plotted as a function of the incident photon energy in Fig. 5.14(c). It is apparent that the ratio of spectral weight from the Dirac cone with respect to the parabolic 2D band defined as r=$\frac{I(Dirac)}{I(2DS+Dirac)}$ steeply increases below $h\nu$=10 eV. This unusual photon energy dependence could be explained by matrix-element effects in photoemission.

Figures 5.15(b) and (c) summarize the constant energy contours (i) and their second derivatives (ii) in the $k_{\parallel}$ range -0.3 Å^{-1} $\leq k_x$, $k_y \geq$ +0.3 Å^{-1} from E_B=470 meV (DP) to 0 meV(E_F) at $h\nu$=7.5 and 10 eV, respectively. With $h\nu$=10 eV we find at the DP energy six ellipses oriented along$\bar{\Gamma}$-$\bar{M}$ in addition to the point-like feature at the $\bar{\Gamma}$ point for the TSS. On the other hand, the elliptical contours are much weaker at $h\nu$=7.5 eV, signifying a strong matrix elements effect. In going away from the DP, the sole hexagonally shaped contour is observed down to E_B=290 meV and at smaller binding energies another state becomes enclosed inside the DC (starting with E_B=260 meV). Figures 5.16(a) and (b) show ARPES energy dispersion curves along $\bar{\Gamma}$-$\bar{M}$ line acquired at $h\nu$=7.5 and 10 eV, respectively. The corresponding energy
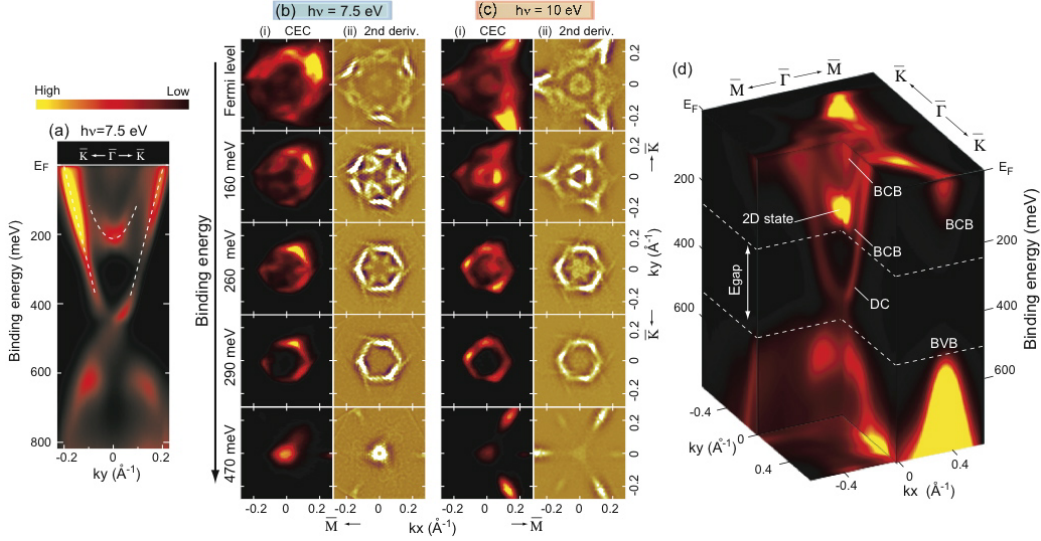
Figure 5.15: (a) ARPES energy dispersion curves along the $\bar{\Gamma}$-$\bar{K}$ line acquired at $h\nu$=7.5 eV. Constant energy contour (CEC) maps (i) and their second derivatives (ii) obtained from the ARPES measurement at $h\nu$=7.5 eV (b) and 10 eV (c) in the $k_{\parallel}$ range -0.3 $\mathring{A}^{-1} \leq k_x$, $k_y \geq$ +0.3 $\mathring{A}^{-1}$ from E_B=470 meV (Dirac point) to 0 meV (Fermi level). The threefold symmetrization procedure is applied only for the second derivative images. (c) Three-dimensional map for $h\nu$=10 eV with Dirac cone (DC) surface state, two-dimensional parabolic band (2D state), bulk conduction band (BCB) and valance band (BVB). The BCB bottom and BVB maximum separated by a bulk energy gap (E_{gap}) are denoted with dashed lines. Adapted from reference [84].

dispersion curves (EDCs) are also depicted on the right side of each panel. First, let us take a look at the bulk conduction band enclosed within the Dirac cone as denoted with the rectangular frame A. At $h\nu$=7.5 eV, we can see two small electron pockets near E_F as schematically shown in the upper part of Fig. 5.16(c). On the other hand, there is a single electron pocket for $h\nu$=10 eV as schematically shown in the lower part of Fig. 5.16(c). One can also see another bulk band feature that shows a downward dispersion in the frame B for $h\nu$=7.5 eV. These differences on incident photon energy can be explained by k_z dependence of the bulk electronic states instead of the matrix element effect. As seen in Fig. 5.15(b) and (c) the TSS further deforms and practically merges into the BCB below E_B=160 meV. In the map measured
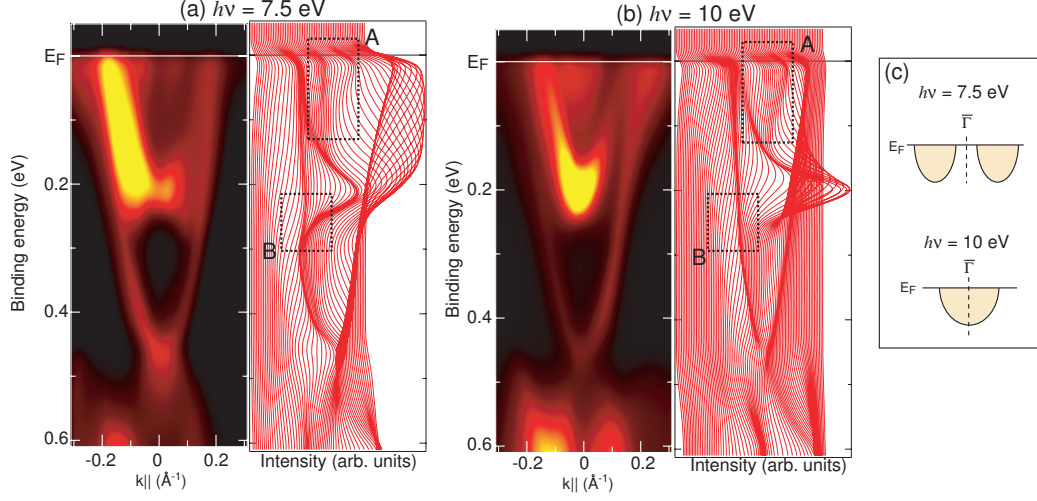
Figure 5.16: ARPES energy dispersion curves along $\bar{\Gamma}$-$\bar{M}$ line acquired at (a) $h\nu$=7.5 and (b) 10 eV, respectively. The corresponding energy dispersion curves (EDCs) are also depicted on the right side of each panel.

with $h\nu$=10 eV the hexagonal FS of the TSS encloses two large and one small triangular shaped surfaces centered at $\bar{\Gamma}$. At $h\nu$=7.5 eV the shape of the inner Fermi surfaces strongly changes and becomes very complicated, which is consistent with a bulk state. The size of the energy gap is estimated as 230 meV as shown in the 3D map for $h\nu$=10 eV (Fig. 5.15(d)). Such a large energy gap is beneficial for a high stability of the spin current conductance at room temperature. Figure 1(d) illustrates a high anisotropy of the BVB: the valence band maximum in the $\bar{\Gamma}$-$\bar{M}$ line is at E_B=490 meV ($k_\parallel$±0.3 $\mathring{A}^{-1}$), while in the $\bar{\Gamma}$-$\bar{K}$ line it is deeper in energy.

Next we discuss the surface Dirac cone of PbBi₂Te₄ in more detail by comparing it with other 3D TIs studied. The Dirac cone dispersion along $\bar{\Gamma}$-$\bar{K}$ is shown in Fig. 5.17(a) for PbBi₂Te₄ and for the well-studied TIs Bi₂Se₃ (Chap. 4.2) and TlBiSe₂ (Sec. 5.1). Close to E_F the Dirac cone energy dispersion in PbBi₂Te₄ is as steep as in the other materials, but it is apparently less steep near the Dirac point. In PbBi₂Te₄, the group velocity at E_F is estimated as 3.9×10⁵ m/s, while near the Dirac point, it is much lower (1.4×10⁵ m/s) than in Bi₂Se₃ (2.9×10⁵ m/s) and in TlBiSe₂ (3.9×10⁵ m/s). The sizes of the iso-energy contours in the bulk energy gap from the Dirac point to 200 meV are much larger for PbBi₂Te₄ than for the other two ma-

125
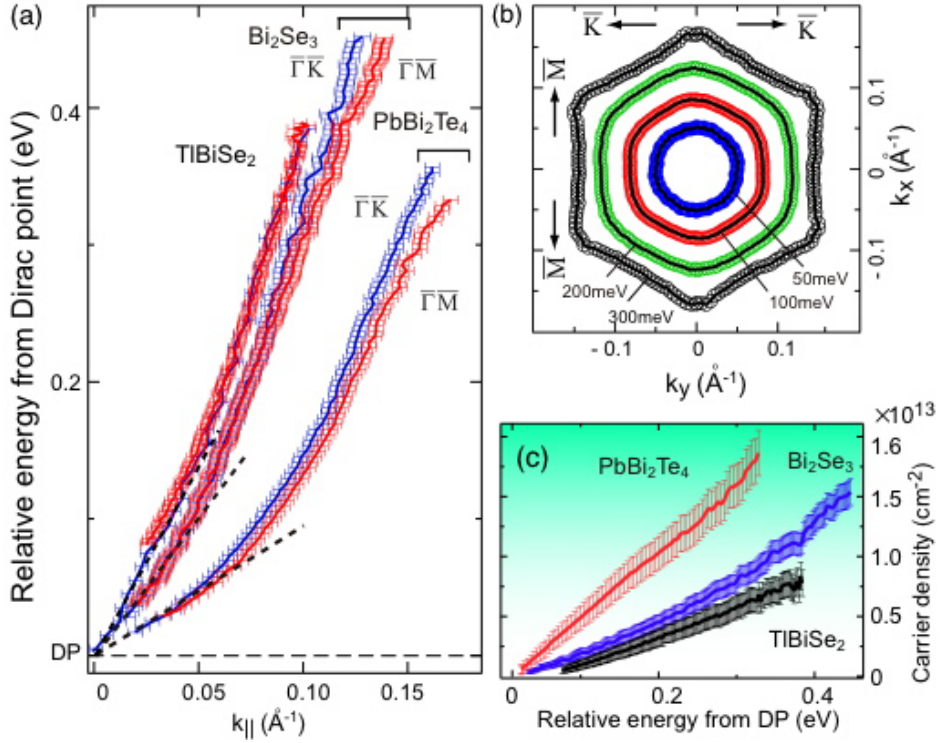
Figure 5.17: (a) Experimental energy dispersion curves of surface Dirac cones along $\bar{\Gamma}$-$\bar{M}$ and $\bar{\Gamma}$-$\bar{K}$ lines in $PbBi_2Te_4$ compared to Bi_2Se_3 and $TlBiSe_2$. The curves are obtained from the intensity maxima of momentum distribution curves. The energy is relative to the Dirac point (DP). (b) Constant energy contours for $PbBi_2Te_4$. (c) Estimated carrier densities $S(E)/4\pi^2$ for three materials as a function of energy with respect to DP. $S(E)/4\pi^2$ is the area of the constant energy contour at energy E. Adapted from reference [84].

terials, as shown in Fig. 5.17(b). The estimated topological surface carrier density in $PbBi_2Te_4$ obtained from the area of constant energy contour $S(E)/4\pi^2$=4.2 is much larger than in the other two materials (Fig. 5.17(c)).

The theoretical bulk and surface band structures of $PbBi_2Te_4$ are shown in Figs. 5.18(a) and (b), respectively. The calculations were performed with the VASP code with optimized internal lattice parameters [85, 86]. In principle, three-dimensional materials with inversion symmetry are classified with four Z_2 topological invariants μ_0; ($\mu_1\mu_2\mu_3$), which can be determined by the parity $\xi_m(\Gamma_i)$ of occupied bands at eight time-reversal invariant momenta

126
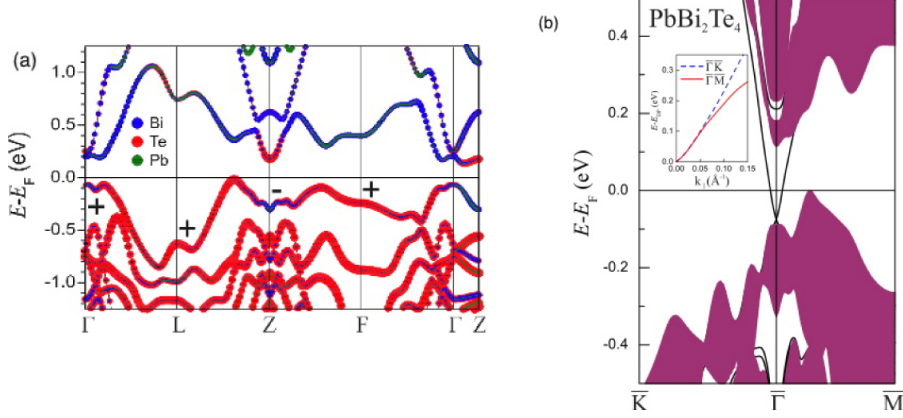
Figure 5.18: (a) Bulk band structure of PbBi$_2$Te$_4$ calculated along high symmetry directions of the Brillouin zone; colors show the weight of the states at Bi (blue), Te (red), and Pb (green) atoms, respectively. Signs of $\delta_i = \pm 1$ at the TRIM are also shown. (b) Calculated surface (solid line) and bulk continuum states (shaded) of PbBi$_2$Te$_4$ along $\bar{K}$-$\bar{\Gamma}$-$\bar{M}$ line. The inset shows the surface Dirac cones in the limited momentum space for $\bar{\Gamma}$-$\bar{M}$ and $\bar{\Gamma}$-$\bar{K}$ lines. Adapted from reference [84].

(TRIM) $\Gamma_{i=(n_1;n_2;n_3)} = (n_1 b_1 + n_2 b_2 + n_3 b_3)/2$, where b_1, b_2, b_3 are primitive reciprocal lattice vectors, and $n_j = 0$ or 1. The Z_2 invariants are determined by the equations $(-1)^{\mu_0} = \Pi_{i=1}^8 \delta_i$ and $(-1)^{\mu_k} = \Pi_{n_k=1;n_{j\neq k}=0,1} \delta_{i=(n_1 n_2 n_3)}$, where $\delta_i = \Pi_{m=1}^N \xi_{2m}(\Gamma_i)$ [16]. For rhombohedral lattice of PbBi$_2$Te$_4$ the TRIMs are Γ, Z, and three equivalent L as well as F points. The previous study confirmed that this compound is a strong topological insulator with the principal topological invariant $mu_0 = 1$ [75]. Here we analyze the $(n_1 n_2 n_3)$ invariants. Interestingly, the parity inversion of bulk bands occurs at the Z point for PbBi$_2$Te$_4$ (Fig. 5.18(a)), which leads to Z_2 invariants 1;(111). This is in contrast to the case of binary chalcogenides Bi$_2$X$_3$ (X: Se, Te), where the parity inversion takes place at the Γ point with Z_2 invariant 1; (000). Note that PbBi$_2$Te$_4$ is the first case among the experimentally established topological insulators with Z_2 invariant 1;(111) possessing a single Dirac cone surface state. It is, thus, distinguished from the Bi$_{1-x}$Sb$_x$ alloy with the same Z_2 invariant [18] but with 5 or 3 pairs of surface states crossing the Fermi energy [19]. In Bi$_{1-x}$Sb$_x$, owing to nonzero invariants $(n_1 n_2 n_3)$, a one-dimensional (1D) topologically protected state can exist at the dislocation core [87]. In the case of the layered crystal, the bulk dislocations can hardly

exist, but other types of 1D TI states, such as edge states in thin films or 1D states at step edges, are possible.

Finally, we compare the experimental ARPES results with the theoretical band structures, see Fig. 5.18(b). The calculated band structure well reproduces the BCB minimum located at Γ point at 200 meV above the Dirac point. Although the BVB maximum is higher in theory than in experiment, the theory well reproduces its location in k-space, that is, it appears around $1/3\bar{\Gamma}\bar{M}$ ($k_{||} \sim 0.3$ $\mathring{A}$). Anisotropic features along different symmetry lines can be recognized above 100 meV relative to the Dirac point, as depicted in the inset. In addition, the parabolic surface state appears at ~ 280 meV above the Dirac point in the conduction band gap, which is consistent with the present observation.

5.4   Conclusion

Our ARPES experiments demonstrated that ternary chalcogenides, $TlBiSe_2$ and $PbBi_2Te_4$, are three-dimensional topological insulators and posses nontrivial surface state. For $TlBiSe_2$, the TSS features in a practically ideal Dirac cone and its velocity is larger than for Bi_2Se_3. Furthermore, according to both experiment and theory, there are no bulk continuum states that energetically overlap with the DP. This means that the scattering channel from the TSS to the bulk continuum is suppressed. Finally, the bulk energy band gap is estimated to be ~ 300 meV, which is comparable to that for Bi_2Se_3. Our experimental results favor the realization of the topological spin-polarized transport with high mobility and long spin lifetime in $TlBiSe_2$. For $PbBi_2Te_4$, the energy gap of 230 meV. Importantly, the size of the Fermi surface contour in the bulk energy gap is significantly larger than in the other presently known 3D topological insulators, whereby the highest carrier density of the known TSSs is achieved. These novel findings pave a way for the efficient control of the group velocity with sufficiently large spin current density by tuning the chemical potential in the bulk energy gap.

Chapter 6

Bulk carrier manipulation of ideal topological insulator TlBiSe$_2$ in reversible spin current regime

6.1   Introduction
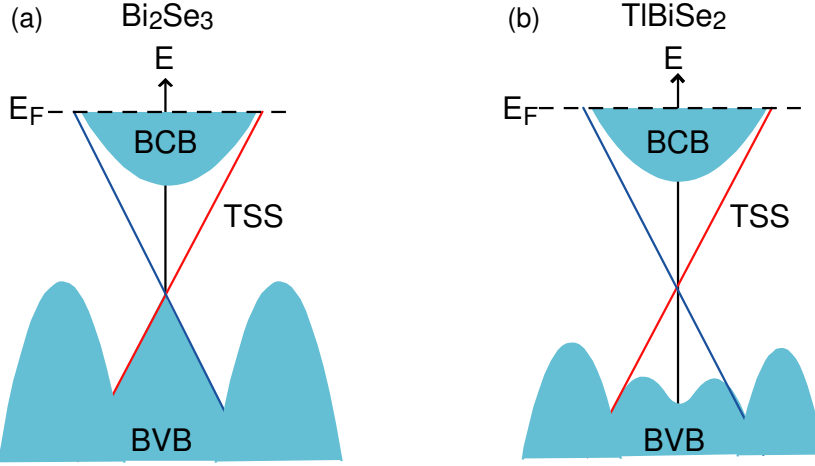
Figure 6.1: Schematic energy band structure images for (a) Bi$_2$Se$_3$ and (B) TlBiSe$_2$, where shaded areas indicate bulk continuum states including the bulk conduction band (BCB) and valence band (BVB) with a topological surface state (TSS). Their characteristic energy dispersion has been determined in previous works.

Band structures near the Dirac point (DP) are quite important because the novel topological surface state (TSS) has great potential to bring several electromagnetic topological phenomena into reality when the DP is located near the Fermi energy (E_F) within the bulk energy gap [60, 61, 62].

Spin-helical textures were clearly identified above the DP in tetradymite compounds, such as Bi$_2$Se$_3$ and Bi$_2$Te$_3$, but the relevant feature was obscured below it [26, 71]. This probably stems from their particular band structures, in which the lower part of the TSS (LP-TSS) is buried in the bulk valence band (BVB), as is actually observed in the ARPES spectra (Fig. 6.1(a)). Indeed, large bulk conduction mainly contributes to the transport in these materials.

As we demonstrated Sec. 5.2, a single TSS has been experimentally verified at the surface of TlBiSe$_2$ and it has the size of the bulk energy band gap, which is estimated to be 300 meV, comparable to that of Bi$_2$Se$_3$. Furthermore, as shown in Fig. 6.1(b), the DP of the TSS has been found to be energetically well isolated from the bulk continuum state, which is missing

in Bi_2Se_3. Owing to the in-gap DP feature, the spin-helical texture was identified not only for the upper part of TSS (UP-TSS) but also for the LP-TSS in a previous SARPES study [88]. In addition to these talented electronic structures, a massive TSS has been observed in this system even if time reversal symmetry is preserved without any magnetic dopants [88, 89]. The occurrence of these features at the surface of $TlBiSe_2$ motivates us to further explore this surface to possibly realize macroscopic topological phenomena. However, despite the potential advantages of $TlBiSe_2$, the study of macroscopic properties of this material is hindered by the uncontrolled bulk current due to spontaneous electron doping effects. These difficulties prevent us from investigating topological phenomena and thus the production of a bulk-insulating phase in this material is quite important. Also, theoretical and experimental investigations on spin polarizations of a TSS indicate that final state effects play a role, that is, the observed spin-helical state is sensitive to the incident light polarization and experimental geometry [90]. Therefore, to evaluate the spin-helical TSS more accurately, SARPES measurements with variable light polarizations and photon energies are required

Here, we show how to control the bulk carrier density in $TlBiSe_2$ and bring the material into the bulk-insulating regime. Spin polarizations of a TSS that reverse their signs at the DP have been revealed by a SARPES measurement combined with variable light polarizations and photon energies, which confirms that the novel spin texture is present at the surface. Using chemical composition analysis, we noticed that several kinds of defects contribute to a spontaneous electron doping effect. On the basis of this result, we synthesized a high-quality crystal of $Tl_{1-x}Bi_{1+x}Se_{2-\delta}$, which enables us to obtain the bulk-insulating phase and tune the DP near E_F. Our key finding, that the ideal topological insulating phase can be achieved without any guest atoms, unambiguously offers a platform for a wide range of technical applications.

6.2 Experimental set-up

Single crystals of $Tl_{1-x}Bi_{1+x}Se_{2-\delta}$ (x=0.015-0.064) were grown by a standard procedure using Bridgman method with high purity elements (Bi, Se; 5N, Tl; 5N). The quality of all samples was checked with Laue diffraction, X-ray diffraction as well as electron probe micro-analysis (EPMA). The carrier-type of samples was evaluated from the measurement of Seebeck coefficients. Af-

ter all the above-mentioned procedures were completed, a part of ingot was cut into a suitable size of $2 \times 2 \times 0.5$ mm^3 for the photoemission experiments. The x values were determined by EPMA analysis. Angle-resolved photoemission spectroscopy (ARPES) and spin- and angle-resolved photoemission spectroscopy (SARPES) experiments were performed with synchrotron radiation at the ESPRESSO end station (BL9B) and the high-resolution ARPES endstation (BL9A) of HiSOR. Each photoemission spectrum was acquired with the hemispherical photoelectron analyzer (VG-SCIENTA R4000) at 40 K for SARPES measurement and at 80 K for ARPES. The energy and angular resolutions were set below 20 meV and 0.1° for ARPES, and 30 meV and 0.7° for SARPES experiment, respectively. The photon energy ($h\nu$) was tuned at 17.5 eV and 17.7 eV for ARPES and SARPES measurements, respectively. Clean surfaces were obtained by cleaving in ultrahigh vacuum at low temperature. The hard X-ray photoelectron spectroscopy (HAXPES) measurement was performed at SPring-8 BL15XU ($h\nu$=6 keV). The total energy resolution was set to 240 meV. All the HAXPES experiments were performed at room temperature for the same sample sets as used in the ARPES and SARPES experiments without cleaving the samples.

6.3   Results and discussion

Figure 6.2(a) shows the ARPES results from as-grown TlBiSe$_2$ (x=0.064) along the $\bar{\Gamma}$-$\bar{K}$ high symmetry line. An X-shaped Dirac cone energy dispersion is observed and the DP is located at a binding energy (E_B) of 310 meV, which is slightly lower than that reported in previous works, probably because of carrier doping induced by gas absorption after sample cleaving. Here, one can see that the LP-TSS is merged into the M-shaped state at E_B=470 meV, taken as the intensity maxima of the plot indicated by open circles in Fig. 6.2(a). We then extracted the constant energy contours (CECs) near the $\bar{\Gamma}$ point from E_F to E_B=600 meV, as shown in Fig. 6.2(b). As Fig. 6.2(c) shows, at E_F, one finds that the Fermi surface of the TSS is isotropic, in contrast to the situation in Bi$_2$Te$_3$ and Bi$_2$Se$_3$. Here, we note that the TSS can still be clearly identified in Fig. 6.2(d), even below the DP. The absence of an anisotropic feature for both parts of the TSS, the so-called warping effect, may indicate that electron scattering can be suppressed as long as time reversal symmetry is preserved. As E_B increases, the spectral weight of the M-shaped state becomes stronger and a triangular
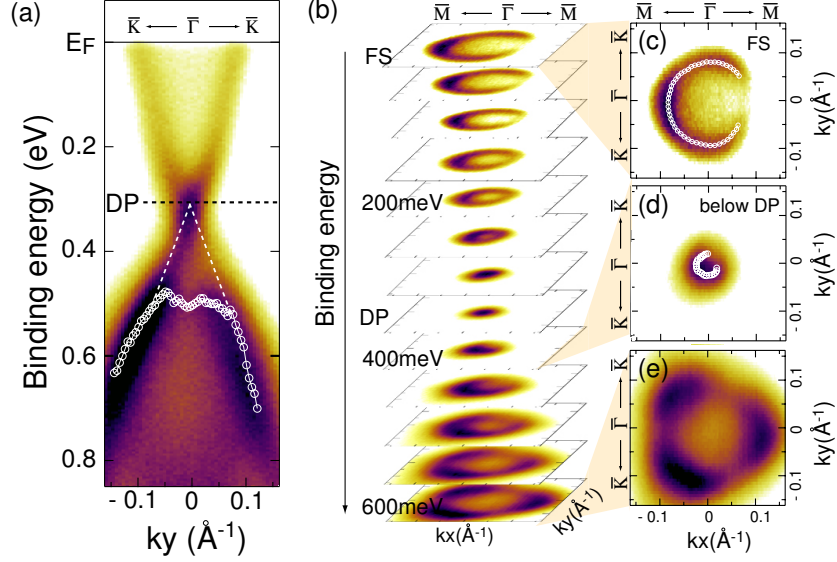
Figure 6.2: (a) ARPES intensity near the E_F for as-grown sample and around $\bar{\Gamma}$ point using a photon energy of 17.7 eV, where the Dirac point (DP) is located around 310 meV and intensity maxima of the M-shaped state from the momentum distribution curves (MDCs) are denoted by circle. (b) Constant energy contour maps at several E_B from E_F to 600 meV in 50 meV step. (c)-(e) Selected constant energy contours at (c) E_F, (d) below the DP (E_B=450 meV) and (e) at E_B=600 meV. Intensity maxima from the momentum distribution curves (MDCs) are denoted by circles in figure (c) and (d).

shaped CEC is gradually formed as clearly seen in Fig. 6.2(e).

In order to determine k positions for the SARPES data, energy distribution curves (EDCs) were taken using a multichannel detector as shown in Figure 6.3(a). Figure 6.3(b) shows spin-integrated EDCs taken with the same angular window as that for the spin-resolved spectra and one notices that it is sufficient to resolve very steep energy-dispersion even with spin-resolution. Here, five bold lines indicate the selected k positions used to obtain the SARPES results shown in Fig. 6.3(c). Figure 6.3(d) shows the spin-resolved EDCs at these emission angles. Here, the spin-up and spin-down spectra are plotted with upright and inverted triangles, respectively. Note that, during the spin-resolved measurement, there was a slight energy shift of the TSS by 20 meV towards E_F, which is ignorable on the energy

133
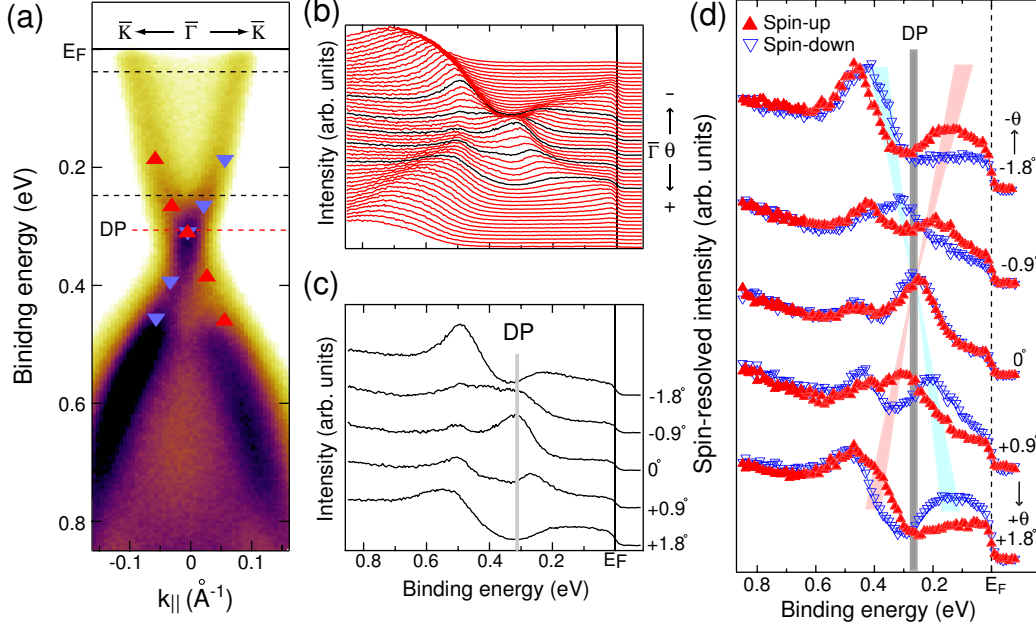
Figure 6.3: (a) ARPES intensity map near the E_F for as-grown sample. Red (blue) triangles shows the intensity maxima of spin-up (-down) state obtained from the SARPES measurement in (d). (b) Energy distribution curves (EDCs) integrated with same angular resolution for SARPES mode. Bold lines indicate the EDCs (b), where SARPES measurements were performed. (c) Spin-resolved EDCs along $\bar{\Gamma}$-$\bar{K}$ from k=-1.8° to +1.8° in 0.9° step. Spin-up and spin-down spectra are plotted with closed upright (filled) and inverted (open) triangles.

scale used for spin- resolved measurement. In the normal emission configuration (θ= 0°), the spin-up and spin-down spectra are identical. At θ= -1.8°, the spin-up state is found to be centered at E_B=150 meV, while the spectral weight of the spin-down state is comparatively flat. In going from θ=-1.8° to +1.8°, the spin-up state shifts to higher E_B with increasing θ. The spin-down feature shows similar behavior, but the direction of the energy shift is opposite. Peak positions determined by spin-resolved EDC for each spin directions are plotted in Fig. 6.3(a).

The measured spin polarizations of the TSS at several emission angles are shown in Fig. 6.4(a). Here, it should be emphasized that the spin polarizations are clearly resolved not only in the UP-TSS, but also in the LP-TSS,
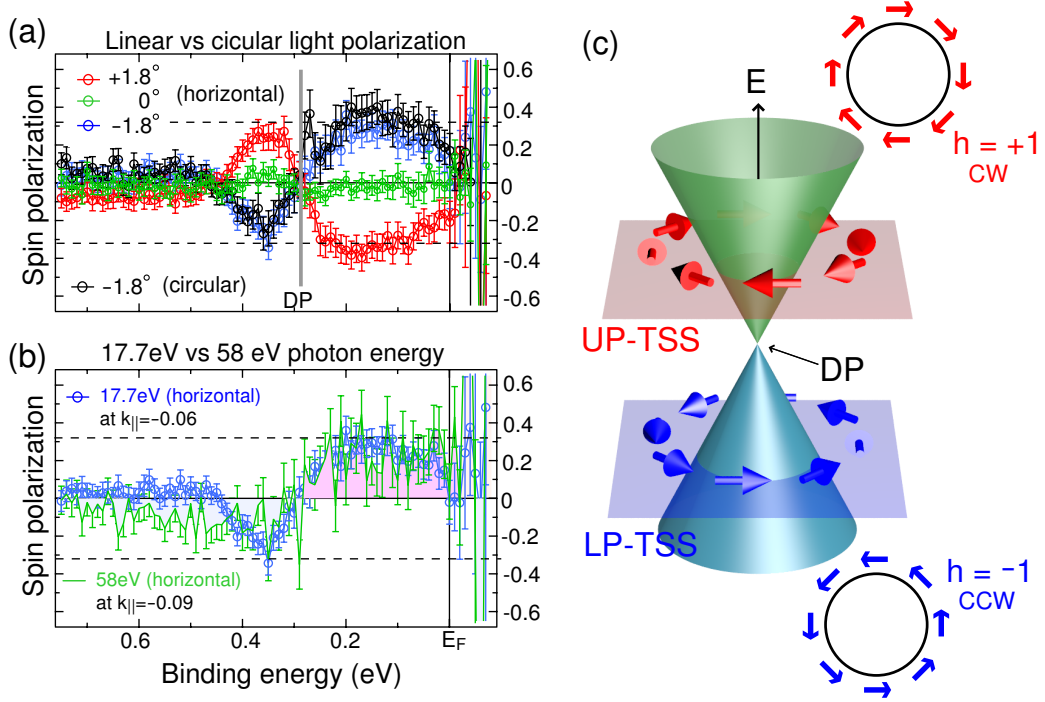
Figure 6.4: (a) Spin polarizations taken with horizontally and circularly polarized lights. Red, blue and green marks indicate the spin polarization obtained by horizontally polarized light at +1.8°, 0° and -1.8°, respectively. Black marks denote that observed by circularly polarized light at -1.8°. (b), A comparison of spin polarizations taken with different photon energies of 58 eV (green marks) and 17.7 eV (blue marks). Solid lines in (a) and (b) denote the size of typical spin polarization 32%. (c) Schematic image of spin helical topological surface state with reversed spin helicity at the Dirac point (DP).

and furthermore, the spin polarizations are inverted with respect to the $\bar{\Gamma}$ point, which is consistent with the previous SARPES work on the same material [88]. To evaluate this reversed spin polarization feature, the spin-resolved measurement has also been performed with circularly polarized light. The observed spin polarization with circularly polarized light at $-1.8°$ shows the same feature as that seen for linear polarization in Fig. 6.4(b). Moreover, this feature does not strongly depend on $h\nu$. These results signify a helical spin texture in k space, as depicted in Fig. 6.4(c).

Before attempting an effect bulk carrier control, we explored the chemical
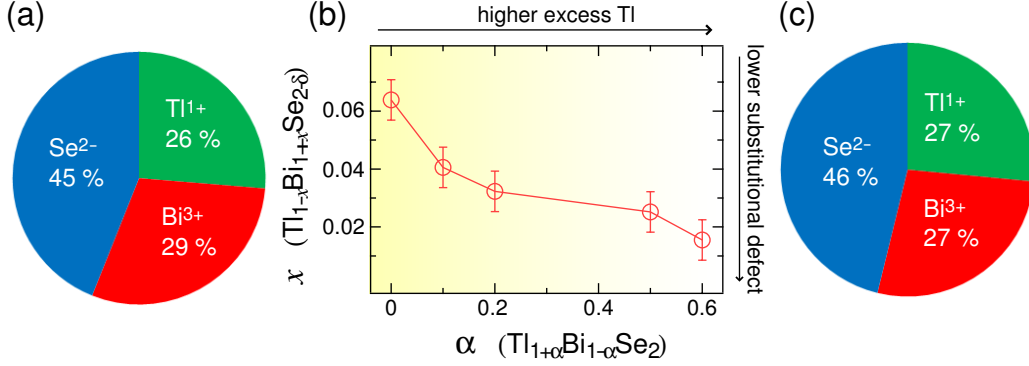
Figure 6.5: (a) Result of chemical composition analysis for as-grown sample. (b) Evaluated x values versus α values. (c) Result of chemical composition analysis for excess thallium sample ($\alpha=0.6$).

composition of an as-grown sample with EPMA to understand the origin of the spontaneous electron doping effect, and found that the as-grown sample was non-stoichiometric. This result indicates the occurrence of several kinds of defects. Accordingly, we have synthesized crystalline $Tl_{1-x}Bi_{1+x}Se_{2-\delta}$ while manipulating atomic compositions, where x and δ indicate the value of substitution in cation and anion-site defects, respectively. In this work, we have focused on control of x values.

In order to understand the origin of spontaneous electron doping effect for the as-grown sample of TlBiSe$_2$, EPMA analysis has been conducted at N-BARD in Hiroshima University (JEOL JXA-8200). The result for the as-grown sample is summarized as a circle graph in Fig. 6.5(a). It is noticed that the estimated compositions deviate from the stoichiometric values, that is, (i) the Se concentration is less than 50% and (ii) the ratio of Tl concentration to that of Bi is less than unity. First, the item (i) tells us that the chalcogen-site vacancies are present in the synthesized sample, and a portion of Tl and Bi ions may also be substituted at chalcogen sites (anti-site defects). The chalcogen vacancies often take place in chalcogenide systems that act as donors while the anti-site defects behave as accepters. Note that, anti-site defects could be a minor effect because the electronegativities of Tl and Bi are smaller than that of Se. The item (ii) has never been reported so far for TlBiSe$_2$, which might be considered to stem from substitutional-type defects at cation sites, where a small portion of Tl^{1+} sites are replaced by Bi^{3+}. By

taking into account the number of valence electrons of both ions, one can easily find that this type of defect works as an electron donor as expressed with the following equation:

$$Bi + Tl^{1+} = Bi^{3+} + Tl + 2e^- \qquad (6.1)$$
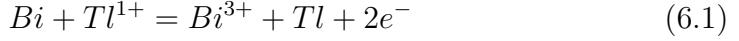
Therefore, we need to describe the actual chemical composition of samples as $Tl_{1-x}Bi_{1+x}Se_{2-\delta}$, where x and δ denote the amount of cation-site defects and anion-site defects, respectively. In order to conduct hole-doping in $TlBiSe_2$, it is necessary to reduce x down to nearly a stoichiometric value. In this work, we have tried to reduce the substitutional defects at the cation-sites by introducing excess Tl as an initial composition $Tl_{1+\alpha}Bi_{1-\alpha}Se_2$, where α denotes the amount of excess Tl atoms and the amount of Se is fixed in the sample growth procedure. Figure 6.5(b) shows the x values determined by the EPMA analysis as a function of α, where the error bars come from the statistical error in the EPMA analysis at several parts of the sample. Here, one can find that x decreases with increasing α. At α=0.6, the Bi/Tl ratio is close to unity as shown in Fig. 6.5(c). It is thus shown that a nearly stoichiometric composition can be achieved.

The evolution of TSS for several different x's is shown in Fig. 6.6(a)-(d). Taking the DP energy position as a reference, the E_F shifts downwards by 100 meV at x=0.032 with respect to that for an as-grown sample (x=0.064). At lower x values, the sample goes into a bulk insulator phase, where the E_F is located inside the bulk energy gap, and the DP is still present below E_F. At x=0.015, the E_F undergoes a further downward shift and the DP is pushed above E_F with reversed spin helicity. To quantitatively evaluate the E_F shift of the TSS as a function of x, the shape of TSS band dispersions need to be compared among various samples with different x's. Figure 6.6(e) shows the result of peak plots obtained from energy distribution curves (EDCs) and momentum distribution curves (MDCs). Here, the observed energy shift is found to roughly follow a rigid band-like picture, since TSSs with different x's are identical to each other when their energy positions are plotted with respect to the DP energy, despite a total energy shift as large as $\sim$0.4 eV. Figure 6.6(f) shows the EDC at the center of the surface Brillouin zone for x= 0.032. Note that the EDC is composed of a single peak at the DP that can be reproduced well with a single Lorentzian peak, which indicates that there is no gap and the TSS still remains even after a drastic change of compositions, in sharp contrast to the gapped TSS found for $TlBi(Se_{1-x}S_x)_2$. Our results are unique because either guest atom doping [57] or fabrication
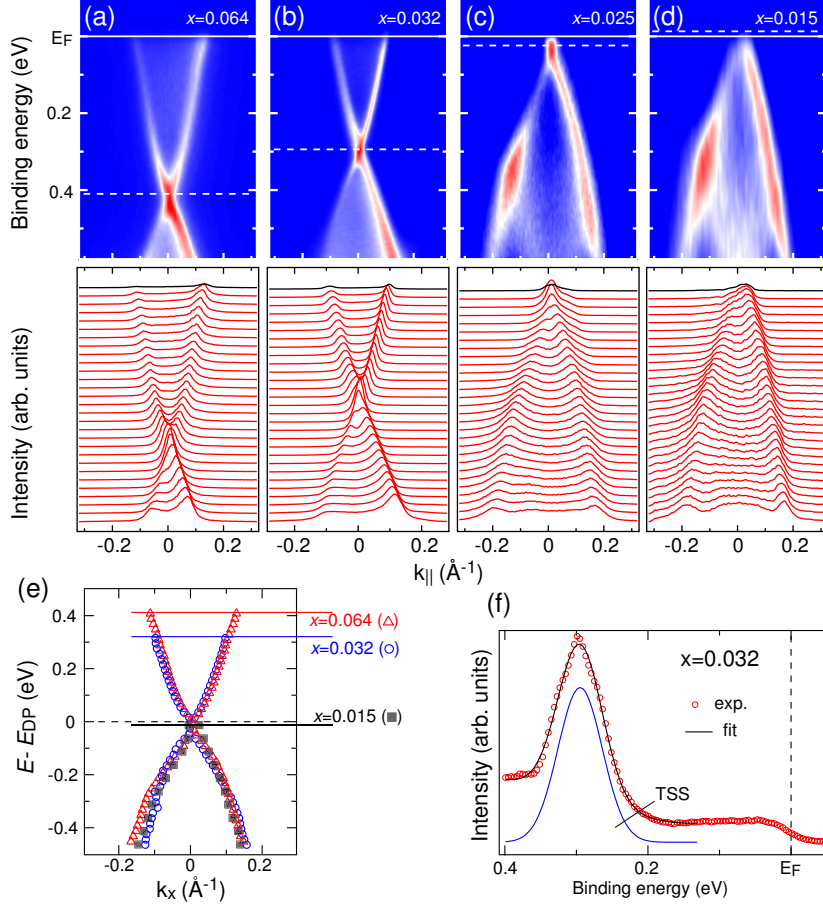
Figure 6.6: (a)-(d) Measured band dispersion and momentum distribution curves (MDCs) for x=0.064-0.015 samples. Top row: image plots of band dispersions along the $\bar{M}$-$\bar{\Gamma}$-$\bar{M}$ direction obtained with $h\nu$=17.7 eV. Bottom row: MDCs from image plots shown in Top row. (e) Plot of energy peak position determined by the MDCs and energy distribution curves (EDCs) fitting analysis with respect to the Dirac point energy. (e) EDC for x=0.032 sample at the central $k_{\parallel}$ position with fitting result.

of multinary compounds [91] is usually required to control bulk carriers for naturally n-doped TIs. However, these methods might lead to considerable lattice disorder that can disturb electron transport, thus substantially reducing the carrier mobility. Our methodology, which avoids these techniques,

provides a path to a new style of material design of TIs with extremely high surface electron mobility.
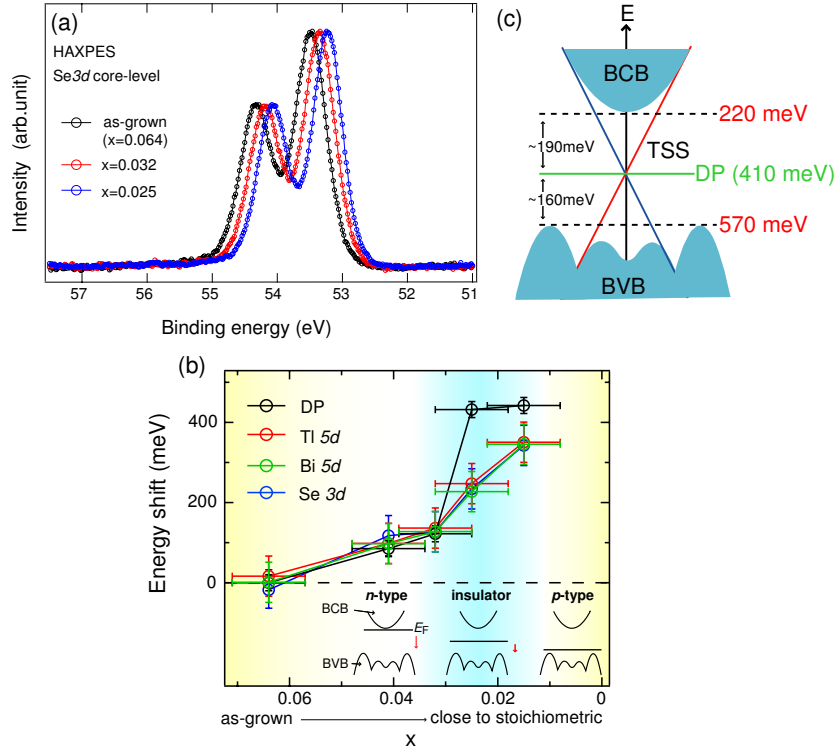
Figure 6.7: (a) Se 3d core-level with spin-orbit splitting for samples with deferent x levels. The sample with x=0.064, 0.032, 0.025 levels are denoted by the black, red and blue open circles and lines. (b) Comparison of x dependence with respect to the as-grown sample of bulk core levels and Dirac point energy (DP) obtained in Fig. 6.6. The chemical energy shifts for Tl 5d, Bi 5d and Se 3d core-level are denoted by red, green and blue colored circles and lines. Inset figures in panel b schematically show the relation between deeper-lying bulk state and chemical potential. (c) Schematics of energy band structure for bulk and surface states around $\bar{\Gamma}$ point revealed in Sec. 5.2.

Finally, in order to experimentally confirm the bulk insulator property of TlBiSe$_2$, a deeply buried bulk state has been investigated by hard x-ray photoelectron spectroscopy (HAXPES) with a photon energy of 5.95 keV, where the mean free path of the photoelectron reaches as large as $\sim$5 nm.

Figure 6.7(a) shows the Se $3d$ core-level spectrum for compounds with different x values, in which the peaks are found around E_B of 52∼55 eV. One can see that the observed peaks energetically shift to lower E_B with decreasing x. Similar energy shifts are also found for the other core-levels. Typical results for Tl $5d$, Bi $5d$ and Se $3d$ core-levels are plotted in Fig. 6.7(b) together with the DP energy shift of the TSS determined by the ARPES measurements shown in Fig. 6.6(a)-(d). One can see that all the bulk core levels show a monotonic energy shift to lower E_B with decreasing x and the maximum energy shift of 330 meV is obtained at the minimum x of this study. This result indicates that all the observed core level shifts are attributable to the chemical potential (E_F) shift caused by bulk hole doping. By referring to our previous ARPES study for the characteristic energy band structure of this material, the bottom of bulk conduction band (BCB) is seen to be located around E_B=220 meV and the relationship between the BCB bottom and the E_F is shown in inset of Fig. 6.7(b). At x=0.042, we notice that the bottom of BCB is pushed up, but still crosses E_F. One can notice that the DP drastically shifts upward by 300 meV in going to lower x, where the bottom of the BCB goes into the bulk energy gap region. The observed difference in the x-dependent energy shift for the bulk and surface might be ascribed to the construction of the band bending effect due to the different bulk insulating level. We should note that the bulk still remains insulating at $x = 0.015$, where the spin helicity at E_F is reversed with respect to those for higher x. This result tells us that the spin helicities of TSS can be switched by tuning the E_F position near the DP while keeping the suppressed bulk conductance and is expected to provide an ideal platform for studying topological magneto-electric effects.

6.4 Conclusion

In conclusion, we have established a methodology to realize a bulk-insulating phase in the ternary topological insulator TlBiSe$_2$. We have found unequivocal evidence for an initial state spin texture that reverses its helicity above and below the DP at the surface using our innovative spin- and angle- resolved photoemission spectrometer. Further, we have found that the natural electron doping for TlBiSe$_2$ is caused not only by anion site defects but is also due to defects at the cation sites. Starting from this disadvantageous situation, we have demonstrated that the DP of the functional TSS can be

manipulated below and above E_F by controlling atomic compositions close to stoichiometric values without introducing any foreign elements, and thus finally achieved a bulk insulator phase. Moreover, our methodology has the advantage of being able to obtain an isolated DP from bulk continuum states, which allows access to both of the helical spin textures without any bulk carrier interruptions. These findings forge a new direction for topological insulators towards realizing an ambipolar gate control with high mobility electrons for future spintronic devices, and also provide an ideal platform to study new exotic phenomena.

Chapter 7

Experimental verification of the surface termination in the topological insulator TlBiSe$_2$ using core-level photoelectron spectroscopy and scanning tunneling microscopy

7.1 Introduction
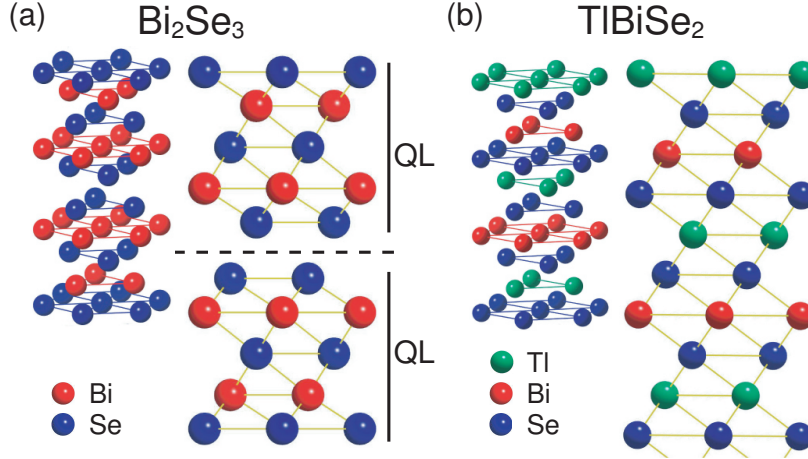
Figure 7.1: Crystal structures of (a) Bi$_2$Se$_3$ and (b) TlBiSe$_2$. (left) Part of the crystal structures where 10 layers are shown. (right) Side view from [100] direction. The crystal structure of Bi$_2$Se$_3$ and TlBiSe$_2$ with the quintuple layers (QLs) stacking in the sequence Se-Bi-Se-Bi-Se and the atomic layer stacking in the sequence -Tl-Se-Bi-Se-Tl- without van-der-Waals-gap. Adapted from reference [92].

So far, several binary chalcogenides, such as Bi$_2$Se$_3$ and Bi$_2$Te$_3$, are known as the prototypical topological insulators. They form a tetradymite crystal structure with a stacking of quintuple layers (QLs) (X-Bi-X-Bi-X atomic layers, X: Se or Te) weakly coupled via van-der-Waals-forces as shown in Fig. 7.1(a). Due to the weak bonds between the QLs, the outermost chalcogenide layer of a QL terminates the surface after cleaving and it is therefore thought that dangling bonds will not emerge. The scenario that layered materials cleave along their van-der-Waals gap is widely accepted [93]. Actually, *ab-initio* calculation [21] with the chalcogenide termination model has reproduced their characteristic electronic structures obtained by angle-resolved photoemission spectroscopy (ARPES) [22, 23].

After finding the tetradymite-type topological insulators, TlBiSe$_2$ has been discovered to be a topological insulator, which forms a three-dimensional crystal structure without van-der-Waals-gaps, as shown in Fig. 7.1(b). The crystal is built up by stacking [-Tl-Se-Bi-Se-]^n layers along the *c*-axis of its hexagonal unit cell. In this compound, the observed TSS features an in-gap

Dirac point which is well isolated from the continuum states of the bulk. This may prove essential for the realization of an ambipolar gate-control in spin-current devices as well as for studying novel topological properties, where the Dirac point is required to be close to the Fermi energy [60, 61, 62]. In this respect, $TlBiSe_2$ is known as one of the most promising topological insulators of today. However, due to the absence of any van-der-Waals-gaps, and the overall covalent and ionic natures of the interatomic bonds, it is unknown which layer terminates the surface after cleaving. A theoretical study predicted that trivial surface states should co-exist with the non-trivial TSS due to dangling bonds at the cleaved surface and even the TSS will be affected by the surface termination [78]. However, no trivial surface states have been observed and the observed band structures of the TSS apparently are the same for previous ARPES measurements. This discrepancy indicates that the actual cleaved surface would be different from the assumed one in the calculation, which is in sharp contrast to the situation for the prototypical topological insulators. Therefore, studying the surface termination is an important key to solve the discrepancy with a precise surface model in $TlBiSe_2$.

In this paper, we present an experimental approach to determine the surface termination of $TlBiSe_2$ by using a combination of scanning tunneling microscopy (STM) and core-level photoelectron spectroscopy (CL-PES). First, we present STM results revealing that residual islands are formed on the cleaved surface. This fact makes a case for a preferential cleaving plane between the Tl and Se layers, leaving a Se surface with the residual Tl atoms forming the islands. This particular situation is strongly supported by employing PES on the core-levels of $TlBiSe_2$ using different surface and bulk sensitive photon energies ($h\nu$s) ranging from vacuum ultraviolet (VUV) to the hard x-ray (HAX) regime.

7.2 Experimental set-up

Single crystalline samples of $TlBiSe_2$ were grown by using the Bridgman method using high purity elements (Bi, Se: 99.999 %, Tl: 99.99 %). The materials were heated in an evacuated quartz ampule above the melting point around 800 °C, and kept at the constant temperature for two days. It was then cooled down to 100 °C over a period of twenty days.

The STM experiment was conducted at 78 K in an ultrahigh vacuum with a base pressure better than 1×10^{-8} Pa using a low temperature scan-

ning tunneling microscope (Omicron Nano Technology). STM images were acquired in the constant-current mode with a bias voltage (V_s) applied to the sample. The samples were cleaved *in-situ* at room temperature and also low temperature below 100 K, and then transferred to the measurement chamber.

Surface sensitive PES in the VUV regime (VUV-PES) was conducted at BL-7 of the Hiroshima Synchrotron Radiation Center with a hemispherical photoelectron analyzer (VG-SCIENTA SES 2002) at 80 K in ultra-high vacuum conditions better than 1×10^{-8} Pa. The excitation energies ranged from 24 to 250 eV. The total energy resolution for the VUV-PES measurement was obtained by Fermi edge fitting of polycrystalline Au and found to be approximately $E/\Delta E = 1000$. The samples were cleaved *in-situ* at 80 K. In order to reduce photoelectron diffraction effect the VUV-PES spectra were recorded at normal emission in angle integrated mode, covering an angular window of ±7 degrees along the $\bar{\Gamma}$-$\bar{\text{M}}$ direction.

Bulk sensitive PES with hard x-ray (HAX-PES) was measured at BL15XU of SPring-8 at room temperature. An excitation energy of $h\nu$=5.95 keV was used, which results in an inelastic mean free-path (IMFP) for the photo-electrons as large as 50 $\mathring{A}$. This corresponds to a probing depth of up to 30 atomic layers for TlBiSe$_2$. The total energy resolution for the HAX-PES measurement was determined to be 246 meV. The samples were cleaved in air and immediately installed into the vacuum chamber.

7.3   Results and discussion

First, the cleaved surface of TlBiSe$_2$ has been directly examined by STM. Figure 7.2(a) shows a typical large area image acquired at a sample bias voltage of V_s=-0.8 V. A couple of step edges are clearly seen in the cleaved plane, whose height profile along A-B is shown in Fig. 7.2(a). The observed terraces have a typical width larger than 20 nm. It can also be seen that their step height is around 8 $\mathring{A}$, which is comparable to the five-layer-thickness (-Tl-Se-Bi-Se-Tl-). The uniform step height strongly indicates that identical atomic layers terminate the different terraces at the cleaved surface. In figure 7.2(c), we show a small area STM image on a single terrace with atomic resolution. It can be clearly seen that the terrace is made up by residual islands on top of the surface layer. It should be noted that one can see the close-packed lattice structure within the islands, which corresponds to the TlBiSe$_2$ (001) surface. These features indicate that the atoms forming the islands remain
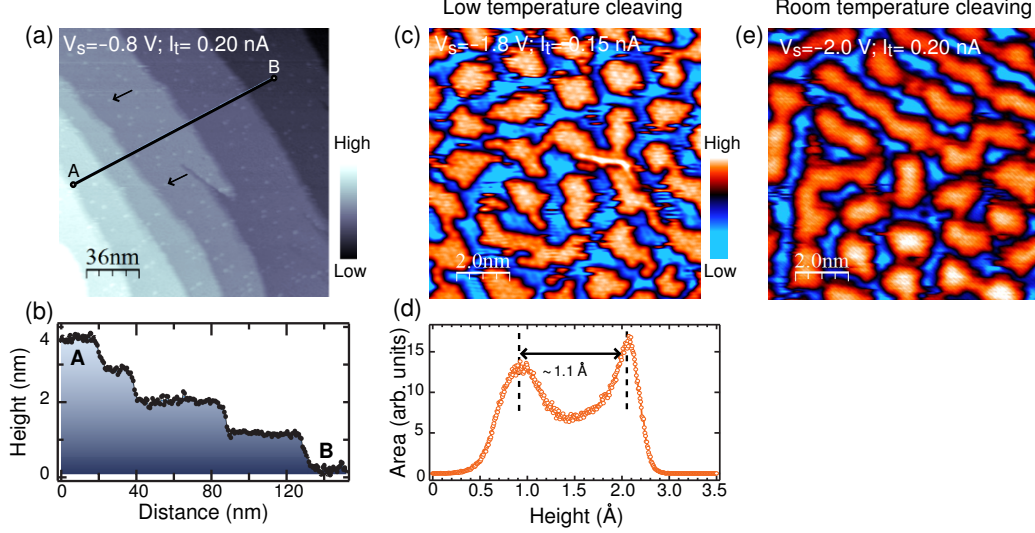
Figure 7.2: (a) Large scale STM image of TlBiSe$_2$; (b) Height profile of the steps on the cleaved surface of TlBiSe$_2$ along the A-B line in (a); (c) Small area of the cleaved surface obtained by low temperature cleaving, showing atomically resolved structure of the residual clusters on the cleaved surface. (d) Histogram of the surface shown in (c). (e) Small area of the cleaved surface obtained by room temperature cleaving. Adapted from reference [92].

on top of the surface layer after the sample is cleaved. Note that the residual islands have been observed also for the surface cleaved at low temperature below 100 K (not shown), which means that the formation of the islands does not depend on the cleaving temperature. It is certainly surprising that a single TSS has been identified by ARPES measurements regardless of the existence of the islands found by the STM. This unambiguously represents the topologically non-trivial character of this surface state.

To qualify the island coverage of the surface, we show that the height distribution of topographic STM image in a histogram in Fig. 2(d), where two peaks can be identified. Note that the height difference between two peaks represents the heights of the island in the topographic image. Besides the area of the each peak represents the area of islands (right peak) and the rest area (left peak), respectively. The height of the islands is found to be 1.1 $\overset{\circ}{A}$, which is smaller than the interlayer distance along the c-axis $\sim$1.8 $\overset{\circ}{A}$ [77]. This difference may indicate the altered local density of states of

147

the islands including an apparent change in height and an inward relaxation of the islands toward the bulk. In both cases, it can be safely concluded that the islands are formed by a single monolayer of atoms. An analysis of the area of the surface and island peaks shows that almost half of the surface is covered by islands. One may notice that bright spots are visible on the terraces (arrows in Fig. 2(a)). By their height, we consider them to be of different surface terminations than the islands. We note however that the occupancy on the terrace is small compared to the islands. Therefore, we can safely disregard their influence on the surface properties.
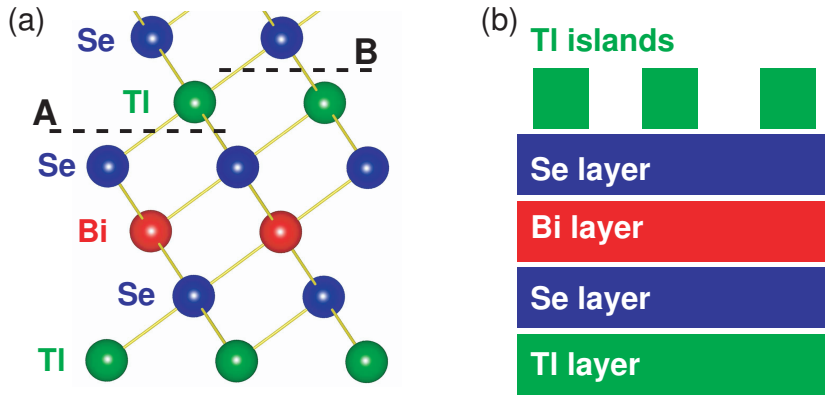
Figure 7.3: (a) Schematic image for the cleaving of TlBiSe$_2$ from the [100] direction. Dashed lines with marked A (B) shows the teared bonding with the lower (upper) Se layer. (b) Proposed cleaved surface model. Adapted from reference [92].

In the crystal structure of TlBiSe$_2$ shown in Fig. 7.1(b), the Tl layers are sandwiched by Se layers. By taking into account the previous *ab-initio* study, which has shown that the bonding strength between Tl and Se layers is weaker than that for the others [78], it can be expected that cleaving would happen between these layers. Note that there are two possibilities for the surface termination as shown in Fig. 7.3(a); the breaking of the bond with the lower Se layer (dashed line A in Fig. 7.3(a)) and the upper layer (dashed line B). In the former case, the Se layer would terminate the surface, whereas the Tl layer will remain on top of the Se layer in the latter case. Since these two possibilities can be considered to be equally likely, we propose a model of the cleaved TlBiSe$_2$ surface as seen in Fig. 7.3(b). The islands on the cleaved surface would then consist of the residual Tl atoms, covering half

the Se layer. Note that the Tl-Se swap model where the surface Tl layer is interchanged with the Se layer, i.e. Se-Tl-Bi-Se-Tl-, has been proposed as another possible way to terminate the surface, but the Tl termination was predicted to be energetically preferred to the swap model [78].
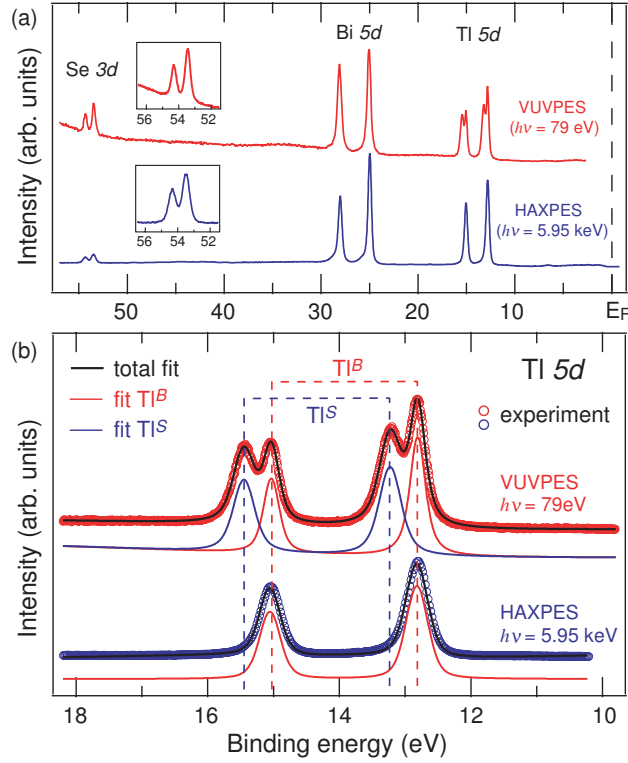
Figure 7.4: Results of the photoelectron spectroscopy with vacuum ultraviolet radiation (VUV-PES) and hard x-ray (HAX-PES) (a) in the wide energy region and (b) Tl $5d$ core-level energy region. VUV-PES (HAX-PES) result is denoted by upper (lower) line. The solid lines in (b) indicate (black) total fitting result, (red) the Tl $5d$ peaks denoted with Tl^B as the main line and (blue) Tl^S as the satellite line. The observed Tl $5d$ spectra are fitted with Voigt functions and a Shirley-type background. The fitting parameters are listed in Table I. Adapted from reference [92].

Commonly, a variation of atomic configurations leads to a modification of chemical bonding, which has been widely studied by CL-PES in clusters and step edges at surfaces [94, 95]. Considering the proposed model as shown in

	Tl^B	Tl^S
VUV-PES ($h\nu$=79 eV)		
E_B of $5d_{5/2}$	12.81 ± 0.01	13.23 ± 0.01
spin-orbit splitting	2.22 ± 0.02	2.22 ± 0.02
lorentzian width	0.16 ± 0.01	0.20 ± 0.01
Gaussian width	0.19 ± 0.02	0.27 ± 0.02
ΔE	0.42 ± 0.02	
HAX-PES ($h\nu$=5.95 keV)		
E_B of $5d_{3/2}$	12.82 ± 0.03	-
spin-orbit splitting	2.23 ± 0.05	-
lorentzian width	0.16 ± 0.01	-
Gaussian width	0.30 ± 0.02	-

Table 7.1: Fitting parameters for the components of the Tl $5d$ core-level in Fig. 3(b). Tl^B and Tl^S show the components of the Tl $5d$ state located at lower and higher E_B, respectively. Listed all energy units are eV. The lorentzian and Gaussian widths refer to the full width at half maximum. ΔE indicates the size of splitting for the two components.

Fig. 7.3(b), one may expect that the chemical condition of Tl atoms forming the islands and buried in the bulk are different. In this respect, studying the chemical character with CL-PES is useful to examine our model. Therefore, we focus on the core-levels spectra obtained by the surface sensitive VUV-PES and the bulk sensitive HAX-PES techniques. Figure 7.4(a) shows VUV-PES (top) and HAX-PES (bottom) results in a wide binding energy (E_B) range. Three core-levels are identified as Se $3d$, Bi $5d$ and Tl $5d$. It becomes evident that VUV-PES results for Bi and Se core-levels are overall similar to those measured by HAX-PES. Note that the both binding energies for VUV-PES results are apparently corresponding to that for HAX-PES results, which indicates that a band bending effect is considered to be negligible in this material. By contrast, a distinct difference in the spectrum is visible in the Tl $5d$ core-levels; HAX-PES result shows a single spin-orbit doublet, whereas an additional peak appears for each spin-orbit component in the VUV-PES data. The magnified Tl $5d$ core-level spectra are shown in Fig. 7.4(b), where one can clearly see two components (named as Tl^B and Tl^S) in the VUV-PES data (red), whereas HAX-PES data (blue) only shows single component of

Tl $5d$ that energetically coincides with the component of Tl^B in VUV-PES data. Considering the surface sensitivity of VUV-PES experiments as well as the bulk sensitivity of HAX-PES experiments, the Tl^S line is considered as the satellite which is possibly linked to the formation of the islands at the surface as seen in STM and the Tl^B emission is determined to be emitted from the bulk as the main line. Then, these components as seen in the VUV-PES spectra are decomposed by a fitting procedure using four Voigt functions and a Shirley-type background. The fitting results are indicated by the solid lines in Fig. 7.4(b). To obtain the best fit, the Gaussian width of all Voigt profiles had to be set larger than the experimental energy resolution probably due to lattice vibration [96]. The fitting parameters are tabulated in Table 7.1. We find that the lorentzian and Gaussian widths for Tl^S peaks are slightly larger than those for the Tl^B peaks. The size of the splitting between Tl^B and Tl^S components in the VUV-PES spectrum is estimated to be ΔE=420±20 meV.

To further confirm the surface and bulk origin of the two components observed in VUV-PES measurement, we have examined the Tl $5d$ core-level spectra using various excitation energies. The measurement mirrors similar experiments used to separate surface and bulk components at conventional semiconductor surfaces [97, 98]. In these reports, the kinetic energy (E_{kin}) of photoelectrons was tuned to a low energy below 10 eV, where the IMFP will rapidly increase as shown in the universal curve of the IMFP [40]. This can be expected to result in a mixture between surface and bulk sensitivity. To continuously change the surface sensitivity, we use the tunable photon source provided by the synchrotron radiation in the $h\nu$ range of 24-190 eV. The observed spectra are summarized in the Fig. 7.5(a) together with their fitting results. The lorentzian widths shown in Table I are used for the fitting functions. The total spectra are found to strongly depend on $h\nu$. At $h\nu$=27 eV, the main Tl $5d$ core-level emission (Tl^B) is stronger than the emission from the satellite (Tl^S). With increasing $h\nu$ to 46 eV, the intensity of Tl^S becomes stronger than the main line. Further increase of the excitation energy towards $h\nu$=190 eV again reduces the weight of Tl^S close to its low $h\nu$ value. Figures 7.5(b) and (c) show a magnified view of the Tl $5d$ core-level spectra normalized by the intensity of the Tl^S peak in the energy window of Tl $5d_{3/2}$ and Tl $5d_{5/2}$ components, respectively. For both peaks in the doublet, a similar $h\nu$ dependence is observed, except for the fact that the intensities of Tl^B for the $5d_{3/2}$ and $5d_{5/2}$ peaks show their minimal at different photon energy, $h\nu$=49 eV and 52 eV, respectively. This corresponds roughly

151
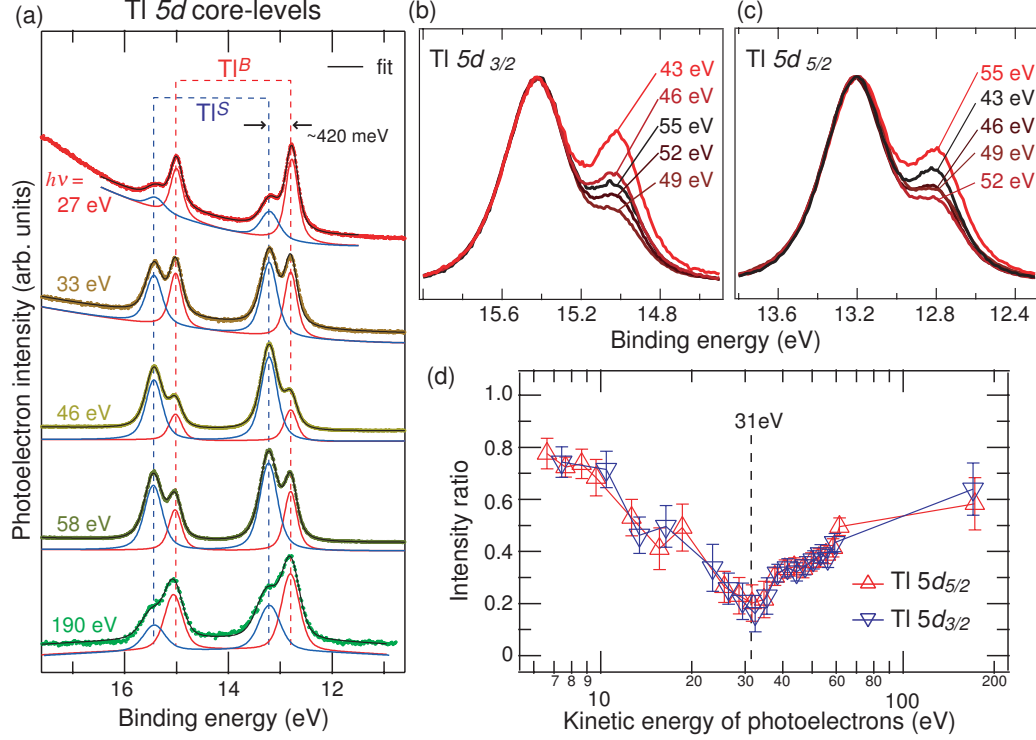
Figure 7.5: (a) Core-level spectra for Tl $5d$ with vacuum ultraviolet (VUV) radiations ranging from 27 to 190 eV. The corresponding E_{kin} of the photoelectrons from $5d_{5/2}$ are shown in the figure. The red (blue) solid line shows the Tl^B (Tl^S) lines decomposed with fitting and the Lorentzian widths are fixed at the same value listed in Table I. (b) and (c) show intensity evolution of the Tl^B for Tl $5d_{3/2}$ and Tl $5d_{5/2}$ with respect to that of Tl^S peaks, respectively. (d) Intensity ratios between Tl^B and Tl^S for each doublet as a function of E_{kin} of photoelectrons. The intensity ratios are defined with the equation as described in the main text. Adapted from reference [92].

to the spin-orbit splitting of the doublet and demonstrates that the changes in the intensity of the spectra can be better explained with a dependence on E_{kin} rather than $h\nu$. In the following, we will analyze the intensity ratio between main line and its satellite by defining the normalized intensity ratio:

$$r_j = \frac{I_j^B}{I_j^S + I_j^B} \tag{7.1}$$

where I_j^B is the fitted intensity of the Tl^B line and I_j^S the corresponding intensity from the Tl^S line of the $5d_j$, respectively (j=5/2 or 3/2). The E_{kin} dependence of $r_{5/2}$ and $r_{3/2}$ are summarized in Fig. 7.5(d). As suggested from the preceding qualitative analysis in Fig. 7.5(b) and (c), it is found that the E_{kin} dependences of both Tl $5d$ doublets are indeed identical. The intensities of the Tl^B lines increase towards lower and higher E_{kin} from their minimum near E_{kin}=31 eV, which is in excellent agreement with the universal curve of photoelectron IMFP [40]. This result can further confirm the bulk origin of Tl^B observed in our HAX-PES experiment. and is consistent with our HAX-PES result that Tl^S and Tl^B states originate from the surface and bulk, respectively.
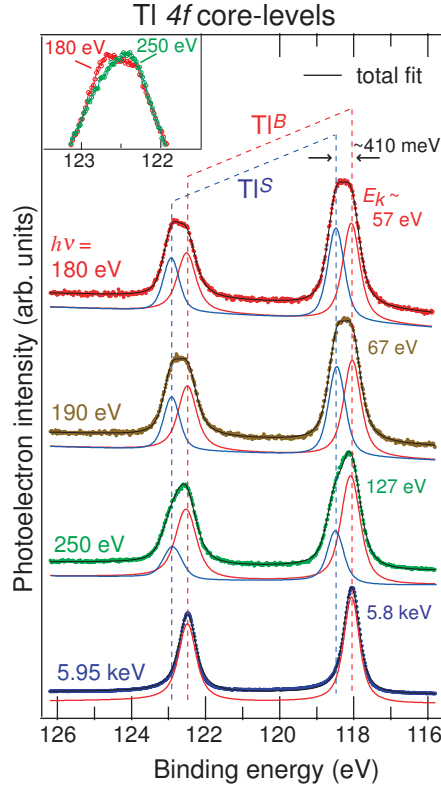
Figure 7.6: Core-level spectra for Tl $4f$ with VUV radiations ranging from 180 to 250 eV as well as hard x-ray. Adapted from reference [92].

To analyze the relation between Tl emission from the surface and the bulk,

we focus on the core-level shift (CLS) between the Tl^S and Tl^B states. The size of the CLS generally depends on several parameters, such as the bonding distance, the valency of the atom and the local chemical surrounding [99]. The Tl 5d core-level is normally thought as a semi-core state because it is located energetically close to the valence band (E_B=12-15 eV) and thus it is highly sensitive to the physical and chemical environments compared to other deeper lying core-levels. Therefore, in order to reduce the possibility that shifts are induced from beyond the nearest neighbor lattice site, it is important to compare the CLS of the Tl 5d line with other Tl core-levels that are more strongly screened. To do so, we chose to investigate the Tl 4f core-level, which is located at higher E_B ($\sim$118 eV) than that of the Se 3d, Bi 5d and Tl 5d core-levels. Figure 7.6(e) shows the spectral features for Tl 4f core-levels excited with several different $h\nu$ and fitted with Voigt profiles. Even without resorting to an analysis of the fitting results, one can already see that the spectral weight on the higher E_B side increases, if the E_{kin} of photoelectrons is close to the highly surface sensitive values (see the inset). Accordingly, the spectral weight at lower E_B increases at more bulk sensitive E_{kin}. This behavior is verified in more detail by the fitting functions. Similar to Tl 5d, we are able to identify a Tl^B main line by comparing the VUV-PES data with the spectrum taken with HAX-PES which again shows a single component. The Tl^B and Tl^S lines of the Tl 4f peak show comparable E_{kin} dependence of the Tl 5d core-levels. The size of the CLS between these lines is estimated to be 410$\pm$20 meV which is well comparable to that of the Tl 5d level. This finding again support our notion that the chemical state of Tl is strongly deformed by the chemical environment at the surface.

n order to get a proof that no similar CLS exists for the Se or Bi atoms, we focus on the shallow core-levels from these elements next. Figures 7.7(a) and (b) summarize the Se 3d and Bi 5d core-level spectra, respectively. The fitting parameters are as listed in Table II and compared with those for Bi$_2$Se$_3$ as a reference (as discussed later). We find that no additional features, such as shoulders or peak shifts are present in the VUV-PES spectra. Both the Se 3d and the Bi 5d core-level spectra measured by VUV-PES can be reproduced by a single Voigt profiles with the same parameters listed in Table II. Tuning $h\nu$ to obtain a highly surface sensitive condition ($E_{kin} \sim$31 eV) does not change the spectral shape, which is in a strong contrast to the Tl core-levels. We notice that the peak positions slightly shift in different directions for the Se 3d and Bi 5d peaks if the HAX-PES results are compared to those from the VUV-PES measurements. The Bi 5d spectrum measured by HAX-PES is
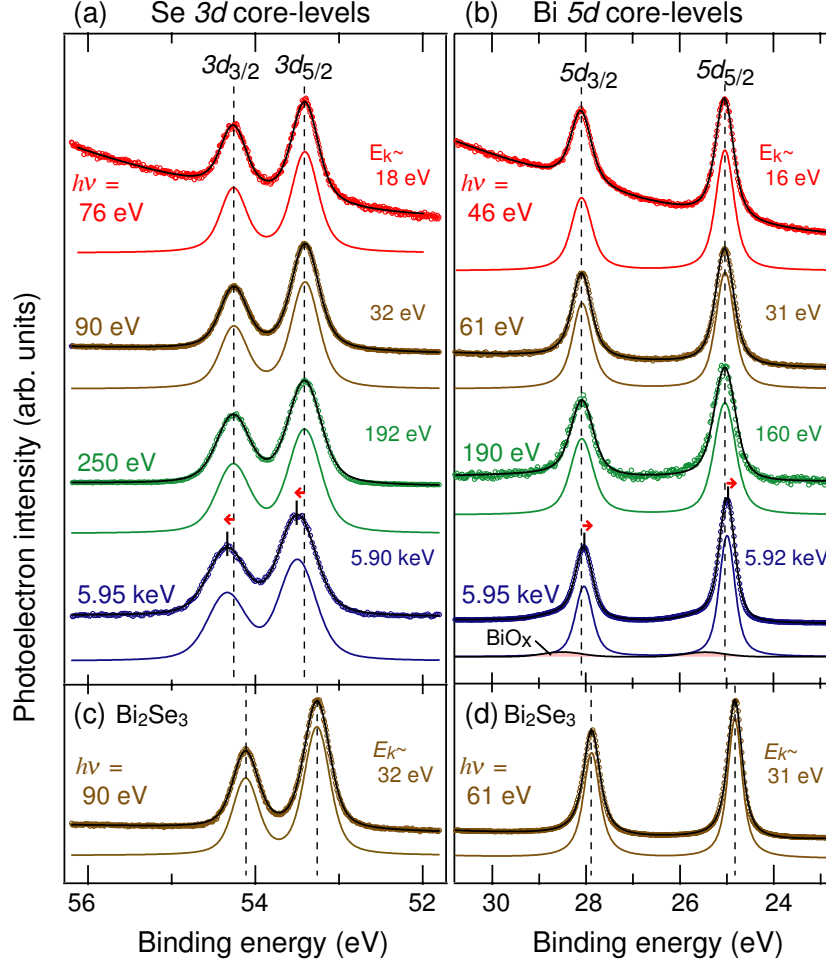
Figure 7.7: Core-level spectra for (a) Se $3d$ and (b) Bi $5d$ with vacuum ultraviolet radiations and hard x-ray. The corresponding E_{kin} of the photoelectron from $3d_{5/2}$ and $5d_{5/2}$ are denoted in the figure. Solid lines show fitting results with parameters listed in Table II. We found the tails in Bi $5d$ spectra taken with hard x-ray (bottom) at higher E_B which is attributed to the oxidized Bi (BiO_x) (shaded area). (c) and (d) are Se $3d$ and Bi $5d$ core-level spectra for Bi_2Se_3 obtained by the selected photon energy to obtain the most surface sensitivity. Adapted from reference [92].

located at lower E_B with respect to that acquired by the VUV-PES while the Se $3d$ shifts to higher E_B with a comparable energy shift of ∼80 meV. For Se

	TlBiSe$_2$	Bi$_2$Se$_3$
Bi 5d core-level		
E_B of 5$d_{5/2}$	25.06 ±0.01	24.83 ±0.01
	(24.98 ±0.03)	
spin-orbit split	3.04 ±0.02	3.05 ±0.02
	(3.03 ± 0.05)	
lorentzian width of 5$d_{5/2}$	0.32 ± 0.02	0.28 ± 0.02
	(0.20 ± 0.02)	
lorentzian width of 5$d_{3/2}$	0.38 ± 0.02	0.34 ± 0.02
	(0.24 ± 0.02)	
Se 3d core-level		
E_B of 3$d_{5/2}$	53.41 ± 0.01	53.26 ± 0.01
	(53.50 ± 0.03)	
spin-orbit split	0.84 ± 0.02	0.86 ± 0.02
	(0.85 ± 0.05)	
lorentzian width of 3$d_{5/2}$	0.20 ± 0.01	0.16 ± 0.01
	(0.20 ± 0.01)	
lorentzian width of 3$d_{3/2}$	0.20 ± 0.01	0.16 ± 0.01
	(0.20 ± 0.01)	

Table 7.2: Fitting parameters of Bi 5d and Se 3d spectra in TlBiSe$_2$ and Bi$_2$Se$_3$. The values of HAX-PES are shown in parentheses. The lorentzian width refer to the full width at half maximum. All listed energy units are in eV.

3d core-level, the CLS can be partially attributed to recoil effect in HAX-PES measurement [100], which is expected to induce an energy shift of $\sim$40 meV to higher E_B, and a single Voigt profile with the same lorentzian width can reproduced the HAX-PES spectrum. However, the lorentzian width of the HAX-PES peak for Bi 5d is smaller than that measured by VUV-PES. This result probably indicates that all observed VUV-PES spectra of Bi 5d include an unresolved surface component.

In order to understand the possible contribution of dangling bonds on the Bi 5d and Se 3d core-levels, we investigate the core-levels of Bi$_2$Se$_3$ in which dangling bonds are believed to be absent. Figures 7.7(c) and (d) show the observed Se 3d and Bi 5d spectra in Bi$_2$Se$_3$ at highly surface sensitive E_{kin}. We find that both core-levels are located at lower E_B with respect

to those of TlBiSe$_2$, indicating the different bonding conditions as well as spontaneous carrier doping effect due to the presence of defects in the bulk for Bi$_2$Se$_3$. We note that the spectral shape in Bi$_2$Se$_3$ is quantitatively close to that in TlBiSe$_2$ for both core-levels and these features are independent of the E_{kin} (not shown). Thus, the contribution of the dangling bonds is found to be weak for Bi and Se core-levels in TlBiSe$_2$ and we consider that an unresolved surface component in TlBiSe$_2$ may be attributed to a surface relaxation effect which is predicted to decay slowly into the bulk [78]. A previous CL-PES measurement on Bi$_2$Se$_3$ with Fe deposition has demonstrated that the spectral feature of Se $3d$ core-level are stable against the chemical environment [101]. Hence, we do not deny the existence of the Se atoms affected by the different chemical surroundings in TlBiSe$_2$.

The proposed model for the surface termination as shown in Fig. 7.3(b) is therefore supported by our core-level PES where only the Tl core-levels are strongly deformed by the surface component. Since a flat surface is generally assumed for the previous calculation [78], the fact that residual islands exist on the surface provides us with a reason why the trivial surface states which present in the calculated band structure are absent in the ARPES measurements as shown in Sec. 5.1. Firstly, due to the small domain size of the islands, the dispersing features of the dangling bond states would be absent, which results from the fact that the dangling bond states are localized on the islands as well as in the Se terminated surface area. The localized states may be energetically located above the Fermi energy or weakly contributing to the intensity of photoelectrons and thus be absent from the ARPES measurements. Secondly, as mentioned in the STM analysis that the island height is smaller than the lattice constant in the bulk, the island deformation may lead to a saturation of the dangling bonds. Finally, the strong ionic nature of the interlayer bonding between Tl and Se can lead an absence of the dangling bond states. Our VUV-PES for Tl $5d$ core-level shows that the surface component is located at ∼420 meV higher E_B than the bulk one. If we assume that the stoichiometry of TlBiSe$_2$ formally assigns the Tl atoms a 1+ oxidation state, the Bi atoms a 3+ state and the Se atoms a 2− state, the energy difference can be expected to be originated from a higher oxidation state more than 1+ of the partially remaining Tl atoms on the surface. According to the coverage of the Tl islands estimated to be half of the surface, the valence number of the rest Tl ions can be assigned nearly 1.5+ states to keep neutrality in the whole of the crystal. The speculation of the higher oxidation state of rest Tl ions has actually good agreement with

the shrink of the interlayer distance in STM analysis because the ionic radius of the residual Tl ions would constrict resulting from the higher oxidation. For this reason, the consideration with the ionic type bonding can give an interpretation of our experimental results and furthermore provide with a reasonable explanation for the absence of the dangling bond states. The presented surface model may motivate future experiments on this surface. Possible experiments include the study of surface deposition which has been widely used on the surface of Bi$_2$Se$_3$ [101, 102, 103, 104], as well as theoretical studies on the surface of TlBiSe$_2$ including the island structure.

7.4 Conclusion

In conclusion, we have experimentally approached the open question of the surface termination problem of TlBiSe$_2$ utilizing STM and CL-PES. The STM results have shown that islands are formed on the cleaved surface. The CL-PES measurements with tunable surface sensitivity have revealed that the spectral features of Tl core-levels are strongly deformed by the surface component in contrast to the other elements. From these findings, we proposed a model for the surface termination that includes Tl islands covering half of the surface which is terminated by a Se layer. We demonstrated that the residual-Tl-island-model is the most likely explanation for the pronounced CLS found in Tl core-levels. The model was also able to account for the absence of the trivial surface state in ARPES measurements. It will motivate further experimental and theoretical studies of the surface properties.

Chapter 8

Final state effects in photoelectron spin polarization via the investigation on topological surface state in Bi$_2$Se$_3$

8.1   Introduction

We come back to the prototypical topological insulator Bi$_2$Se$_3$ and further study the spin texture of the topological surface state using our ESPRESSO machine. Especially, we highlight the circular polarization dependence in ARPES and SARPES measurements, and discuss, how the final state can affect in the observation of intrinsic spin polarizations? This fundamental question is crucial because this would concern the general materials probed with photoemission measurements.

Recently, the several ARPES works on the topological insulators proposed that the interpretation of the circular dichroism in the angular distribution (CDAD) of ARPES is expected to be an efficient probe of spin helical textures of topological surface states, which could be replaced with spin resolved ARPES [105, 106]. This proposal has been supported by several theoretical interpretations [30, 107] that the CDAD pattern represents the orbital angular momentum (OAM) texture in k-space and the spin texture is indirectly probed via the strong spin-orbit coupling, which is introduced in Sec. 1.3.4.

However, in the previous experimental and theoretical works, the photon energy ($h\nu$) dependences, the so-called final state effect in the photoemission, are neglected. We note that CD is universal effect, which is well known to occur in chiral materials [108], magnetic materials [109] and even in the small spin-orbit coupled materials [110]. Not surprisingly, recent ARPES work on Bi$_2$Te$_3$ by *Rader*'s group demonstrated that the final state effect dominates the CDAD pattern, which generally oscillates several times as a function of $h\nu$ [111]. According to their calculation based on the first-step model, the sign reversal corresponds to the switching the final state in dipole transitions from $p \to s$ to $p \to d$ transitions.

In contrast to the developed discussion about CDAD effect of TSS, the possible influence of the final state effect in SARPES measurement remains as a open question. In 1969, *Ugo Fano* theoretically predicted that the photon helicity induces the high spin polarization along the quantum axis of the photon in free Cs atoms through the spin-orbit coupling, which is named Fano effect [112]. The prediction was experimentally verified by *Heinzmann*'s group in 1970, where the pronounced spin polarization of photoelectron was measured to be between 100 % and −50 % as a function of $h\nu$ [113]. Observed $h\nu$ dependence of the spin polarization can be easily clarified with the different matrix elements of the dipole transitions. Thus, it is recognized that the spin of the emitted electron follows the quantum axis of the incident

light in spherical symmetric systems such as free atoms and molecules (see Ref. [90]).

However, since the electronic state in solids is restricted by their crystal symmetry, the interpretation becomes much complicated and therefore the final state in dipole transition is usually assumed to be a free electron state. Recently, *Louie*'s group developed the model for the spin polarization of photoelectron from TSS [114]. According to their model, the electronic field of the incident light can interact with electron spin via the strong spin-orbit coupling in the photoemission process, which leads to the strong spin-flip effects. This particular polarization dependence of the spin polarization was demonstrated by laser SARPES measurement by *Lanzara*'s group [115] in which the spin polarization of the photoelectron from TSS is strongly influenced not only by the circular polarization but also linearly polarized light and consequently the measured spin spin polarizations lose the initial spin information. Nevertheless, we note that the model [115] ignores the realistic final states in the photoemission process.

Therefore, in order to get more insight into the final state effect in the photoemission ignored in current experientially and theoretical works on TIs, the $h\nu$ and light polarization dependences have to be explored. Furthermore, the final-state effects need to be further defined for the purpose of spin manipulation in opto-spintronics applications [116].

Here, we show our experimental verification of the influence of the final state effect in the spin polarization of photoelectron from the TSS in Bi_2Se_3. By using the tunable photon and light polarization from the synchrotron radiation, we clarify its $h\nu$ and light polarization dependences. We unambiguously demonstrate that the spin polarization of photoelectrons is influenced through the variety of photoemission process that strongly depends on the final states reached at different photon energies. This work provides a methodology for manipulating photoelectron spins in the topological insulators.

8.2 Experimental set-up

Single crystalline samples of Bi_2Se_3 were grown by the standard procedure as explained in Chap. 4.2. High quality CDAD patterns were obtained by high-resolution angle-resolved photoemission spectroscopy (ARPES) at BL9A and spin- and angle-resolved photoemission spectroscopy (SARPES) experiments

were performed with synchrotron radiation at the ESPRESSO machine of Hiroshima Synchrotron Radiation Center (HiSOR). Photoemission spectra at both systems were acquired at around 60 K. The energy resolutions were set below 15 and 30 meV for ARPES and SARPES measurements with the $h\nu$ below 17.7 eV. The angular resolutions of ARPES and SARPES measurements was set 0.1 and 0.7°, respectively. Clean surfaces were obtained by cleaving in ultrahigh vacuum at low temperature $\sim$60 K with ultra-high vacuum conditions better than 1×10^{-8} Pa.
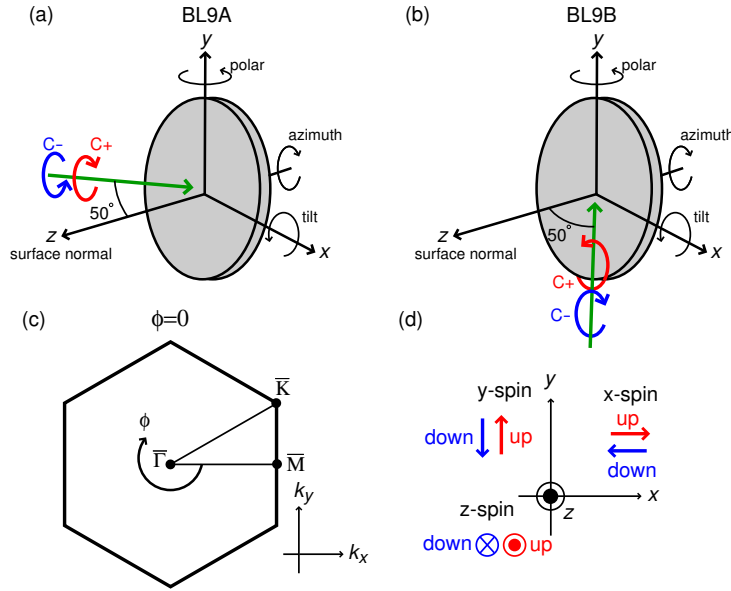
Figure 8.1: Experimental geometry at (a) high-resolution ARPES end-station BL9A and (b) SARPES station BL9B. (c) Relation of the high symmetry lines of the sample and k, which can be controlled with azimuthal rotation. (d) Definition of spin-up and spin-down directions in real space.

Experimental geometries at BL9A and BL9B are shown in Figs. 8.1(a) and (b), respectively. Six-axis goniometer is equipped at both of the systems. The synchrotron radiation impinges onto the sample surface in the different incident direction for the end-stations. The difference has to be taken into account when one considers the definition of the spins of circularly polarized lights. When azimuthal angle (ϕ) is 0, the $\bar{\Gamma}$-$\bar{M}$ and $\bar{\Gamma}$-$\bar{K}$ high symmetry line of the surface Brillouin zone correspond to x and y direction as depicted in

Fig. 8.1(c). The definition of spin axes are shown in Fig. 8.1(d).

8.3   Results and discussion
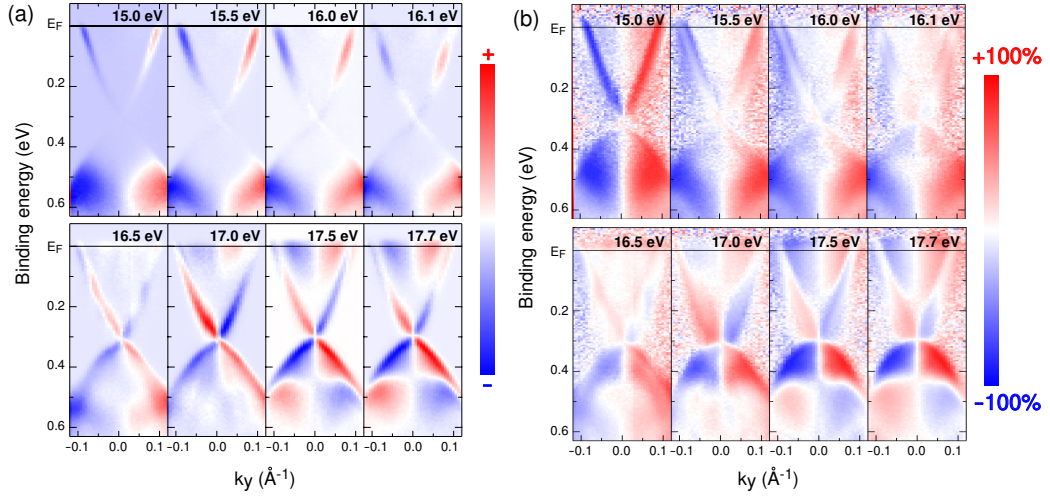
Figure 8.2: Result of the circular polarization dependence of ARPES intensity maps in Bi_2Se_3. (a) ARPES intensity difference between spectra taken with right- ($C+$) and left- ($C-$) circularly polarized light, which is defined as $I_{C+} - I_{C-}$. (b) Normalized difference defined by $\frac{I_{C+} - I_{C-}}{I_{C+} + I_{C-}}$.

Figure 8.2 shows the CDAD patterns of the ARPES spectra taken with photon energies between 15.0 and 17.7 eV at BL9A. In the figure, CDAD patterns are shown in two ways, (a) difference of the intensities ($I_{C+} - I_{C-}$) and (b) normalized difference (($I_{C+} - I_{C-}$)/($I_{C+} + I_{C-}$)). The former way can keep clearness of the surface and bulk energy dispersion with the intensity differences but loses the quantitative information of the size of CDAD. The size of CDAD can be quantified in the latter way. At first, the clear CDAD can be identified not only for the TSS but also for the bulk conduction and valence bands in the result with $h\nu$=17.7 eV in which the sign of CDAD in the TSS significantly reverses with respect to the Dirac point (E_B=300 meV) and the $\bar{\Gamma}$ point. This reminds us of the spin texture of TSS previously studied with SARPES measurement. However, one can find that the feature of the CDAD pattern strongly depends on the photon energies in both of the bulk

and the surface states. It is noticed that the CDAD patterns are similar for $h\nu$=17.0-17.7 eV but the CDAD amplitude crucially decreases with further decreasing $h\nu$, and the intensity near the DP diminishes at 16.0 eV. Finally, the sign of CDAD above the DP, the so-called upper TSS (UP-TSS), is reversed below $h\nu$=16.0 eV. Note that the reversed sign can be identified only above the DP while it represents the identical feature below the DP for the result of 15.0 eV with respect to that of 17.7 eV. These results pose a question about previous interpretations that the CDAD of TSS represents the helical spin-texture in k-space. It is then stressed that the final state effect plays an important role in CDAD, where the final state in the photoemission switches into the different orbital character for $h\nu$=15.0 and 17.7 eV. This situation can provide us with an opportunity to study the contribution of the final state effect in SARPES measurement that is a heart of our interest in this chapter.

To investigate the influence of the final state effect in the observed spin polarization, we have performed SARPES measurement with ESPRESSO machine utilizing various photon energies. Figures 8.3 represents normalized CDAD intensity maps selected from Fig. 8.2(b) and the spin-resolved spectra of x and z components obtained with circularly polarized lights (C+ and C−) and the $h\nu$ of (a) 17.7 eV, (b) 16.0 eV and (c) 15.0 eV. Black dashed lines in the CDAD maps mark the k positions for the SARPES measurements. For the SARPES spectra obtained by $h\nu$=17.7 eV in Fig. 8.3(a), one may notice that the spin-up and spin-down EDCs along the x direction slightly change if the helicity of the light is reversed while they almost identical in the result for the z spin component. This result indicates that in-plane spin component is affected by the light helicity meaning that the quantitative information of the spin polarization in the initial state is modified during the excitation by circularly polarized lights. However, we note that the sign of the spin polarization of the TSS located at $E_B \sim$260 meV is identical for both light polarizations. Next, the low $h\nu$ was utilized for SARPES measurement to tune the orbital character in the final state and then we will discuss the influence in the spin-polarization of photoelectrons. For the spin-resolved spectra of x spin, it is apparent that no significant change is identified, where the intensity of the spin-up states is higher than that for the spin-down states in the these photon energies. However, the situation is completely different for the z spin component, that is, the z spin polarization significantly decreases and reaches nearly 0 at $h\nu$=16.0 eV. It goes to negative at $h\nu$=15.0 eV. One may notice that the sign reversal feature in z spin
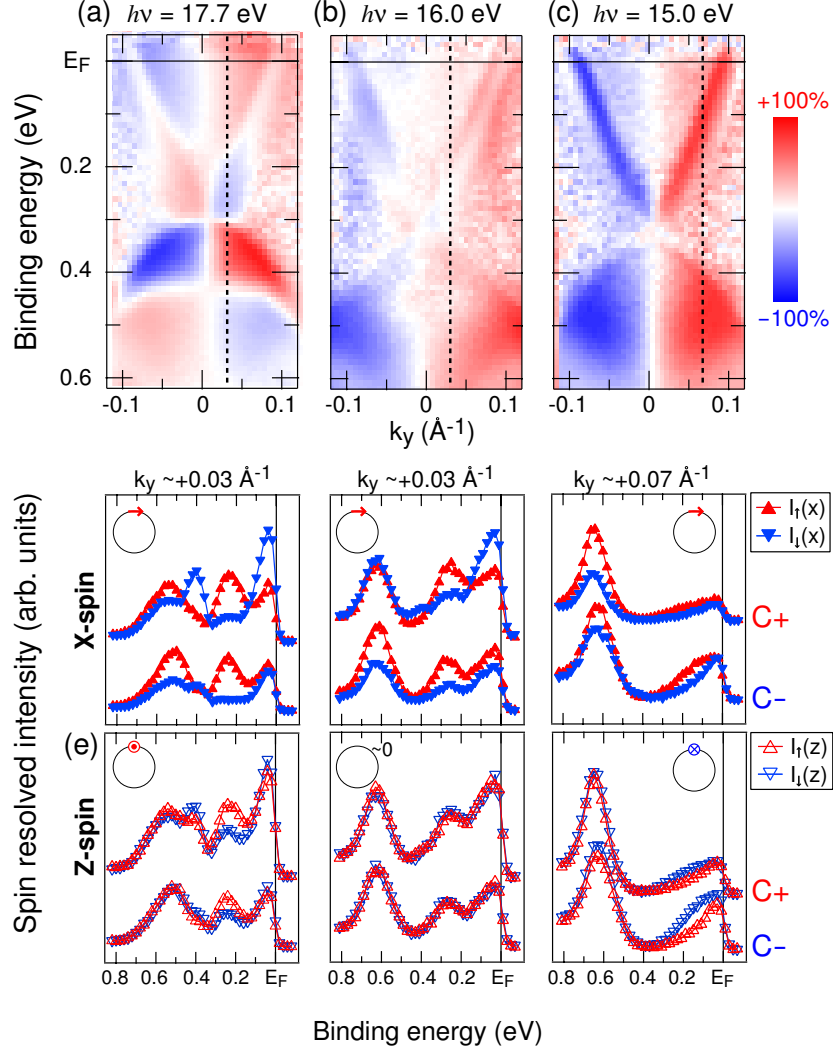
Figure 8.3: Results of the circular polarization dependence in SARPES measurement acquired at $h\nu$ of (a) 17.7 eV, (b) 16.0 eV, (c) 15.0 eV and circularly polarized lights (C+ and C−). (top) normalized CDAD intensity maps from Fig. 8.2(b). (middle) and (bottom) Obtained SARPES spectra in (middle) x and (bottom) z direction along the dashed line in the top panels. Inset figures show the schematics of constant energy contour of TSS and observed spin orientations.

polarization is similar to the $h\nu$ dependence of CDAD pattern as discussed in Fig. 8.2. Therefore, the $h\nu$ dependence of z spin polarization is likely to

be a signature of the final state in the dipole matrix element.
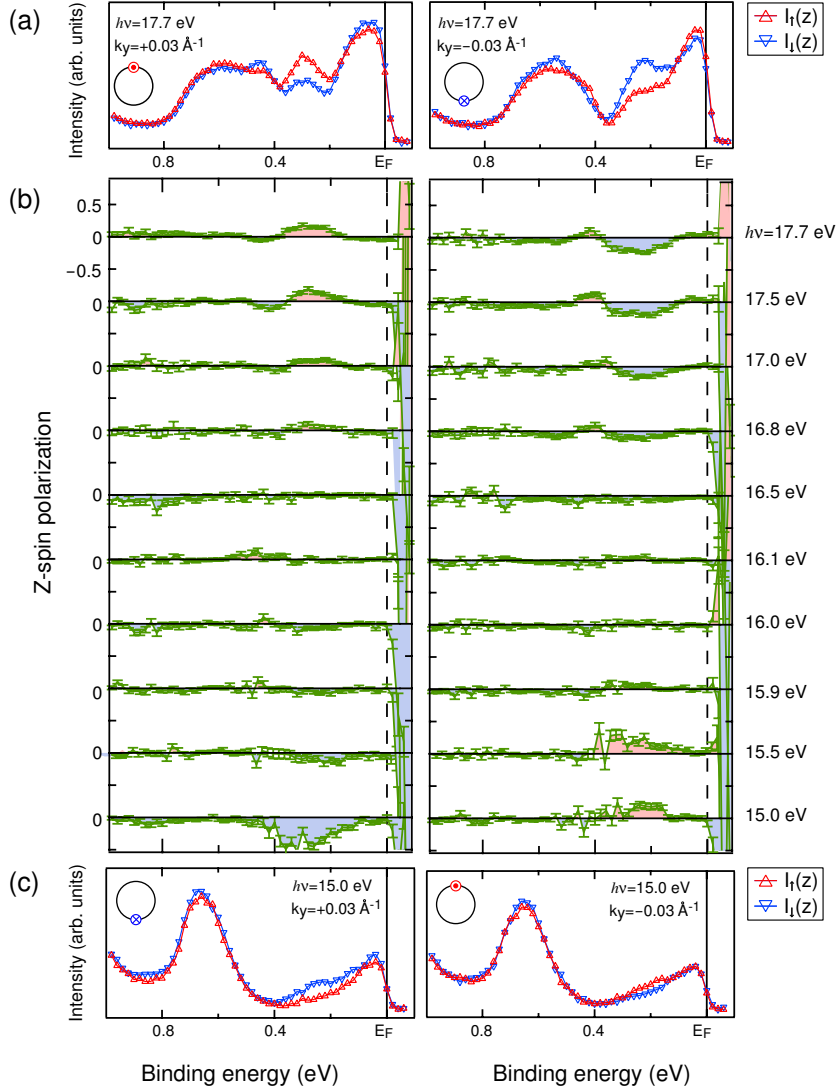
Figure 8.4: $h\nu$ dependence of the out-of-plane spin component excited with horizontally polarized light. (a) Obtained SARPES spectra at (left) k_y=+0.03 $\mathring{A}^{-1}$ and (left) k_y=−0.03 $\mathring{A}^{-1}$ at $h\nu$ of 17.7 eV. (b) Obtained z spin polarization with various photon energies. (c) SARPES spectra at $h\nu$ of 15.0 eV.

Particularly, we note that the z spin polarization and its $h\nu$ dependence are observed also by the linearly polarized light. Figure 8.4(a) shows the

spin-resolved spectra of the z spin component with horizontally polarized light ($h\nu$=17.7 eV). These spectra are measured at k_y=+0.03 $\mathring{A}^{-1}$ (left) and -0.03 $\mathring{A}^{-1}$ (right). The observed z spin polarizations are summarized in Fig. 8.4(b). The sign of spin polarization in the result for $+0.03$ $\mathring{A}^{-1}$ is identical with that obtained for the circularly polarized lights and is reversed at -0.03 $\mathring{A}^{-1}$ as shown in figure 8.4(a). In addition, the absolute value of the spin polarizations for both k_y becomes smaller with decreasing $h\nu$ to 16.0 eV and finally its sign is reversed at 15.0 eV as shown in Fig. 8.4(b), which is consistent with the result excited with circularly polarized lights. The absence of light polarization dependence in spin polarizations is completely different from the well-known final state effect, Fano effect and also Louie's model.
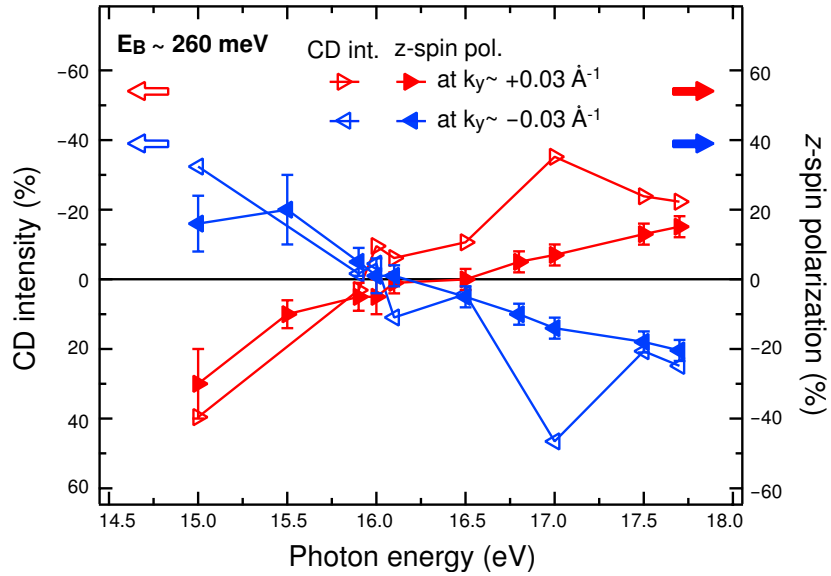
Figure 8.5: Summarized hn dependences of CDAD intensities of TSS and the spin polarizations. Opened (closed) red and blue triangles represent the CDAD intensities (the z spin polarizations) of the TSS at E_B=260 meV, k_y=+0.03 $\mathring{A}^{-1}$ and -0.03 $\mathring{A}^{-1}$, respectively.

Observed $h\nu$ dependence of the CDAD intensities and the z spin polarizations of photoelectron with horizontally polarized lights are summarized into Fig. 8.5, where open (filed) red and blue triangles represent the CDAD intensities (the z spin polarizations) of UP-TSS at E_B=260 meV, k_y=+0.03 $\mathring{A}^{-1}$

and -0.03 $\mathring{A}^{-1}$, respectively. Apparently, both $h\nu$ dependences show identical feature in which the signs is inverted at the same $h\nu$ ($h\nu$=16.0 eV). From the nice consistency, one may consider that the realization of CDAD reflects the excitation of z spin polarization via the same dipole matrix elements. However, we note that our results exclude such a possibility because our SARPES results crucially indicate that the observed z spin polarizations are independent on the light polarizations and especially it can be exited even by the linearly polarized light. Therefore, we consider that the CDAD effect is unlikely to create the z spin polarization.

Below, we discuss whether the origin of z spin-polarization can be explained with several proposed models as introduced in Sec. 1.3.2 and Sec. 1.3.4. The perpendicular spin component can be allowed in $\bar{\Gamma}$-$\bar{K}$ line owing to the hexagonal warping effect as we studied in Chap 4.2. Recently, a theoretical model with the entangled spin-orbital texture has been proposed for Bi$_2$Se$_3$. There is another interpretation that the $h\nu$ dependence in z spin polarizations originate from the layer-dependent textures though the presence of such an initial state spin texture has not yet been experimentally confirmed.

This fundamental issue can be verified with the crystal symmetry of the target material. Note that the reversed spin polarization feature between different k_y positions is identified for all observed spin polarizations obtained with different photon energies as shown in Fig. 8.4(b). In fact, the result can be easily explained by the crystal symmetry of Bi$_2$Se$_3$. Since this compounds has the mirror plane along $\bar{\Gamma}$-$\bar{M}$ line (corresponding to x direction in our geometry), the electronic structures have to follow the mirror symmetry operation ($y\rightarrow -y$). Importantly, the experimental geometry is also symmetric for the measurements at $+k_y$ and $-k_y$ (see Fig. 8.1). The adequate SARPES measurement geometry promises that the spin polarization of photoelectrons should satisfy the symmetry transformation, which is expressed as follows:

$$P_z(+k_y) = -P_z(-k_y) \tag{8.1}$$

where P_z is the spin polarization of photoelectron along z axis. This equation can reproduce the revered spin polarization feature as a function of k_y and thus it is likely to be a consequence of the crystal symmetry including the experimental geometry.

Additionally, as a consequence of the three-fold and the mirror symmetries, the z spin polarization in the initial state should be three-fold symmetric (antisymmetric). Therefore, we performed SARPES measurement
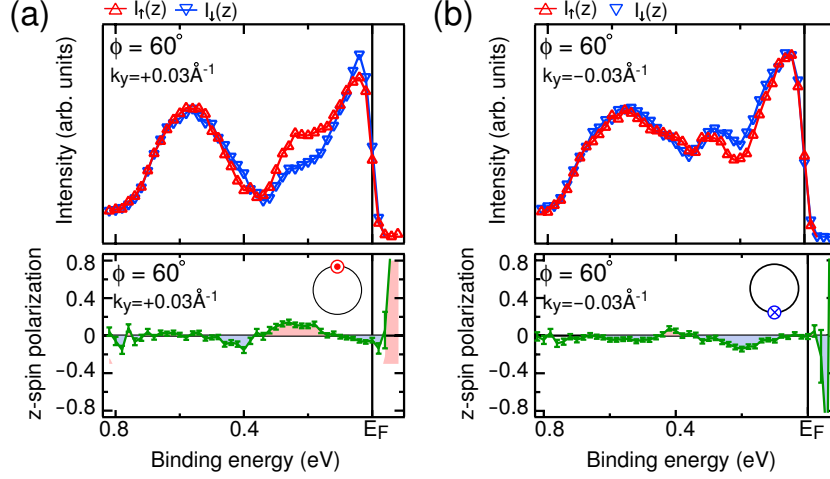
Figure 8.6: (top) SARPES spectra of out-of-spin component and (bottom) the spin polarizations at the different sample geometry with the azimuthal rotation of $60°$ and obtained with horizontally polarized light and the $h\nu$ of 17.7 eV for (a) $k_y=+0.03$ $\mathring{A}^{-1}$ and (b) -0.03 $\mathring{A}^{-1}$.

at the different sample geometry with the azimuthal rotation of $60°$. The spin-resolved spectra and the spin polarizations in z axis obtained with horizontally polarized light and the $h\nu$ of 17.7 eV are shown in Fig. 8.6. However, in sharp contrast to the expectation based on the symmetry consideration, our SARPES results represent that the z spin polarization does not depend on the azimuthal angle rotation for both $+k_y$ and $-k_y$ positions, which ambiguously tells us that the observed z spin polarization does not reflect the initial state. Furthermore, since also the final state should be restricted by the crystal symmetry, it is very surprising that the observed spin polarization of photoelectron does not follow. The results demonstrate that the spin polarization of photoelectrons is influenced by the complicated photoemission process (still let us call it the final state effects in the wide sense) and should always include particular $h\nu$ dependence and geometry effects. Thus, we have identified the observed $h\nu$ dependence of z spin polarization as a result of the final state effects and possibly reflects the switching of the orbital character in the final state confirmed by the reversal CDAD sign. In order to comprehensively understand the process leading to these features, the one-step photoemission calculation with the time-reversed LEED final

169

state is strongly required.
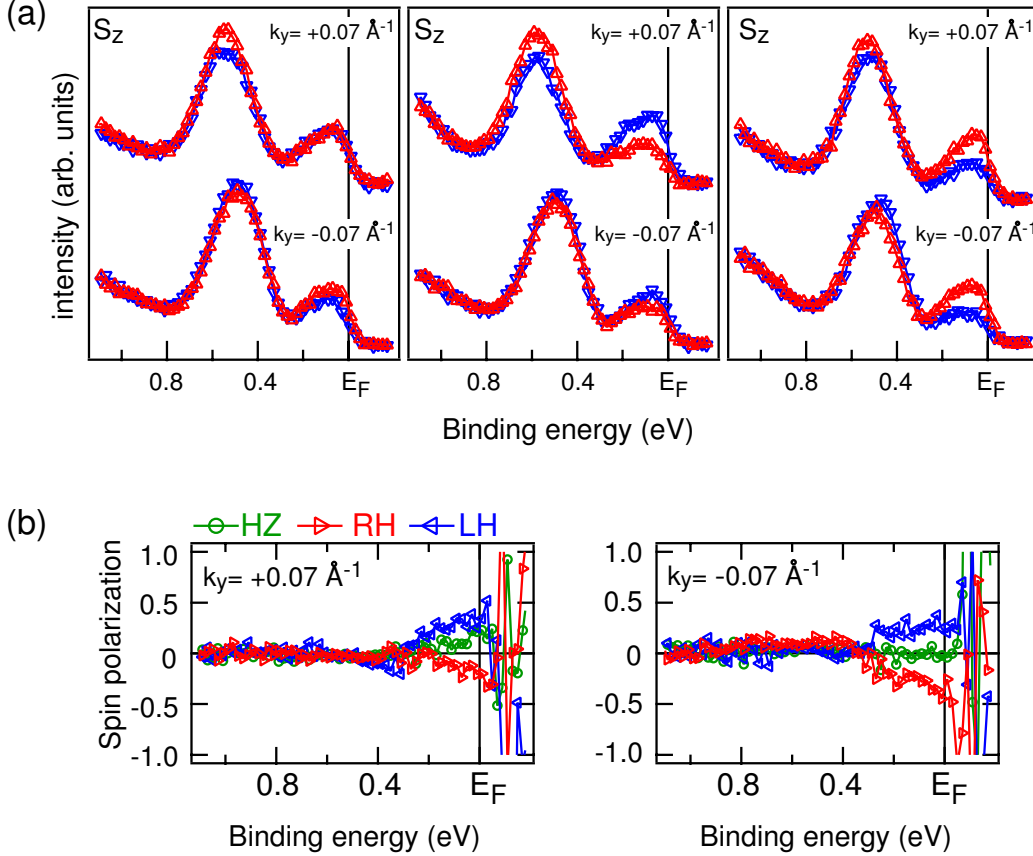
Figure 8.7: Spin resolved energy distribution curves for z-spin component excited with $h\nu$=51eV. (a) Obtained spin-resolved spectra with (left) horizontally, (middle) $C+$ and (right) $C-$ polarized lights. (b) Experimental spin polarizations.

However, we find a completely different situation when using circularly polarized lights at $h\nu$=51 eV. Figure 8.7(a) shows the spin-resolved spectra for the z components acquired with horizontally (left), $C+$ (middle) and $C-$ (right) circularly polarized lights. These spectra obtained at k_y=+0.07 and -0.07 $\mathring{A}^{-1}$ positions with azimuthal angle of 0°. Corresponding spin polarizations are shown in Fig. 8.7(b) where the green, red and blue color marks denote those obtained with horizontally, $C+$ and $C-$ circularly polarized lights, respectively. For the result obtained for the horizontal polarization,

the out-of-plane spin component is small/absent at both k_y positions. However, when the light polarization is turned into the circular ones, the photoelectron spins significantly tend to point toward the out-of-plane direction. Moreover, the spin direction depends on the photon helicity instead of the reversed spin polarization feature with respect to k_y position. This feature is not satisfied with the symmetry consideration expressed by Eq. 8.1, which indicates that the photon polarization breaks the symmetry and contributes to the photoemission final state effect. Thus, the photoemission process at this $h\nu$ is consistent with the spin-flip model proposed by *Louie*'s group where the spin-degenerate free-electron-like final states are assumed as the final state. This suggests that the spin polarization of photoelectrons is influenced through the variety of photoemission process that strongly depends on the final states reached at different photon energies.

8.4   Conclusion

We have experimentally investigated the influence of the final state effect on the spin polarizations of topological surface state in the prototypical TI Bi_2Se_3. Between $h\nu$=15.5 eV and 17.7 eV, the CDAD measurement have probed the existence of the orbital character switching in the final state. The SARPES measurements with these photon energies have demonstrated that the perpendicular spin component to the surface reflect the orbital character switching as a final state effect although in-plane spin texture roughly reflects the initial state. The experimental spin polarization has been found to be quantitatively identical with those obtained by the different light polarizations, which is in sharp contrast to the previously proposed spin-flip model. We have further demonstrated that the particular final state effect in the observed spin polarization can be controlled into the spin-flip type of the final state if $h\nu$ is tuned into 51 eV. These results unambiguously indicate that the spin polarization of photoelectrons is influenced through the variety of photoemission process that strongly depends on photon energies. Our experimental demonstrations can universally provide important indications in the understanding of the final state effect of the photoemission process and establishing a methodology for controlling photoelectron spins.

Chapter 9

Summary

In summary, the electronic structure of spin polarized Dirac surface states in various chalcogenide topological insulators have been investigated by the photoemission spectroscopy with synchrotron radiation. Furthermore, we have developed the methodologies for the carrier manipulation and the spin manipulation in the Dirac systems. These finding can open path way to study intriguing physical phenomena as well as the designing the new devices.

The hexagonally shaped Fermi surface of the surface state in the prototypical topological insulator Bi_2Se_3 has been experimentally identified, for the first time, by means of high-resolution ARPES measurement. The bulk and surface carrier densities have successfully manipulated with subtle Mg doping into the quantum topological transport regime. The paramagnetic property in the non-magnetic impurity doped in Bi_2Se_3 has been revealed by surface sensitive XMCD measurement even in the low temperature. This result imply that it is not easy to realize the surface intriguing properties in the prototypical insulator.
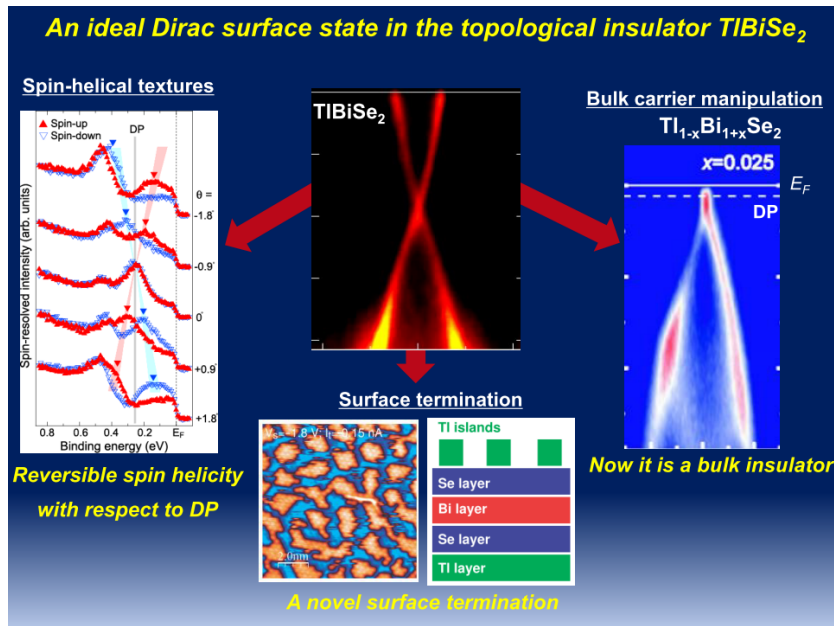
Figure 9.1: Summary of this work on $TlBiSe_2$

By our ARPES measurements, the ternary chalcogenides, $TlBiSe_2$ and $PbBi_2Te_4$, have been newly identified as topological insulators possessing a

single Dirac surface state. Especially, the surface state in TlBiSe$_2$ features in a practically ideal in-gap Dirac state, which has never been achieved even in Bi$_2$Se$_3$. Furthermore, the bulk energy band gap is estimated to be ∼300 meV in TlBiSe$_2$, which is comparable to that for Bi$_2$Se$_3$. These findings favor the realization of the topological spin-polarized transport with high mobility and long spin lifetime at the surface of TlBiSe$_2$. The works on TlBiSe$_2$ in the thesis is summarized in Fig. 9.1.

The spin textures of the ideal Dirac surface state in TlBiSe$_2$ have experimentally evaluated by means of SARPES at ESPRESSO machine. The SARPES results crucially have indicated the reversal spin texture regarding to Dirac point that gives us an opportunity to control spin current if the carrier densities in both the bulk and surface states are tunned. In oder to challenge the unexploited subject we have developed a methodology for the manipulation of the carrier densities in TlBiSe$_2$ and finally achieved the reversal spin current regime with the bulk insulating for the first time.

The surface termination of TlBiSe$_2$ has been directly investigated with scanning tunneling microscope and core-level photoemission spectroscopy with tunable photon. Our STM results have unambiguously represented a novel cleaved surface structure in which the atoms remain and forms islands structure. Core-level photoemission spectroscopy with tunable surface sensitivity has revealed that the spectral features of Tl core-levels are strongly deformed by the surface component. From these findings, we proposed a model for the surface termination in the promising topological insulator.

Finally, the final state effect in the photoelectron's spin polarizations have been studied by means of SARPES measurement with various photon energies and light polarizations. As a remarkable finding, the experimental spin polarization reflects the variety of the photoemission process that strongly depends on the final states reached at different photon energies. Our experimental demonstrations can universally provide important indications in the understanding of the final state effect of the photoemission process and establishing a methodology for controlling photoelectron spins.

References

[1] Midred S. Dresselhaus, Gene Dresselhaus, and Jorio Ado. *Group Theory Application to the physics of Condensed Matter*. Springer, (1962).

[2] S. LaShell, B. A. McDougall, and E. Jensen. *Spin splitting of an au(111) surface state band observed with angle resolved photoelectron spectroscopy*. Phys. Rev. Lett., **77**, 3419, (1996).

[3] Christian Ast, Jürgen R. Henk, Arthur Ernst, Luca Moreschini, Mihaela C. Falub, Daniela Pacilé, Patrick Bruno, Klaus Kern, and Marco Grioni. *Giant spin splitting through surface alloying*. Phys. Rev. Lett., **98**, 186807, (2007).

[4] Yu. A. Bychkov and E. I. Rashba. *Properties of a 2d electron gas with lifted spectral degeneracy*. JETP Lett., **39**, 78, (1983).

[5] Tsuneya Ando, Yukio Matsumoto, and Yasutada Uemura. *Theory of hall effect in a two-dimensional electron system*. J. Phys. Soc. Jpn., **39**, 279–288, (1975).

[6] K. v. Klitzing, G. Dorda, and M. Pepper. *New method for high-accuracy determination of the fine-structure constant based on quantized hall resistance*. Phys. Rev. Lett., **45**, 494, (1980).

[7] R. B. Laughlin. *Quantized hall conductivity in two dimensions*. Phys. Rev. B, **23**, 5632, (1981).

[8] D. J. Thouless, M. Kohmoto, M. P. Nightingale, and M. den Nijs. *Quantized Hall conductance in a two-dimensional periodic potential*. Phys. Rev. Lett., **49**, 405, (1982).

[9] J. J. Sakurai. *Modern Quantum Mechanics*. Yoshino-syoten, (1985).

[10] F. D. M. Haldane. *Model for a quantum hall effect without landau levels: Condensed-matter realization of the "parity anomaly"*. Phys. Rev. Lett., **61**, 2015, (1988).

[11] C. L. Kane and E. J. Mele. *Quantum spin hall effect in graphene*. Phys. Rev. Lett., **95**, 226801, (2005).

[12] C. L. Kane and E. J. Mele. Z_2 *topological order and the quantum spin hall effect*. Phys. Rev. Lett., **95**, 146802, (2005).

[13] B. Andrei Bernevig, Taylor L. Hughes, and Shou-Cheng Zhang. *Quantum spin Hall effect and topological phase transition in HgTe quantum wells*. Science, **314**, 1757, (2006).

[14] Markus Konig, Steffen Wiedmann, Christoph Brune, Andreas Roth, Hartmut Buhmann, Laurens W. Molenkamp, Xiao-Liang Qi, and Shou-Cheng Zhang. *Quantum spin hall insulator state in hgte quantum wells*. Science, **318**, 776–770, (2007).

[15] J. E. Moore and L. Balents. *Topological invariants of time-reversal-invariant band structures*. Phys. Rev. B, **75**, 121306, (2007).

[16] Liang Fu, C. L. Kane, and E. J. Mele. *Topological insulators in three dimensions*. Phys. Rev. Lett., **98**, 106803, (2007).

[17] Liang Fu and C. L. Kane. *Topological insulators with inversion symmetry*. Phys. Rev. B, **76**, 045302, (2007).

[18] Jeffrey C. Y. Teo, Liang Fu, and C. L. Kane. *Surface states and topological invariants in three-dimensional topological insulators: Application to $bi_{1-x}sb_x$*. Phys. Rev. B, **78**, 045426, (2008).

[19] D. Hsieh, Y. Xia, L. Wray, D. Qian, A. Pal, J. H. Dil, J. Osterwalder, F. Meier, G. Bihlmayer, C. L. Kane, Y. S. Hor, R. J. Cava, and M. Z. Hasan. *Observation of unconventional quantum spin textures in topological insulators*. Science, **323**, 919–922, (2009).

[20] Pedram Roushan, Jungpil Seo, Colin V. Parker, Y. S. Hor, D. Hsieh, Dong Qian, Anthony Richardella, M. Z. Hasan, R. J. Cava, and Ali Yazdani. *Topological surface states protected from backscattering by chiral spin texture*. Nature, **460**, 1106–1109, (2009).

[21] Haijun Zhang, Chao-Xing Liu, Xiao-Liang Qi, Xi Dai, Zhong Fang, and Shou-Cheng Zhang. *Topological insulators in Bi_2Se_3, Bi_2Te_3 and Sb_2Te_3 with a single dirac cone on the surface.* Nature Phys., **5**, 438, (2009).

[22] Y. Xia, D. Qian, D. Hsieh, L. Wray, A. Pal, H. Lin, A. Bansil, D. Grauer, Y. S. Hor, R. J. Cava, and M. Z. Hasan. *Observation of a large-gap topological-insulator class with a single dirac cone on the surface.* Nature Phys., **5**, 398 – 402, (2009).

[23] Y. L. Chen, J. G. Analytis, J.-H. Chu, Z. K. Liu, S.-K. Mo, X. L. Qi, H. J. Zhang, D. H. Lu, X. Dai, Z. Fang, S. C. Zhang, I. R. Fisher, Z. Hussain, and Z.-X. Shen. *Experimental realization of a three-dimensional topological insulator, bi_2te_3.* Science, **325**, 178–181, (2009).

[24] Chao-Xing Liu, Xiao-Liang Qi, HaiJun Zhang, Xi Dai, Zhong Fang, and Shou-Cheng Zhang. *Model hamiltonian for topological insulators.* Phys. Rev. B, **82**, 045122, (2010).

[25] Liang Fu. *Hexagonal warping effects in the surface states of the topological insulator Bi_2Te_3.* Phys. Rev. Lett., **103**, 266801, (2009).

[26] Z.-H. Pan, E. Vescovo, A. V. Fedorov, D. Gardner, Y. S. Lee, S. Chu, G. D. Gu, and T. Valla. *Electronic structure of the topological insulator Bi_2Se_3 using angle-resolved photoemission spectroscopy: Evidence for a nearly full surface spin polarization.* Physical Review Letters, **106**, 257004, (2011).

[27] S. Souma, K. Kosaka, T. Sato, M. Komatsu, A. Takayama, T. Takahashi, M. Kriener, Kouji Segawa, and Yoichi Ando. *Direct measurement of the out-of-plane spin texture in the dirac-cone surface state of a topological insulator.* Physical Review Letters, **106**, 216803, (2011).

[28] Tong Zhang, Peng Cheng, Xi Chen, Jin-Feng Jia, Xucun Ma, Ke He, Lili Wang, Haijun Zhang, Xi Dai, Zhong Fang, Xincheng Xie, and Qi-Kun Xue. *Experimental demonstration of topological surface states protected by time-reversal symmetry.* Phys. Rev. Lett., **103**, 266803, (2009).

[29] Oleg V. Yazyev, Joel E. Moore, and Steven G. Louie. *Spin polarization and transport of surface states in the topological insulators Bi_2Si_3 and Bi_2Te_3 from first principles.* Phys. Rev. Lett., **105**, 266806, (2010).

[30] Seung Ryong Park, Choong H. Kim, Jaejun Yu, Jung Hoon Han, and Changyoung Kim. *Orbital-angular-momentum based origin of rashba-type surface band splitting.* Phys. Rev. Lett., **107**, 156803, (2011).

[31] Haijun Zhang, Chao-Xing Liu, and Shou-Cheng Zhang. *Spin-orbital texture in topological insulators.* Phys. Rev. Lett., **111**, 066801, (2013).

[32] Yue Cao, J. A. Waugh, J-W. Zhang, X-W. Luo, Q. Wang, T. J. Reber, S. K. Mo, Z. Xu, A. Yang, J. Schneeloch, G. D. Gu, M. Brahlek, N. Bansal, S. Oh, A. Zunger, and D. S. Dessau. *Mapping the orbital wavefunction of the surface states in three-dimensional topological insulators.* Nature Phys., **9**, 499–504, (2013).

[33] Kazuma Eto, Zhi Ren, A. A. Taskin, Kouji Segawa, and Yoichi Ando. *Angular-dependent oscillations of the magnetoresistance in Bi_2Se_3 due to the three-dimensional bulk fermi surface.* Phys. Rev. B, **81**, 195309, (2010).

[34] Y. S. Hor, A. Richardella, P. Roushan, Y. Xia, J. G. Checkelsky, A. Yazdani, M. Z. Hasan, N. P. Ong, and R. J. Cava. *p-type Bi_2Se_3 for topological insulator and low-temperature thermoelectric applications.* Phys. Rev. B, **79**, 195208, (2010).

[35] James G. Analytis, Jiun-Haw Chu, Yulin Chen, Felipe Corredor, Ross D. McDonald, Z. X. Shen, and Ian R. Fisher. *Bulk fermi surface coexistence with dirac surface state in Bi_2Se_3: A comparison of photoemission and Shubnikov de haas measurements.* Phys. Rev. B, **81**, 205407, (2010).

[36] Dong-Xia Qu, Y. S. Hor, Jun Xiong, R. J. Cava, and N. P. Ong. *Experimental realization of a three-dimensional topological insulator, bi_2te_3.* Science, **329**, 821–824, (2010).

[37] Zhi Ren, A. A. Taskin, Satoshi Sasaki, Kouji Segawa, and Yoichi Ando. *Large bulk resistivity and surface quantum oscillations in the topological insulator Bi_2Te_2Se.* Phys. Rev. B, **82**, 241306, (2010).

[38] Zhi Ren, A. A. Taskin, Satoshi Sasaki, Kouji Segawa, and Yoichi Ando. *Optimizing $Bi_{2-x}Sb_xTe_{3-y}Se_y$ solid solutions to approach the intrinsic topological insulator regime.* Phys. Rev. B, **84**, 165311, (2011).

[39] Stefan. Hüfner. *Very High Resolution Photoelectron Spectroscopy.* Springer, (2009).

[40] M. P. Seah and W. A. Dench. *Quantitative electron spectroscopy of surfaces: a standard data base for electron inelastic mean free paths in solids.* Surface and interface analysis, **1**, 2, 1979.

[41] E. Kisker, R. Clauberg, and W. Gudat. *Electron spectrometer for spin-polarized angle-and energy-resolved photoemission from ferromagnets.* Review of Scientific Instruments, **53**, 1137, (1982).

[42] Shan Qiao, Akio Kimura, Ayumi Harasawa, M. Sawada, J.-G. Chung, and A. Kakizaki. *A new compact electron spin polarimeter with a high efficiency.* Review of scientific instruments, **68**, 4390, (1997).

[43] K. Iori, K. Miyamoto, H. Narita, K. Sakamoto, A. Kimura1, S. Qiao, K. Shimada, H. Namatame, and M. Taniguchi. *The self-calibration of a retarding-type Mott spin polarimeter with a large collection angle.* Review of Scientific Instruments, **77**, 013101, (2006).

[44] V. N. Petrov, V. V. Grebenshikov, B. D. Grachev, and A. S. Kamochkin. *New compact classical 40 kV Mott polarimeter.* Review of scientific instruments, **74**, 1278, (2003).

[45] J. Kirschner and R. Feder. *Spin polarization in double diffraction of low-energy electrons from w(001): Experiment and theory.* Phys. Rev. Lett., **42**, 1008, (1979).

[46] G.-C. Wang, R. J. Celotta, and D. T. Pierce. *Polarized low-energy-electron diffraction from w(100).* Phys. Rev. B, **23**, 1761, (1981).

[47] F. U. Hillebrecht, R. M. Jungblut, L. Wiebusch, Ch. Roth, H. B. Rose, D. Knabben, C. Bethke, N. B. Weber, St. Manderla, U. Rosowski, and E. Kisker. *High-efficiency spin polarimetry by very-low-energy electron scattering from Fe(100) for spin-resolved photoemission.* Review of scientific instruments, **74**, 1229, (2002).

[48] Riccardo Bertacco, Davide Onofrio, and Franco Ciccacci. *A novel electron spin-polarization detector with very large analyzing power.* Review of scientific instruments, **70**, 3572, (1999).

[49] Taichi Okuda, Yasuo Takeichi, Yuuki Maeda, Ayumi Harasawa, Iwao Matsuda, Toyohiko Kinoshita, and Akito Kakizaki. *A new spin-polarized photoemission spectrometer with very high efficiency and energy resolution.* Review of Scientific Instruments, **79**, 123117, (2008).

[50] A. Winkelmann, D. Hartung, H. Engelhard, C.-T. Chiang, and J. Kirschner. *High efficiency electron spin polarization analyzer based on exchange scattering at Fe/W(001).* Review of Scientific Instruments, **79**, 083303, (2008).

[51] Joachim Kessler. Polarized Electrons. Springer, (1985).

[52] Scienta official home page. `http://www.vgscienta.com/productlist.aspx?MID=398`.

[53] Specs official home page. `http://www.specs.de/cms/front_content.php?idcat=183`.

[54] Timothy J. Gay and FB Dunning. *Mott electron polarimetry.* Review of scientific instruments, **63**, 1635, (1992)).

[55] Riccardo Bertacco, Michele Merano, and Franco Ciccacci. *Spin dependent electron absorption in Fe (001)-p (1×1) O: A new candidate for a stable and efficient electron polarization analyzer.* Applied physics letters, **72**, 2050, (1998).

[56] Taichi Okuda, Koji Miyamaoto, Hirokazu Miyahara, Kenta Kuroda, Akio Kimura, Hirofumi Namatame, and Masaki Taniguchi. *Efficient spin resolved spectroscopy observation machine at Hiroshima synchrotron radiation center.* Review of Scientific Instruments, **82**, 103302, (2011).

[57] David Hsieh, Y. Xia, Dong Qian, L. Wray, J. H. Dil, F. Meier, J. Osterwalder, L. Patthey, J. G. Checkelsky, N. P. Ong, A. V. Fedorov, H. Lin, A. Bansil, D. Grauer, Y. S. Hor, R. J. Cava, and M. Z. Hasan. *A tunable topological insulator in the spin helical Dirac transport regime.* Nature, **460**, 1101, (2009).

[58] K. Kuroda, M. Arita, K. Miyamoto, M. Ye, J. Jiang, A. Kimura, E. E. Krasovskii, E. V. Chulkov, H. Iwasawa, T. Okuda, K. Shimada, Y. Ueda, H. Namatame, and M. Taniguchi. *Hexagonally deformed fermi surface of the 3d topological insulator Bi_2Se_3.* Phys. Rev. Lett., **105**, 076802, (2010).

[59] AS Núñez and Joaquín Fernández-Rossier. *Colossal anisotropy in diluted magnetic topological insulators.* Solid State Communications, **152**, 403, (2012).

[60] M. Zahid Hasan and Charles L. Kane. *Colloquium: topological insulators.* Reviews of Modern Physics, **82**, 3045, (2010).

[61] Xiao-Liang Qi and Shou-Cheng Zhang. *Topological insulators and superconductors.* Reviews of Modern Physics, **83**, (1057), 2011.

[62] Rundong Li, Jing Wang, Xiao-Liang Qi, and Shou-Cheng Zhang. *Dynamical axion field in topological magnetic insulators.* Nature Physics, **6**, 284, (2010).

[63] Qin Liu, Chao-Xing Liu, Cenke Xu, Xiao-Liang Qi, and Shou-Cheng Zhang. *Magnetic impurities on the surface of a topological insulator.* Phys. Rev. Lett., **102**, 156603, (2009).

[64] Y. L. Chen, J.-H. Chu, J. G. Analytis, Z. K. Liu, Kyushiro Igarashi, H.-H. Kuo, X. L. Qi, Sung-Kwan Mo, R. G. Moore, D. H. Lu, M Hashimoto, T. Sasagawa, S.-C. Zhang, I. R. Fisher, and Z. X. Hussain, Z. Shen. *Massive dirac fermion on the surface of a magnetically doped topological insulator.* Science, **329** (5992), (2010).

[65] G. Van der Laan and I. W. Kirkman. *The 2p absorption spectra of 3d transition metal compounds in tetrahedral and octahedral symmetry.* Journal of Physics: Condensed Matter, **4**, 4189, (1992).

[66] Y. Takeda, M. Kobayashi, T. Okane, T. Ohkochi, J. Okamoto, Y. Saitoh, K. Kobayashi, H. Yamagami, A. Fujimori, A. Tanaka, J. Okabayashi, M. Oshima, S. Ohya, P. N. Hai, and M. Tanaka. *Nature of magnetic coupling between Mn ions in as-grown $Ga_{1-x}Mn_xAs$ studied by x-ray magnetic circular dichroism.* Phys. Rev. Lett., **100**, 247202, (2008).

[67] Paolo Carra, B. T. Thole, Massimo Altarelli, and Xindong Wang. *X-ray circular dichroism and local magnetic fields.* Phys. Rev. Lett., **70**, 694, (1993).

[68] G. van der Laan and B. T. Thole. *Strong magnetic x-ray dichroism in 2p absorption spectra of 3d transition-metal ions.* Phys. Rev. B, **43**, 13401, (1991).

[69] Kwanghyun Cho, Hoon Koh, Jonghyurk Park, S-J Oh, Hyeong-Do Kim, Moonsup Han, J-H Park, C. T. Chen, Y. D. Kim, J-S Kim, and B. T. Jonker. *X-ray absorption spectroscopy study of diluted magnetic semiconductors: $Zn_{1-x}Mn_xSe$ (M= Mn, Fe, Co) and $Zn_{1-x}Mn_xY$ (Y= Se, Te).* Physical Review B, **63**, 155203, (2011).

[70] Yi Zhang, Ke He, Cui-Zu Chang, Can-Li Song, Li-Li Wang, Xi Chen, Jin-Feng Jia, Zhong Fang, Xi Dai, Wen-Yu Shan, Shun-Qing Shen, Qian Niu, Xiao-Liang Qi, Shou-Cheng Zhang, Xu-Cun Ma, and Qi-Kun Xue. *Crossover of the three-dimensional topological insulator Bi_2Se_3 to the two-dimensional limit.* Nature Physics, **6**, 584, (2010).

[71] Chris Jozwiak, Y. L. Chen, A. V. Fedorov, J. G. Analytis, C. R. Rotundu, A. K. Schmid, J. D. Denlinger, Y.-D. Chuang, D.-H. Lee, I. R. Fisher, R. J. Birgeneau, Z.-X. Shen, Z. Hussain, and A. Lanzara. *Widespread spin polarization effects in photoemission from topological insulators.* Physical Review B, **84**, 165113, (2011).

[72] Hsin Lin, R. S. Markiewicz, L. A. Wray, L. Fu, M. Z. Hasan, and A. Bansil. *Single-dirac-cone topological surface states in the $TlBiSe_2$ class of topological semiconductors.* Phys. Rev. Lett., **105**, 036404, (2010).

[73] Binghai Yan, Chao-Xing Liu, Hai-Jun Zhang, Chi-Yung Yam, Xiao-Liang Qi, Thomas Frauenheim, and Shou-Cheng Zhang. *Theoretical prediction of topological insulators in thallium-based iii-v-vi2 ternary chalcogenides.* EPL (Europhysics Letters), **90**, 37002, (2010).

[74] S. V. Eremeev, Yu M. Koroteev, and Evgenii Vladimirovich Chulkov. *Ternary thallium-based semimetal chalcogenides ¡t¿l-¡v¿-¡vi¿2 as a new class of three-dimensional topological insulators.* JETP letters, **91**, 594, (2010).

[75] TV Menshchikova, SV Eremeev, Yu M Koroteev, VM Kuznetsov, and Evgenii Vladimirovich Chulkov. *Ternary compounds based on binary topological insulators as an efficient way for modifying the dirac cone.* JETP letters, **93**, 15, (2011).

[76] Hsin Lin, L. Andrew Wray, Yuqi Xia, Suyang Xu, Shuang Jia, Robert J. Cava, Arun Bansil, and M. Zahid Hasan. *Half-heusler ternary compounds as new multifunctional experimental platforms for topological quantum phenomena.* Nature Materials, **9**, 546, (2010).

[77] S. N. Toubektsis and E. K. Polychroniadis. *Growth and structural considerations on single TlBiSe$_2$ crystals.* Journal of crystal growth, **84**, 316, (1987).

[78] S. V. Eremeev, G. Bihlmayer, M. Vergniory, Yu. M. Koroteev, T. V. Menshchikova, J. Henk, A. Ernst, and E. V. Chulkov. *Ab-initio electronic structure of thallium-based topological insulators.* Phys. Rev. B, **83**, 205129, (2011).

[79] K. Kuroda, M. Ye, A. Kimura, S. V. Eremeev, E. E. Krasovskii, E. V. Chulkov, Y. Ueda, K. Miyamoto, T. Okuda, K. Shimada, H. Namatame, and M. Taniguchi. *Experimental realization of a three-dimensional topological insulator phase in ternary chalcogenide TlBiSe$_2$.* Phys. Rev. Lett., **105**, 146801, (2010).

[80] M. Higashiguchi. *Quantitative evaluation of the bulk and surface electronic states of transition-metal single crystals by angle-resolved photoemission spectroscopy with synchrotron radiation.* PhD thesis, Graduate School of Science, Hiroshima University, (2008).

[81] S. R. Park, W. S. Jung, Chul Kim, D. J. Song, C. Kim, S. Kimura, K. D. Lee, and N. Hur. *Quasiparticle scattering and the protected nature of the topological states in a parent topological insulator Bi$_2$Se$_3$.* Physical Review B, **81**, 041405, (2010).

[82] Sergey V Eremeev, Gabriel Landolt, Tatiana V. Menshchikova, Bartosz Slomski, Yury M. Koroteev, Ziya S. Aliev, Mahammad B. Babanly, Jürgen Henk, Arthur Ernst, Luc Patthey, Andreas Eich, Alexander Ako Khajetoorians, Julian Hagemeister, Oswald Pietzsch, Jens Wiebe, Roland Wiesendanger, Pedro M. Echenique, Stepan S. Tsirkin,

Imamaddin R. Amiraslanov, J. Hugo Dil, and Evgueni V. Chulkov. *Atom-specific spin mapping and buried topological states in a homologous series of topological insulators.* Nature Communications, **3**, 635, (2012).

[83] L. E. Shelimova, O. G. Karpinskii, T. E. Svechnikova, E. S. Avilov, M. A. Kretova, and V. S. Zemskov. *Synthesis and structure of layered compounds in the PbTe-Bi$_2$Te$_3$ and PbTe-Sb$_2$Te$_3$ systems.* Inorganic materials, **40**, 1264, (2004).

[84] K. Kuroda, H. Miyahara, M. Ye, S. V. Eremeev, Yu. M. Koroteev, E. E. Krasovskii, E. V. Chulkov, S. Hiramoto, C. Moriyoshi, Y. Kuroiwa, K. Miyamoto, T. Okuda, M. Arita, K. Shimada, H. Namatame, M. Taniguchi, Y. Ueda, and A. Kimura. *Experimental verification of PbBi$_2$Te$_4$ as a 3d topological insulator.* Phys. Rev. Lett., **108**, 206803, (2012).

[85] Georg Kresse and Jürgen Furthmüller. *Efficiency of ab-initio total energy calculations for metals and semiconductors using a plane-wave basis set.* Computational Materials Science, **6**, (1996).

[86] G. Kresse and D. Joubert. *From ultrasoft pseudopotentials to the projector augmented-wave method.* Phys. Rev. B, **59**, 1758, (1999).

[87] Ying Ran, Yi Zhang, and Ashvin Vishwanath. *One-dimensional topologically protected modes in topological insulators with lattice dislocations.* Nature Physics, **5**, 298, (2009).

[88] Su-Yang Xu, Y. Xia, L. A. Wray, S. Jia, F. Meier, J. H. Dil, J. Osterwalder, B. Slomski, A. Bansil, H. Lin, R. J. Cava, and M. Z. Hasan. *Topological phase transition and texture inversion in a tunable topological insulator.* Science, **332**, 560, (2011).

[89] T. Sato, Kouji Segawa, K. Kosaka, S. Souma, K. Nakayama, K. Eto, T. Minami, Yoichi Ando, and T. Takahashi. *Unexpected mass acquisition of Dirac fermions at the quantum phase transition of a topological insulator.* Nature Physics, **7**, 840, (2011).

[90] Ulrich Heinzmann and J. Hugo Dil. *Spin-orbit-induced photoelectron spin polarization in angle-resolved photoemission from both atomic and*

condensed matter targets. Journal of Physics: Condensed Matter, **24**, 173001, (2012).

[91] T Arakane, T Sato, S Souma, K Kosaka, K Nakayama, M Komatsu, T Takahashi, Zhi Ren, Kouji Segawa, and Yoichi Ando. *Tunable Dirac cone in the topological insulator $Bi_{2-x}Sb_xTe_{3-y}Se_y$.* Nature Communications, **3**, 636, (2012).

[92] Kenta Kuroda, Mao Ye, Eike F. Schwier, Munisa Nurmamat, Kaito Shirai, Masashi Nakatake, Shigenori Ueda, Koji Miyamoto, Taichi Okuda, Hirofumi Namatame, Masaki Taniguchi, Yoshifumi Ueda, and Akio Kimura. *Experimental verification of the surface termination in the topological insulator $TlBiSe_2$ using core-level photoelectron spectroscopy and scanning tunneling microscopy.* Phys. Rev. B, **88**, 245308, (2013).

[93] Laurent Despont, F. Clerc, M. G. Garnier, H Berger, L. Forró, and P. Aebi. *Multiple scattering investigation of the 1t-tas2 surface termination.* The European Physical Journal B-Condensed Matter and Complex Systems, **52**, 421, (2006).

[94] M. Salmerón, S. Ferrer, M. Jazzar, and G. A. Somorjai. *Core- and valence-band energy-level shifts in small two-dimensional islands of gold deposited on Pt(100): The effect of step-edge, surface, and bulk atoms.* Phys. Rev. B, **28**, 1158, (1983).

[95] K. G. Purcell, J. Jupille, and D. A. King. *Coordination number and surface core-level shift spectroscopy: Stepped tungsten surfaces.* Surface Science, **208**, 245, (1989).

[96] J. J. Joyce, M. Del Giudice, and J. H. Weaver. *Quantitative analysis of synchrotron radiation photoemission core level data.* Journal of Electron Spectroscopy and Related Phenomena, **49**, 31, (1989).

[97] F. J. Himpsel, P. Heimann, T.-C. Chiang, and D. E. Eastman. *Geometry-dependent Si 2p surface core-level excitations for Si(111) and Si(100) surfaces.* Phys. Rev. Lett., **45**, 1112, (1989).

[98] C. J. Karlsson, E. Landemark, Y.-C. Chao, and R. I. G. Uhrberg. *Atomic origins of the surface components in the Si 2p core-level spectra of the Si(111)7×7 surface.* Phys. Rev. B, **50**, 5767, (1994).

187

[99] C. So Fadley, S. B. M. Hagstrom, Mr. P. Klein, and D. A. Shirley. *Chemical effects on core-electron binding energies in iodine and europium.* The Journal of Chemical Physics, **48**, 3779, (1968).

[100] Y. Takata, Y. Kayanuma, M. Yabashi, K. Tamasaku, Y. Nishino, D. Miwa, Y. Harada, K. Horiba, S. Shin, S. Tanaka, E. Ikenaga, K. Kobayashi, Y. Senba, H. Ohashi, and T. Ishikawa. *Recoil effects of photoelectrons in a solid.* Phys. Rev. B, **75**, 233404, (2007).

[101] M. R. Scholz, J. Sánchez-Barriga, D. Marchenko, A. Varykhalov, A. Volykhov, L. V. Yashina, and O. Rader. *Tolerance of topological surface states towards magnetic moments: Fe on Bi_2Se_3.* Phys. Rev. Lett., **108**, 256810, (2012).

[102] Marco Bianchi, Dandan Guan, Shining Bao, Jianli Mi, Bo Brummerstedt Iversen, Philip DC King, and Philip Hofmann. *Coexistence of the topological state and a two-dimensional electron gas on the surface of Si_2Se_3.* Nature communications, **1**, 128, (2010).

[103] L. Andrew Wray, Su-Yang Xu, Yuqi Xia, David Hsieh, Alexei V Fedorov, Yew San Hor, Robert J. Cava, Arun Bansil, Hsin Lin, and M. Zahid Hasan. *A topological insulator surface under strong Coulomb, magnetic and disorder perturbations.* Nature Physics, **7**, 32, (2010).

[104] T. Valla, Z.-H. Pan, D. Gardner, Y. S. Lee, and S. Chu. *Photoemission spectroscopy of magnetic and nonmagnetic impurities on the surface of the Bi_2Se_3 topological insulator.* Phys. Rev. Lett., **108**, 117601, (2012).

[105] Seung Ryong Park, Jinhee Han, Chul Kim, Yoon Young Koh, Changyoung Kim, Hyungjun Lee, Hyoung Joon Choi, Jung Hoon Han, Kyung Dong Lee, Nam Jung Hur, Masashi Arita, Kenya Shimada, Hirofumi Namatame, and Masaki Taniguchi. *Chiral orbital-angular momentum in the surface states of Bi_2Se_3.* Physical Review Letters, **108**, 046805, (2012).

[106] Y.-H. Wang, D. Hsieh, D. Pilon, L. Fu, D. R. Gardner, Y. S. Lee, and N. Gedik. *Observation of a warped helical spin texture in Bi_2Se_3 from circular dichroism angle-resolved photoemission spectroscopy.* Physical Review Letters, **107**, 207602, (2011).

[107] Beomyoung Kim, Choong H. Kim, Panjin Kim, Wonsig Jung, Yeongk-wan Kim, Yoonyoung Koh, Masashi Arita, Kenya Shimada, Hirofumi Namatame, Masaki Taniguchi, Jaejun Yu, and Changyoung Kim. *Spin and orbital angular momentum structure of Cu(111) and Au(111) surface states.* Phys. Rev. B, **85**, 195402, (2012).

[108] M. Polcik, F. Allegretti, D. I. Sayago, Gareth Nisbet, C. L. A. Lamont, and D. P. Woodruff. *Circular dichroism in core level photoemission from an adsorbed chiral molecule.* Physical review letters, **92**, 236103, (2004).

[109] J. Bansmann, M. Getzlaff, C. Westphal, F. Fegel, and G. Schönhense. *Magnetic circular dichroism in valence-band photoemission from iron (100).* Surface science, **269**, 622, (1992).

[110] G. Schönhense, C. Westphal, J. Bansmann, and M. Getzlaff. *Circular dichroism in photoemission from nonmagnetic, low-Z solids: a conspicuous effect of the photon spin.* EPL (Europhysics Letters), **17**, 727, (1992).

[111] M. R. Scholz, J. Sánchez-Barriga, J. Braun, D. Marchenko, A. Varykhalov, M. Lindroos, Yung Jui Wang, Hsin Lin, A. Bansil, J. Minár, H. Ebert, A. Volykhov, L. V. Yashina, and O. Rader. *Reversal of the circular dichroism in angle-resolved photoemission from Bi_2Te_3.* Phys. Rev. Lett., **110**, 216801, (2013).

[112] U. Fano. *Spin orientation of photoelectrons ejected by circularly polarized light.* Physical Review, **178**, 131, (1969).

[113] Ulrich Heinzmann, J. Kessler, and J. Lorenz. *Wavelength dependence of the fano effect.* Physical Review Letters, **25**, 1325, (1970).

[114] Cheol-Hwan Park and Steven G. Louie. *Spin polarization of photoelectrons from topological insulators.* Physical Review Letters, **109**, 097601, (2012).

[115] Chris Jozwiak, Cheol-Hwan Park, Kenneth Gotlieb, Choongyu Hwang, Dung-Hai Lee, Steven G. Louie, Jonathan D. Denlinger, Costel R. Rotundu, Robert J. Birgeneau, Zahid Hussain, and Alessandra Lanzara. *Photoelectron spin-flipping and texture manipulation in a topological insulator.* Nature Physics, **9**, 298, (2013).

189

[116] J. W. McIver, David Hsieh, Hadar Steinberg, Pablo Jarillo-Herrero, and Nuh Gedik. *Control over topological insulator photocurrents with light polarization.* Nature nanotechnology, **7**, 96, (2011).

Acknowledgments

March 2014
Kenta Kuroda